MARMARA UNIVERSITY

INSTITUTE FOR GRADUATE STUDIES IN PURE AND APPLIED SCIENCES

OPTICAL PROPERTIES OF GROUP III-NITRIDE THIN FILMS GROWN BY HOLLOW CATHODE PLASMA ASSISTED ATOMIC LAYER DEPOSITION

NEŞE GÜNGÖR

Ph. D. THESIS

Department of Physics

Physics Program

Thesis Supervisor

Prof. Dr. Mustafa ALEVLİ

İSTANBUL, 2019

MARMARA UNIVERSITY

INSTITUTE FOR GRADUATE STUDIES
IN PURE AND APPLIED SCIENCES

OPTICAL PROPERTIES OF GROUP III-NITRIDE THIN FILMS GROWN BY HOLLOW CATHODE PLASMA ASSISTED ATOMIC LAYER DEPOSITION

NEŞE GÜNGÖR
(721213001)

Ph. D. THESIS
Department of Physics
Physics Program

Thesis Supervisor
Prof. Dr. Mustafa ALEVLİ

İSTANBUL, 2019

MARMARA UNIVERSITY
INSTITUTE FOR GRADUATE STUDIES IN PURE AND APPLIED SCIENCES

Neşe GÜNGÖR, a Doctor of Philosophy student of Marmara University Institute for Graduate Studies in Pure and Applied Sciences, defended her thesis entitled "**Optical properties of group III-nitride thin films grown by hollow cathode plasma assisted atomic layer deposition**", on 26.11.2019 and has been found to be satisfactory by the jury members.

Jury Members

Prof. Dr. Mustafa ALEVLİ (Advisor)
Marmara University .... (SIGN)................

Prof. Dr. Şahin AKTAŞ (Jury Member)
Marmara University.. (SIGN)................

Prof. Dr. Hilmi ÜNLÜ (Jury Member)
Istanbul Technical University.. (SIGN)................

Prof. Dr. Zikri ALTUN (Jury Member)
Marmara University.. (SIGN)................

Prof. Dr. Osman ÖZTÜRK (Jury Member)
Gebze Technical University .... (SIGN)................

APPROVAL

Marmara University Institute for Graduate Studies in Pure and Applied Sciences Executive Committee approves that Neşe GÜNGÖR be granted the degree of Doctor of Philosophy in Department of Physics, Physics Program on 11.12.2019. (Resolution no: 2019/25-02).

Director of the Institute
Prof. Dr. Bülent EKİCİ

PREFACE

First, I would like to express my sincere gratitude to my supervisor Prof. Dr. Mustafa Alevli for his endless efforts, valuable guidance, motivation and confidence with me to make this work possible. I am also indebted to the members of my thesis committee Prof. Dr. Şahin Aktaş, and Prof. Dr. Hilmi Ünlü.

I would like to thank UNAM engineers, especially Dr. Gökçe Çelik, for all their help and also Petro Deminskyi, and Seda Kizir for their support. Special thanks to my friends, Dr. Pınar Kirezli Uludağ, Türküler Durğut and Filiz Çağlar for their continuous support, encouragement in difficult times and endless friendship. I would also like to thank all my mates including Haluk, Okan, and Sinan.

During my doctoral studies, warmest thanks go to my beloved family for their efforts to support me, never lose their faith and their trust in me in all circumstances. I am sincerely grateful to my parents Cemile and Sevdekar, my sisters Sevgi, Birsen, Nurdan, my brother Muhammed, Gencay and my newborn nephew İsmail Utku. I also indebted to my aunt Songül, her husband Yafes, and their children İlknur, Öznur, Muhammed and all of the rest of my family for all of their sacrifices and their unconditional love and support

Financial support from TUBITAK BIDEB Ph.D. Fellowship Program (2211-E) is gratefully acknowledged. Finally, I would like to thank TÜBİTAK (Grant No. 114F002) and Marmara University BAPKO (Project No. FEN-C-DRP-250416-0181) for financial support.

October, 2019 **Neşe GÜNGÖR**

CONTENTS

PREFACE **i**
CONTENTS **ii**
ÖZET **v**
ABSTRACT **vii**
CLAIM FOR ORIGINALITY **ix**
LIST OF PUBLICATIONS **x**
SYMBOLS **xi**
ABBREVIATIONS **xiv**
LIST OF FIGURES **xvi**
LIST OF TABLES **xx**
1. INTRODUCTION **1**
2. ATOMIC LAYER DEPOSITION **3**
2.1. Basic Concepts and Principles of ALD 3
2.2. Atomic Layer Deposition Growth Mechanisms 4
2.2.1. Reactants and surface chemistry 4
2.2.2. Temperature effects 5
2.2.3. Substrate effect and growth inhibition 6
2.3. Plasma Enhanced Atomic Layer Deposition 7
2.4. Opportunities and Challenges 9
3. OPTICAL PROPERTIES OF SEMICONDUCTOR AND MATERIAL CHARACTERIZATION **11**
3.1. Optical Constants and the Dielectric Function 11
3.2. Models of Dielectric Function 12
3.2.1. Electronic transition 13
3.2.2. Lattice Vibrations 18
3.2.3. Free-carrier contribution 21

3.2.4. Low-Polarity Mode Contributions 23

3.3. Raman lineshape analysis 23

3.4. Transfer Matrix Method 25

3.5. Spectroscopic Ellipsometry 29

3.6. Infrared Ellipsometry 30

3.7. X-ray Diffraction 33

3.8. X-ray Photoelectron Spectroscopy 33

3.9. Atomic Force Microscopy 35

4. PROPERTIES OF GaN GROWN BY HCPA-ALD 37

4.1. The Role of Film Thickness on The Structural and Optical Properties of GaN on Si (100) 37

4.1.1. Introduction 37

4.1.2. Experimental 38

4.1.3. Structural characterization of GaN films 40

4.1.4. Compositional analysis 42

4.1.5. Surface morphology analysis 46

4.1.6. Optical properties 48

4.2. Thickness Effect of GaN on Sapphire 52

4.2.1. Introduction 52

4.2.2. Film Growth 54

4.2.3. Characterization of synthesized samples 55

4.2.4. Raman spectroscopy line shape analysis and determination of carrier concentration 55

4.2.5. Influence of thickness on UV-Visible refractive index 61

4.2.6. Influence of thickness on infrared refractive index and phonon modes 67

5. PROPERTIES OF GROUP III-NITRIDES GROWN BY HCPA-ALD 75

5.1. Introduction 75

5.2. HCPA-ALD III-Nitride Film Deposition 76

5.3. Film Characterization 76

5.4. Optical Modelling 77

5.5. Crystalline structure and composition 79

5.6. Optical properties 82

6. CONCLUSIONS 91

REFERENCES 95

ÖZGEÇMİŞ 1

ÖZET

OYUK KATOT PLAZMA DESTEKLİ ATOMİK KATMAN BİRİKTİRME YÖNTEMİ İLE BÜYÜTÜLEN GRUP III-NİTRÜR İNCE FİLMLERİNİN OPTİK ÖZELLİKLERİ

Düşük sıcaklıkta oyuk katodlu plazma destekli atomik tabaka biriktirme (HCPA-ALD) tarafından büyütülen grup III-Nitrit ince filmlerin özellikleri, biriken ince filmler için detaylı karakterizasyon sonuçlarıyla sunulmaktadır. Bu bağlamda, önce, film kalınlığı ve substratın düşük sıcaklıkta yetiştirilen GaN ince filmin özellikleri üzerindeki etkisini analiz ettik. Bu amaca yönelik olarak, Si alttaşı için kalınlığı 5.37 ile 81.40 nm arasında ve sapphire altaşı için kalınlığı 6.57 nm ile 84.35 nm arasında yüksek (002) yönelimine sahip GaN filmleri sıralı bir trietilguyum (TEG) ve N_2/H_2 plazması enjeksiyonu kullanılarak büyütülmüştür. X ışını kırınımı (XRD) analizi, GaN filmlerinin (002) tercihli bir büyüme yönüne sahip olduğunu ve GaN filmlerinin kristal kalitesinin her iki alttaş için kalınlığın artmasıyla arttığını gösterdi. XRD ve atomik kuvvet mikroskopisi, GaN tanelerinin varlığını doğruladı ve Si üzerindeki GaN katmanının kalınlığı 5.37 nm'den 48.65 nm'ye yükseldiğinde tane büyüklüğü arttığını gösterdi. X ışını fotoelektron spektrumundan, GaN filminde bulunan oksijen miktarının, kalınlık arttıkça azaldığı gösterilmiştir.

Spektroskopik elipsometri analizi, optik film yoğunluğunun ve lokal kristalliğin, film kalınlığının artmasıyla arttığını ortaya koymaktadır, ancak film kalınlığındaki artışın, tüm GaN örnekleri için bu özellikleri iyileştirmediği görülmektedir. Bulgularımız, film kalınlığının kırılma indeksi üzerinde 300-1000 nm dalga boyu aralığında önemli etkilere sahip olduğunu ancak alttaşın önemli bir etkisinin olmadığını göstermektedir. Ayrıca, optik bant aralığı sonuçları, bant aralığı genişletmenin tüm HCPA-ALD ile büyütülen GaN örnekleri için geçerli olduğunu göstermiştir. Öte yandan, kızılötesi spektroskopik elipsometri (IRSE) kullanılarak elde edilen kızılötesi bölgedeki kırılma indisi, artan kalınlıkta belirgin olarak değişmemektedir. Ayrıca, kızılötesi elipsometrenin sonuçlarını Raman spektrumları ile karşılaştırarak E_1(TO), E_1(LO), A_1(LO), and E_2^{High} fonon modlarını tespit edilmiştir. Frekanslarının GaN filmlerin stres durumuna bağımlılıkları da analiz edilmiş ve tartışılmıştır.

İkinci bölümde, plazma gazı bileşiminin, birikmiş ikili III-nitrit ince filmlerin özellikleri üzerindeki etkisini analiz ettik. Bu amaç için, AlN, GaN ve InN filmleri, H_2 akışının etkilerini araştırmak için sadece N_2 (50 smcm) ve N_2 / H_2 (50 + 50 smcm, 50 + 25 smcm) plazma kullanılarak Si (100) altaşı üzerine büyütülmüştür. N_2/H_2 plazması ile büyütülen AlN ve GaN ince filmlerinin düşük açılı XRD (GIXRD) desenleri, H_2 akışı 50'den 25 sccm'ye düştüğünde neredeyse değişmeden kaldı. Diğer taraftan, H_2 olmadan N_2 plazmasının kullanılması, bulk film içinde önemli karbon safsızlığı olan amorf GaN ince filmlere yol açtı. AlN durumunda, kristal yapı amorf benzeri malzemeye önemli ölçüde değiştirildiği için benzer davranışlar gözlenmiştir. AlN ve GaN ince filmlerin kalınlıkları, sadece N_2 plazma gazı olarak kullanıldığında muazzam bir artış gösterdi. Ayrıca, hem AlN hem de GaN filmlerin kırılma endeksi değerleri, sadece N_2-plazma kullanımında azalmıştır; ki bu, film kalitesinin bozulmasını onaylamaktadır. Yalnızca N_2 plazma ile biriktirilen GaN ve AlN filmlerinin yapısal zayıflıkları, büyüyen film içinde sıkışan karbon kirliliklerinin varlığı nedeniyledir. İlginç bir şekilde, N_2/H_2 plazma ile büyütülmüş InN filmlerinde benzer sonuçlar gözlemlemedik. InN için, GIXRD ve spektroskopik elipsometri sonuçları, plazma gazında H_2 içeriği arttıkça biriken filmlerin fazlarının InN'den In + InN'ye değiştiğini göstermektedir. Öte yandan, sadece N_2-plazma ile yetiştirilen InN filmler gelişmiş yapısal özellikler göstermektedir. Bununla birlikte, biriken InN katmanlarındaki kalıntı karbon içeriğini en aza indirmek için önemli ölçüde daha yüksek N_2 plazma maruziyet sürelerine ihtiyaç vardır.

Eylül, 2019 **Neşe GÜNGÖR**

ABSTRACT

OPTICAL PROPERTIES OF GROUP III-NITRIDE THIN FILMS GROWN BY HOLLOW CATHODE PLASMA ASSISTED ATOMIC LAYER DEPOSITION

In this thesis, properties of group III-Nitride thin films grown by hollow-cathode plasma-assisted atomic layer deposition (HCPA-ALD) at low temperature are presented with detailed characterization results for the deposited thin films. In this respect, first, we analyzed the effect of film thickness and substrate on properties of low-temperature grown GaN thin film. Towards this goal, highly oriented (002) GaN films as a function of film thickness, ranging from 5.37 to 81.40 nm on Si and 6.57 nm to 84.35 nm on sapphire substrate deposited using a sequential injection of triethylgallium (TEG) and N_2/H_2 plasma. X-ray diffraction (XRD) analysis reveals that GaN films have a (002) preferential growth direction fand the crystalline quality of GaN films was improved with the increase of thickness for both substrates. XRD and atomic force microscopy confirmed the presence of GaN grains and the grain size increases when the thickness of GaN layer on Si increases from 5.37 nm to 48.65 nm. From the x-ray photoelectron spectra, it was shown that the amount of oxygen incorporated in the GaN film decreases as the thickness increases.

The spectroscopic ellipsometry analysis reveals that optical film density and local crystallinity was improved with increasing film thickness, but further increase in the film thickness does not seem to improve these features for all GaN samples. Our findings show that film thickness has significant effects on the refractive index in the wavelength range of 300-1000 nm, but the substrate has no significant effect. Moreover, the optical band edge results suggested that bandgap widening is valid for all HCPA-ALD grown GaN samples. On the other hand, the refractive index in the infrared region obtained using infrared spectroscopic ellipsometry (IRSE) does not obviously change with increasing thickness. Moreover, we have identified E_1(TO), E_1(LO), A_1(LO), and E_2^{High} phonon modes by comparing the results of infrared ellipsometry with Raman spectra. The dependencies of their frequencies on the stress state of GaN films were analyzed and discussed.

In the second part, we analyzed the effect of plasma gas composition on the properties of deposited binary III-nitride thin films. For this purpose, AlN, GaN, and InN films were deposited on Si (100) substrates using N_2-only (50 sccm), as well as N_2/H_2 (50+50 sccm, 50+25 sccm) plasma to investigate the impact of H_2 flow. Grazing-incidence XRD (GIXRD) patterns of AlN and GaN thin films deposited with N_2/H_2 plasma remained almost unchanged when H_2 flow decreased from 50 to 25 sccm. On the other hand, the use of N_2 plasma without any H_2 resulted in amorphous GaN thin films with significant carbon impurity within the bulk film. In the case of AlN, similar behavior was observed as the crystal structure is significantly altered to amorphous-like material. Thicknesses of AlN and GaN thin films increased tremendously when N_2-only was used as the plasma gas. Furthermore, refractive index values of both AlN and GaN films decreased upon the use of N_2-only plasma, which confirms the deterioration of the film quality. Structural weaknesses of GaN and AlN films deposited with N_2-only plasma are due to the presence of carbon impurities that are trapped inside the growing film. Interestingly, we did not observe similar results in InN films grown with N_2/H_2 plasma. For InN, GIXRD and spectroscopic ellipsometry results show that the phases of deposited films change from InN to In+InN as H_2 content in the plasma gas is increased. On the other hand, InN films grown with N_2-only plasma show improved structural properties. However, significantly higher N_2 plasma exposure times are needed to minimize the residual carbon content in deposited InN layers.

September, 2013 **Neşe GÜNGÖR**

CLAIM FOR ORIGINALITY

Group III-nitride compound semiconductors and their alloys have emerged as versatile and high-performance materials for a wide range of electronic and optoelectronic device applications. Besides possessing very unique material properties individually, ternary and quaternary alloys of this family are particularly important since their bandgaps can easily be tuned by adjusting the alloy composition. Although high quality III- nitride thin films can be grown at high temperatures (>1000 °C), deposition of these films on temperature-sensitive device layers and substrates necessitates the adaptation of low-temperature methods such as atomic layer deposition (ALD) based on self-terminating and sequential gas-solid surface reactions.

Due these promising properties of both group-III nitrides and ALD, in this thesis, group-III Nitrides were successfully grown by hollow-cathode plasma-assisted ALD (HCPA-ALD) at low temperatures (200 °C) in order to determine the effect of film thickness and plasma gas composition. The evolution of crystallinity, chemical composition, vibrational properties surface morphology, optical properties with a wide range of group III-nitride were analyzed and discussed in detailed.

In conclusion, we believe that the findings obtained in this thesis and the group-III nitride thin films grown at low temperatures will open a pathway for the realization of In rich InGaN heterostructures.

October, 2019 **Neşe GÜNGÖR**

LIST OF PUBLICATIONS

- ***"Visible/Infrared refractive index and phonon properties of GaN films grown on sapphire by hollow-cathode plasma-assisted atomic layer deposition."*** Neşe Güngör, Mustafa Alevli. Journal of Vacuum Science & Technology A: Vacuum, Surfaces, and Films, 37(5) (2019)
- ***"The role of film thickness on the structural and optical properties of GaN on Si (100) grown by hollow-cathode plasma-assisted atomic layer deposition."*** Neşe Güngör, Mustafa Alevli. Journal of Vacuum Science & Technology A: Vacuum, Surfaces, and Films, 36(2) (2018)
- "***Influence of N_2/H_2 and N_2 plasma on binary III-nitride films prepared by hollow-cathode plasma-assisted atomic layer deposition."*** Mustafa Alevli, Neşe Güngör. Journal of Vacuum Science & Technology A: Vacuum, Surfaces, and Films, 36(1), 01A110 (2018).

SYMBOLS

$\boldsymbol{D}$	:	displacement field
$\boldsymbol{E}$	:	electric field
$\boldsymbol{I}$	:	intensity
$\boldsymbol{M}_m$	:	propagation matrix
$\boldsymbol{M}_s$	:	result matrix
$\boldsymbol{N}$	:	carrier concentration
$\boldsymbol{P}$	:	polarization field
$\boldsymbol{R}$	:	reflection
$\boldsymbol{T}$	:	transmission
Γ_{ac}	:	acoustic phonon modes
Γ_{opt}	:	optical phonon modes
Δ	:	ellipsometric data
ψ	:	ellipsometric data
$\boldsymbol{d}$	:	film thickness
$\boldsymbol{k}$	:	extinction coefficient
$\boldsymbol{m}^*$	:	effective mass
$\tilde{n}$	:	complex index of refraction
$\boldsymbol{n}$	:	refractive index (real part)
$\boldsymbol{q}$	:	photon wave vector
r_p	:	p-polarized reflection coefficient
r_s	:	s-polarized reflection coefficient
$\boldsymbol{rr}$	:	reflection coefficient

t_p	:	s-polarized transmission coefficient
t_s	:	s-polarized transmission coefficient
tt	:	transmission coefficient
α	:	absorption coefficient
γ_p	:	plasmon broadening parameter
ε	:	complex dielectric function
ε_∞	:	high-frequency limit of dielectric constant
ε_i	:	imaginary part of dielectric function
ε_r	:	real part of dielectric function
$\varepsilon^{FC}(\omega)$	:	free-carrier dielectric function
$\varepsilon_{imp}(\omega)$	:	impurity dielectric function
$\varepsilon_{int}(\omega)$	:	instrinsic dielectric function
$\varepsilon^{L}(\omega)$	:	lattice dielectric function
θ_i	:	incident angle
λ	:	wavelength
μ	:	mobility
χ	:	electric susceptibility
ρ	:	complex reflectance ratio
τ_m	:	relaxation time
φ	:	work function
ω	:	frequency
ω_{LO}	:	longitudinal optical phonon frequency

ω_p : plasma frequency

ω_{TO} : transverse optical phonon frequency

ABBREVIATIONS

AFM	**:**	Atomic force microscopy
ALD	**:**	Atomic layer deposition
ALE	**:**	Atomic layer epitaxy
BE	**:**	Binding energy
CMOS	**:**	Complementary metal-oxide-semiconductor
CVD	**:**	Chemical vapor deposition
DRAM	**:**	Dynamic random access memory
DTSG	**:**	Deuterium triglycine sulfate
ECR	**:**	Electron cyclotron resonance
EL	**:**	Electroluminescent
EMA	**:**	Effective medium theory
FTIR	**:**	Fourier transform infrared
FWHM	**:**	Full width of at half-maximum
GIXRD	**:**	Grazing incidence x-ray diffraction
GPC	**:**	Growth per cycle
HC	**:**	Hollow-cathode
HCPA-ALD	**:**	Hollow cathode-plasma assisted atomic layer deposition
HVPE	**:**	Hydride vapor phase epitaxy
ICP	**:**	Inductively-coupled plasma
IRSE	**:**	Infrared spectroscopic ellipsometry
LED	**:**	Light emitting diodes
LO	**:**	Longitudinal optical mode
LPP	**:**	Coupled LO plasmon-phonon

MBE	**:**	Molecular beam epitaxy
MDF	**:**	Model dielectric function
MEMS	**:**	Microelectromechanical systems
MOCVD	**:**	Metalorganic chemical vapor deposition
MOS-FET	**:**	Metal oxide semiconductor field-effect transistor
MSE	**:**	Mean squared error
PA-ALD	**:**	Plasma-assisted atomic layer deposition
PE-ALD	**:**	Plasma-enhanced atomic layer deposition
PSD	**:**	Position-sensitive detector
RF	**:**	Radio frequency
RMS	**:**	Root mean square
SE	**:**	Spectroscopic ellipsometry
SPM	**:**	Scanning probe microscope
TFEL	**:**	Thin film electroluminescent
TO	**:**	Transverse optical mode
XPS	**:**	X-ray photoelectron spectroscopy
XRD	**:**	X-ray diffraction

LIST OF FIGURES

Figure 2.1. Schematic representation of the typical atomic layer deposition cycle for binary compound material. 3

Figure 2.2. Deposition temperature-dependent change of ALD growth rate. 6

Figure 2.3. The GPC dependency on reaction cycle number different types of ALD processes, (a) linear growth, (b) substrate-enhanced growth, (c) substrate-inhibited growth of Type 1, and (d) substrate-inhibited growth of Type 2. [48] 6

Figure 2.4. Dependency of GPC on the substrate. Substrate-enhanced growth of (a) GaN on Si(100) (b) GaN on sapphire, and (c) GaN on quartz with different thicknesses grown by HCPA-ALD. The red line depicts the extrapolation of the steady-state GPC in order to better capture the shift of the GPC. 7

Figure 2.5. Remote-plasma configurations for PE-ALD[50]. 8

Figure 3.1. Frequency-dependent dielectric permittivity spectrum. ε_r and ε_i indicate the real and the imaginary part of the permittivity, respectively [71]. 12

Figure 3.2. The influence of frequency dependent damping constant on real and imaginary part of (a) the dielectric function, (b) the index of refraction of GaN vs energy; dotted line- MDF and solid line-modified MDF with frequency dependent damping constant. 16

Figure 3.3. An unbroadened, generic critical point structure composed of four component polynomials, F_I, F_{II}, F_{III}, and F_{IV} [85]. 17

Figure 3.4. Schematic representation of the wurtzite crystal structure of binary group-III nitrides [88]. 19

Figure 3.5. Displacement pattern for the six optical Γ-point phonon modes in the wurtzite structure [89]. 20

Figure 3.6. A comparison of theoretically predicted using Eq. 3.22 and experimentally derived E_1-LPP modes behavior of (a) GaN on Si(100) and (b) InN on sapphire grown by HC-PAALD. 22

Figure 3.7. Coordinate system for measuring the *E* vectors of a plane wave reflected and refracted at a boundary between a medium of refractive index n_1 and a medium of refractive index n_2 [104]. 26

Figure 3.8. The path of the electromagnetic wave in a multi-layered structure 27

Figure 3.9. Schematic diagram of an ellipsometer 29

Figure 3.10. Schematic diagram of an IR-ellipsometer [109] 30

Figure 3.11. (a) Influence of backside reflection on ellipsometric Ψ data of GaN grown on double-side polished Si(111) and schematic representation of (b) reflection from the backside of the substrate [112] (c) roughened Si substrate on the backside [112]. 31

Figure 3.12. Influence of IR beam size on (a) p-polarized (R_p) and (d) s-polarized (R_s) reflection data of GaN on sapphire at 80 degrees, IRSE sample stage (b) with mask and (c) without mask 32

Figure 3.13. Schematic representation of X-ray diffraction 33

Figure 3.14. An illustration energy-level diagram of photoemission from the core and valence bands level in a solid [69]. 34

Figure 3.15. The typical force-distance curve and different regimes and modes of the tip-surface interaction in an AFM [100]. 35

Figure 4.1. GIXRD patterns of GaN thin films with different thickness on Si(100) substrate. 40

Figure 4.2. High resolution XPS scans of (a) Ga 3d and (b) N 1s for GaN films of different thickness on Si(100) at 200 °C. 44

Figure 4.3. AFM images of GaN films with different thicknesses (a) 5.37 nm, (b) 21.01 nm, (c) 48.65 nm, and (d) 81.40 nm. 47

Figure 4.4. Ellipsometry spectra of (a) 5.37 nm and (b) 81.40 nm GaN films grown on Si(100) at room temperature (circle) compared with calculations (solid line). 49

Figure 4.5. Evolution of (a) the refractive index and (b) extinction coefficient as a function of the wavelength for GaN having different film thicknesses. The inset displays optical band edge values calculated from spectroscopic ellipsometry data. 50

Figure 4.6. The estimated (a) fill fraction (b) strain in GaN films (c) grain size and optical band gap in dependence on the thickness of the GaN films. 51

Figure 4.7. The Raman $E2High$ phonon mode spectra of GaN films and theoretical fit of phonon modes. 56

Figure 4.8. Raman lineshape analysis for the LO-phonon and theoretical fit of A_1(LO) phonon mode. 60

Figure 4.9. Free carrier concentration and E_2^{high} phonon peak position as a function of GaN thickness. 61

Figure 4.10. Ellipsometric angles Ψ and Δ as a function of wavelength for (a)-(b) 20.93 and (c)-(d) 84.35 nm GaN films, grown on sapphire substrates, acquired with incidence angles ranging from 60° to 70°; circles and lines represent experimental data and theoretical fit, respectively. 62

Figure 4.11. Optical functions (a) n and (b) k of the GaN layers calculated using the MDF and best-fit parameters obtained in this work. The inset of (b) shows the square of the absorption coefficient (α^2) vs. photon energy for GaN films with different thickness. 64

Figure 4.12. (a) Fill fraction, (b)surface roughness layer thickness (b), and (c) $E2High$ phonon peak position of the GaN layers obtained from Bruggeman EMA, fitting to the SE data and fitting to the Raman Spectra as a function of the thickness 65

Figure 4.13. Band gap of the GaN layers with various thicknesses obtained from the exploration of $(\alpha(E))^2$ vs E. FWHM of the $E2High$ phonons of GaN as a function of the thickness obtained from the analysis of Raman Spectra. 66

Figure 4.14. Experimental (dot) and calculated (solid lines) IRSE (a) Ψ and (b) Δ spectra of GaN films studied at 72° angle of incidence. The spectra of a bare sapphire substrate are included for comparison. The phonon modes are indicated by vertical lines. The solid (dotted) brackets indicate IR-active TO(LO) modes of sapphire. 68

Figure 4.15. (a) Refractive index (n) and (b) extinction coefficient (k) of GaN layers with different thickness perpendicular to the *c*-axis obtained from the best fit IRSE data analysis. 72

Figure 4.16. (a) $\boldsymbol{Im\varepsilon} \perp$ and (b) $\boldsymbol{Im-1\varepsilon} \perp$ spectra of all GaN layers obtained from the best fits to the experimental IRSE spectra and showing the E_1(TO) and E_1(LO) modes. 73

Figure 5.1. GIXRD patterns of InN thin films deposited at 200 °C on Si (100) substrates using (a) N_2 (50 sccm), (b) N_2/H_2 (50+25 sccm), and (c) N_2/H_2 (50+50 sccm) plasma. 80

Figure 5.2. XPS of In $3d_{5/2}$ from InN thin films deposited at 200 °C on Si (100) substrates using different N_2/H_2 plasma flows. Solid line and open circles show experimental data and fitted curve, respectively. 81

Figure 5.3. (a) Refractive index (*n*) and (b) extinction coefficient (*k*) for (Al, Ga)N films with different N_2/H_2 flows. 83

Figure 5.4. (a) Refractive index (*n*) and (b) extinction coefficient (*k*) for InN films deposited using different N_2/H_2 flows. (c) and (d) Structural sketch for InN films deposited using N_2/H_2 plasma. 84

Figure 5.5. Optical absorption coefficient plots of (a) GaN, (b) AlN, and (c) InN films deposited on Si (100) substrates using different N_2/H_2 flow rates. The inset shows the optical band gap and refractive index versus hydrogen flows. The optical band gap was extracted from the optical absorption coefficient. 85

Figure 5.6. Experimental (dashed lines) and best-fit (solid lines) IR ellipsometric Ψ spectra of the (a) GaN, (b) AlN, (c) InN films deposited using N_2/H_2 and N_2 plasma. E_1(TO), A_1(LO) and E_1(TO) phonon modes of GaN, AlN and InN films were deposited on Si(100) substrates using different N_2/H_2 flow rates. Dashed lines are reported frequencies of phonon modes in the literature for strain free structures. 87

LIST OF TABLES

Table 3.1. Raman configurations of allowed in hexagonal nitrides 24

Table 4.1. Lattice constants and elastic strain (in parallel (ε_{xx}) and perpendicular (ε_{zz}) directions) in the GaN layers. The negative values of calculated strain show the existence of compressive strain while the positive value denotes tensile strain. 42

Table 4.2. Elemental at. % of GaN grown on Si(100) as extracted from XPS survey scans. 43

Table 4.3. Relative percentage of different bonding states in the Ga 3d core-level spectra (Fig. 4.2 (a)) and N 1s core level spectra (Fig. 4.2 (b)) of the grown GaN films. 45

Table 4.4. Grain size and RMS roughness values of GaN layers determined from AFM images. 46

Table 4.5. The Phonon frequencies (for q=0) of GaN films at room temperature 58

Table 4.6. The Best-fit values of GaN from the IRSE data analysis for layer thickness d, GaN lattice phonon frequencies, high frequency dielectric constant, and the broadening values of the TO and LO phonon modes. The error limits, which correspond to 90% reliability, are given in parentheses. 71

Table 5.1. E_1(TO), A_1(LO) and E_1(LO) phonon frequencies (cm^{-1}) of GaN, AlN and InN deposited using N_2/H_2 and N_2 plasma 89

1. INTRODUCTION

AlN, GaN and InN have attracted enormous attention due to their strong potential for applications in optoelectronic and electronic devices [1, 2]. (Al, Ga, In)N alloy system with a direct band gap ranging from 0.7 to 6.1 eV allows tunable band gaps of ternary or quaternary alloy systems within specified limits for a particular application [3]. The growth of high-quality epitaxial III-Nitrides (III-N) layers were achieved by using metal organic chemical vapor deposition (MOCVD) and molecular beam epitaxy (MBE) which require high growth temperatures for GaN and AlN (>800 °C). However, the large thermal decomposition pressure of InN and indium-rich group III-Nitride limits the potentials of the growth of narrow band gap III-Nitride heterostructures to be used in spectral tunable light sources and highly efficient photovoltaic converters [4]. Nevertheless, integrations of low band gap (In-rich) group III-Nitride alloys into wide band gap (Ga-rich) group III-Nitride alloys are possible by applying low growth temperature. There are alternative approaches for low-temperature growth of group III-Nitride binaries such as sputtering, pulsed laser deposition, and plasma-assisted atomic layer deposition (PA-ALD) [5–9]. PA-ALD emerges as an interesting, alternative deposition technique to grow III-Nitride thin films and their alloys at low growth temperatures and it is compatible to grow temperature sensitive structures for the integration with existing Si technology.

Atomic layer deposition (ALD) is a unique kind of chemical vapor deposition (CVD) process dependent on sequential and self-terminating gas-solid surface responses. Rather than CVD, the film growth in ALD has a *self-limiting* growth mechanism. In ALD, the precursor gases are separated by purging (and/or evacuation time) and pulsed into the reactor sequential, non-overlapping pulses (which provides the saturative surface reactions), thereby preventing chemical reactions between the precursor molecules in the gas phase. This mechanism allows the growth of films with large-area uniformity, good reproducibility, ultimate conformality, and stoichiometric control, which can be controlled at the atomic level with ALD at low-temperature [10]. ALD's ability to produce substrate-independent film growth allows ALD to be widely used in many different technology/industry fields such as metal oxide semiconductor field-effect transistor (MOS-FET) [11] and dynamic random access memory (DRAM) [12] production in

microelectronics, microelectromechanical systems (MEMS) [13], thin-film electroluminescent (EL) displays, solar energy, coating of fibers [14] .

ALD's concept was first studied by Prof. V.B. Aleskovskii's PhD work in 1952 with the name of "Molecular Layering". In 1970s, ALD was world widely introduced under the name "Atomic Layer Epitaxy (ALE)" by Dr. Suntola and his co-workers. The first commercially significant application of ALD was conceived in Finland in mid-1980's during which a thin film electroluminescent (TFEL) display based on ALD of ZnS:Mn [15]. With the growing interest in the silicon-based microelectronics industry methodology interest in the ALD began to increase with increasing interest in the method of the silicon-based microelectronics industry from the late 1990s to the early 2000s, [16–18]. Also at that time, the term atomic layer deposition was revealed. This increase was most prominent in highly insulating oxide films to be used as low-leakage high-k dielectrics in complementary metal-oxide-semiconductor (CMOS) transistors and DRAM devices. The library of materials feasible by ALD, including nitride-based semiconductors (AlN [19–25], GaN [7, 26], InN [26]), metal oxides (Al_2O_3 [27–29], TiO_2 [30], SnO_2 [31], ZnO [32–36], HfO_2 [37]) , nitrides (TiN [38], TaN [39], NbN [40]), perovskite oxides[41], carbides, chalcogenides, metals (Ru [42], Ir [43], Pt), etc., has significantly expanded over the last decades [44].

This thesis is divided into six chapters. Chapter 2 describes the basic principles and background of ALD of thin films with a motivation on the thin film materials themselves. The most important thin film characterization methods used in this thesis and the theoretical background for modeling are explained in Chapter 3. Chapter 4 discusses the properties of GaN to understand substrate and thickness effect, while the effect of plasma gas composition on the properties of deposited binary III-Nitride thin films (AlN, GaN and InN) analyzed in Chapter 5. Finally, Chapter 6 summarizes and concludes the thesis.

2. ATOMIC LAYER DEPOSITION

2.1. Basic Concepts and Principles of ALD

ALD is a thin film deposition technique that ALD reactions use gases called precursors. Two or more gaseous precursors or chemical vapors which have separately purging and/or evacuation periods react sequentially, on the substrate surface in order to grow layer-by-layer solid thin film. Therefore, ALD is a cyclical film growth process. ALD film growth process for binary compounds as shown in Figure 2.1 occurs with the repetition of four steps.

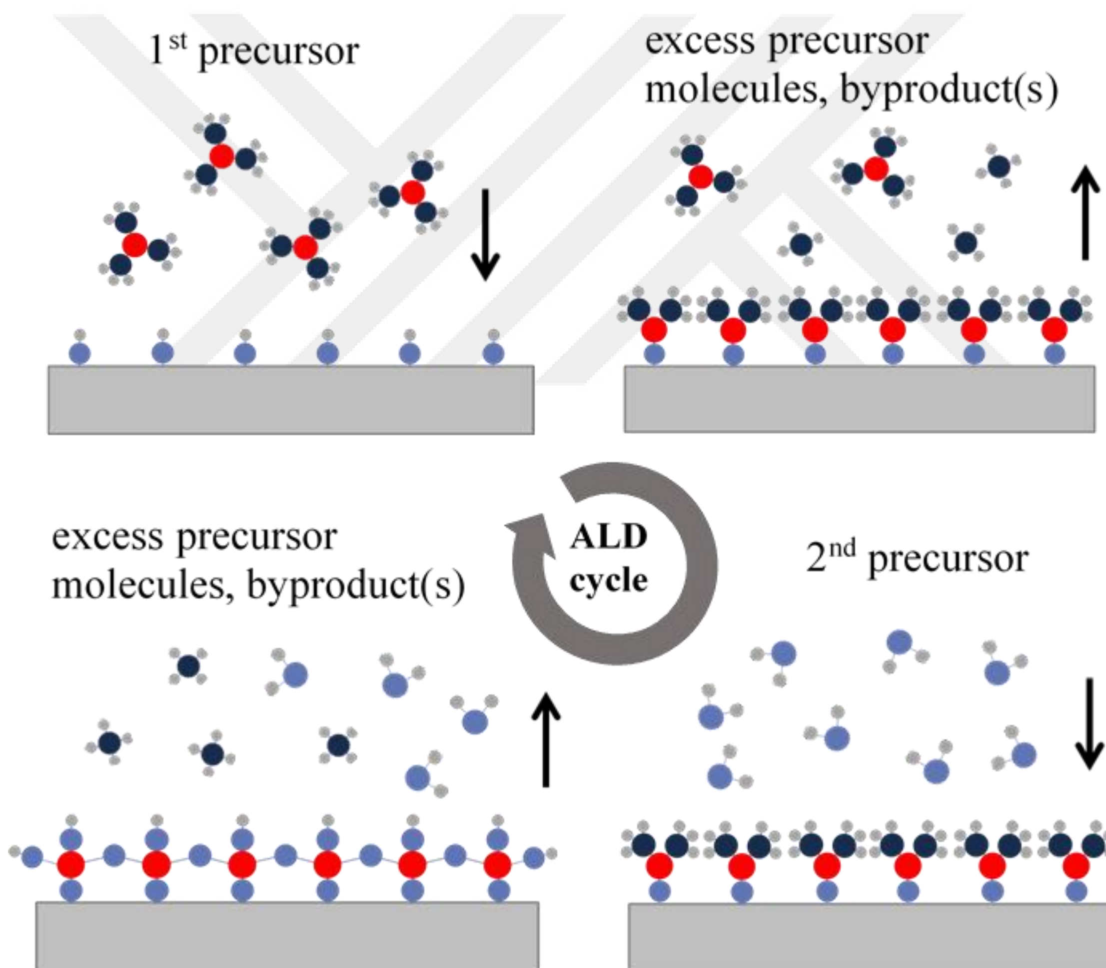

Figure 2.1. Schematic representation of the typical atomic layer deposition cycle for binary compound material.

1. Exposure of the first precursor
2. Purge and/or evacuation to remove non-reacted precursor molecules and gaseous by-products
3. Exposure of the second precursor (occasionally referred as the reactant)
4. Purge and/or evacuation to remove non-reacted precursor (reactant) molecules and gaseous by-products [14, 45]

In ALD, it is important that the reactant reacts with the precursor in a self-limiting manner. Besides, the reactive and precursors should not react with themselves or with the new surface groups they form (Step 1 and 2). During step 3 or 4, the newly produced gaseous reaction products and co-reactant molecules and/or residual precursor are removed from the ALD reactor. Unless decomposition occurs, same amount of material is deposited in each cycle which is generally referred to as growth per cycle (GPC) having a unit of angström per cycle. The thickness of the thin film can be controlled by the accuracy of the sub-nanometer by controlling only the number of reaction cycles, under conditions where the ALD processing conditions (adsorption kinetics, chemisorption mechanisms, etc.) are conducive to self-terminating reactions. Because of its exceptional "*self-limiting*" growth mechanism, uniform and conformal thin films can be grown with the ALD technique [45, 46].

2.2. Atomic Layer Deposition Growth Mechanisms

2.2.1. Reactants and surface chemistry

The reactants used for ALD processes should have high enough reactivity with respect to the growth surface. Consequently, the selected precursor must be volatile either at room temperature or at higher temperatures and stable against self-decomposition within the ALD processing temperature [45]. if the self-limiting thin film growth mechanism would be destroyed by self-decomposition of the precursor molecules, the growth will result in a CVD-like growth regime[45]. Moreover, the selected precursor should go through aggressive and complete reactions, cause no etching reactions, not to be dissolved to the film or substrate, and produce stable, non-reactive volatile by products, which can be easily purged out from the reactor [47].

The purge time of precursors must be of sufficient length so that they do not meet each other in the gas phase. If the purge time is less than this time, precursors that encounter each other in the gas phase cause undesired CVD-like growth and reduce the control of thickness, conformality and result in non-uniform growth. If it is longer than this, it may cause desorption of surface-bonded species. Purge time is also affected reactor's base pressure, flow dynamic, the stiction tendency of the precursor to surfaces and topography of the substrate[46]. Furthermore, the dose and pressure of the reactant, which is carried by an inert carrier gas such as N_2, Ar to the ALD reactor should also be considered in ALD processes. If the dose of the reactant is sufficient for the desired ALD reactions, all accessible and reactive surface areas are saturated with the chemisorption reaction.

2.2.2. Temperature effects

Different types of growth rate are given in Figure 2.2 in comparison with temperature. When the GPC process is applied at temperatures that provide a sufficiently high thermal energy for the chemical reaction, the growth rate generally remains constant relative to the growth temperature. This temperature window is often referred to as *ALD window* where an ALD process fulfills the requirement of self-terminating reactions. In many cases, the growth rate at low temperatures increases with increasing temperature (generally below 150-300 ° C for most metals and nitrates). This is mainly because of the precursor adsorption or reaction between precursor and surface species is a thermally activated process. Thus, the saturation reaction is kinetically limited with low thermal energy. Moreover, the GPC decreases if precursor(s) condensate as solid physisorbed layers on the substrate. At temperatures above this temperature, the self-limiting growth is disrupted because of the decomposition of the metal precursor gases and the growth rate generally increases with the growth temperature (like CVD process). While this thermal decomposition is no problem for high thermal stability halide precursors (fluoride, chloride, bromide and iodide), the metal organic precursors which generally decompose at a relatively lower growth temperature. For example, the thermal-ALD processing temperature for metals and nitrates is between 150-250 ° C for metal organic precursors and 300-500 ° C for halide precursors, respectively. In several material systems, when thermal desorption occurs in the film, the growth rate decreases with increasing growth temperature [47].

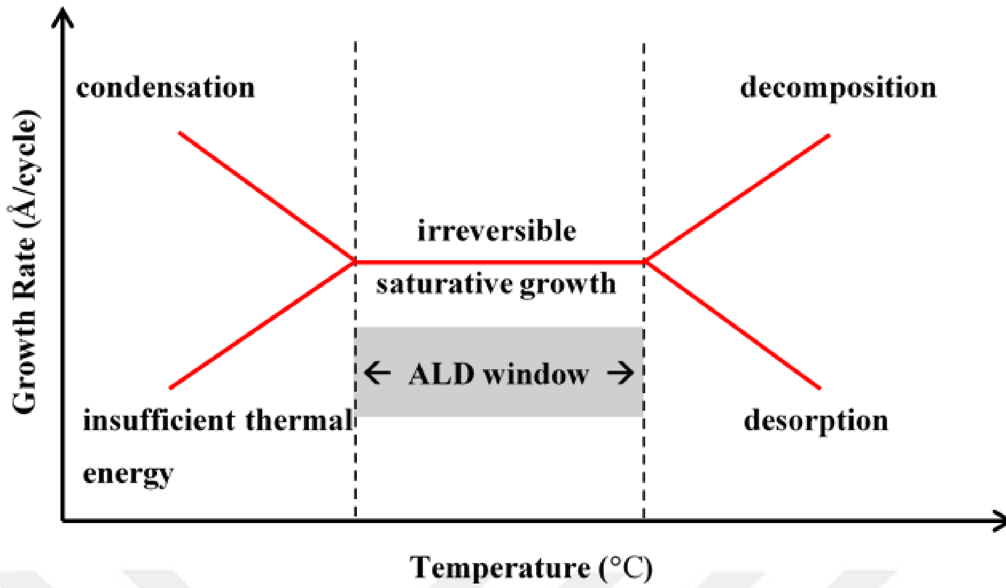

Figure 2.2. Deposition temperature-dependent change of ALD growth rate.

2.2.3. Substrate effect and growth inhibition

Basically, GPC can be divided into four groups according to the number of ALD reaction cycles. Fig. 2.3 illustrates substrate-induced effects on the GPC. The first of these substrate effects is *linear growth* (Fig. 2.3(a)), where the growth is consistently stable without substrate effects and the GPC is stable starting from the first cycle. This effect can occur if the reactive areas on the surface do not alter depending on the number of cycles [48].

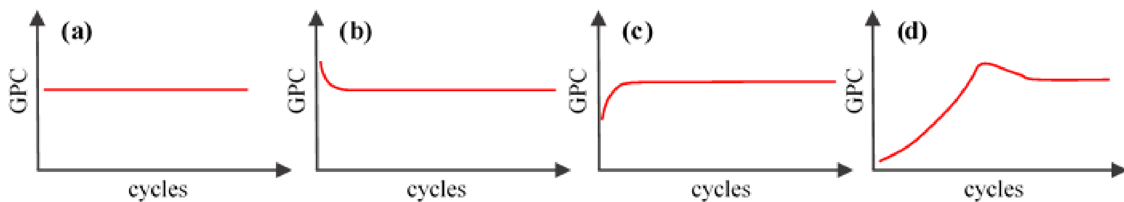

Figure 2.3. The GPC dependency on reaction cycle number different types of ALD processes, (a) linear growth, (b) substrate-enhanced growth, (c) substrate-inhibited growth of Type 1, and (d) substrate-inhibited growth of Type 2. [48]

The second effect is *substrate-enhanced growth* (Fig. 2.3(b)). at which GPC is higher than the steady regime at the beginning of growth. It may occur if reactive areas number on the substrate is higher than the ALD grown material. Finally, it is *substrate-inhibited*

growth of Type 1 and Type 2 (Fig. 2.3(c) and (d)), where GPC is lower than the steady regime at initial steps of the growth. The growth inhibited by the substrate results in lower number of reactive sites on the substrate than on the ALD-grown material. For example, by-products or the reactants etch the film during the initial growth [46]. In Type 2 growth, island growth further seems to occur, the GPC additionally passes a maximum value before settling into the constant value. In all four cases, the GPC is expected to settle to a constant value after a sufficient number of ALD cycles [48].

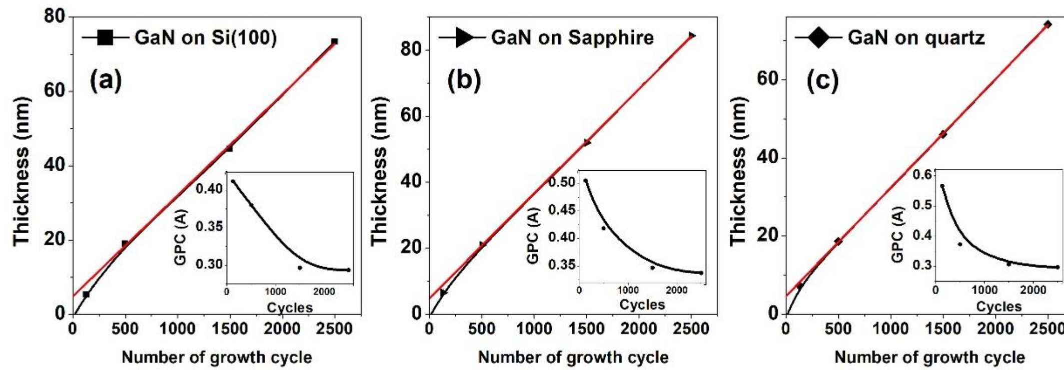

Figure 2.4. Dependency of GPC on the substrate. Substrate-enhanced growth of **(a)** GaN on Si(100) **(b)** GaN on sapphire, and **(c)** GaN on quartz with different thicknesses grown by HCPA-ALD. The red line depicts the extrapolation of the steady-state GPC in order to better capture the shift of the GPC.

Figure 2.4 indicates the variation of the thickness of GaN thin films with different substrates for different number of growth cycles. The red line delineates the extrapolation of the steady-state GPC so as to better capture the shift of the GPC. In addition, inset figures show the variation of GPC according the number of cycles. As seen in Figure 2.4, GaN thin films grown in this study exhibit substrate-enhanced growth. Substrate-enhanced growth occurs when reacted atoms or molecules diffuse deeper in the substrate instead of just forming abrupt interface due to plasma pretreatment [46].

2.3. Plasma Enhanced Atomic Layer Deposition

Plasma-enhanced atomic layer deposition (PE-ALD) (also referred as plasma-assisted ALD, PA-ALD) has the plasma source, which creates radicals, ions, and enhances the chemical reactions on the film growth surface. The activation energy required to provide

exchange reactions between precursor molecules and substrate surface is provided in thermal ALD (the conventional mode of ALD) by thermally heating only the substrate or the entire reactor chamber, whereas in PA-ALD it is provided by highly reactive plasma species. It is appreciated especially when the thin films are deposited on temperature-sensitive and challenging or inaccessible growth regime by the means of thermal ALD.

Due to the enhancement of chemical reactions, PE-ALD enables higher growth rate, the wider choice of precursors, and process versatility, highly pure films. Although PE-ALD has more complicated reactor designs and reaction chemistry, limited conformality, potential plasma damage, its low deposition temperature makes it valuable for some applications such as DRAM, capacitors, etc.

PE-ALD reactor configurations are typically classified into four types: radical-enhanced, direct plasma, remote plasma and hybrid plasma [49]. In this thesis, remote plasma source is used. Therefore, only remote plasma reactor configuration will be discussed. Readers can find other reactor configurations and PE-ALD setups which have different reactor design, plasma radical delivery solutions and/or plasma sources in detail from Ref.49,50.

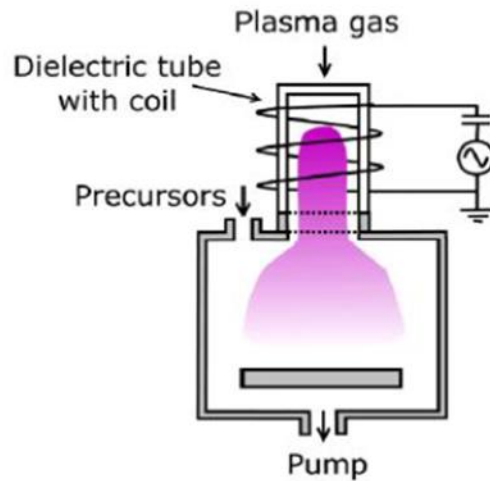

Figure 2.5. Remote-plasma configurations for PE-ALD[50].

In remote plasma configurations depicted in Fig. 2.5, the plasma source is located remotely spatially upstream from the reactor space stage such that the substrate is not involved in plasma generation. This configuration has the generation of "downstream" plasma, high flux of the radicals. This provides the possibility to influence the substrate

level by radical flow, radiation control and ion bombardment. High degree of flexibility makes remote plasma ALD reactors suitable for process design and other R & D applications [51].

Several plasma sources can be used in remote-plasma ALD systems, such as microwave plasma [52], electron cyclotron resonance (ECR) [53] plasma, radio frequency (RF)-driven inductively-coupled plasma (ICP) [7, 22, 54] and hollow-cathode (HC) [55–58] plasma. The plasma system used in this thesis study is a remote-plasma ALD system with RF-driven HC plasma source.

2.4. Opportunities and Challenges

Characteristic feature of ALD, the inherent implication of these features on the film and practical advantages of film deposition (summarized by Ritala and Leskela in Ref. [59]) are listed below.

- *Self-limiting growth process*

  Film thickness depends on the control of the deposition cycle number and it is possible to control the material composition at the sub-atomic level. Thus, the ALD method has accurate and precise thickness control, capability to produce sharp interfaces, superlattices, and possibility to modify interface. In addition, in ALD processes, there is no need of reactant flux homogeneity. Therefore, the ALD method gives practical advantages that can be listed as large-area capability, excellent conformity, large-batch capability, good reproducibility, straightforward scale-up.

- *Separate dosing of reactants*

  In the ALD processes, there is no reaction in the gas phase in the reactor chamber, as well as sufficient time to complete each reaction step. Highly reactive precursors to each other are preferred so that effective material usage and high-quality material are obtained at low temperatures.

- *Processing temperature windows are often wide*

  The large temperature window makes it possible to easily match the processing conditions of different materials. This allows multi-layered structures to be prepared in a continuous process.

At low temperatures, atomic-level control of material compositions enables conformal and uniform material growth, allowing the growth of materials such as doped[60, 61] , alloys[62], graded[63] thin films, quantum wells[64], superlattices[65] and nanolaminates, as well as temperature-sensitive organic substrates [66–68].

The disadvantage of ALD growth method is that the process of ALD is very slow due to monolayer film growth during one cycle. ALD is typically used in microelectronics and nanotechnology, and therefore, thick layers are not required. One of the reasons that prevent ALD from becoming widespread is that the precursor gases required for some materials are expensive [59].

3. OPTICAL PROPERTIES OF SEMICONDUCTOR AND MATERIAL CHARACTERIZATION

3.1. Optical Constants and the Dielectric Function

The interaction of electromagnetic radiation with semiconductors can be defined using a response function such as the dielectric function (ε) and the electric susceptibility (χ) in a semi-classical regime. These definitions can be reduced to an appropriate model item with ε and χ, where it is considered to be the experimentally observed optical behavior and the physical characteristics of the semiconductors. χ and ε are defined by the following equations in the linear region for the isotropic solid [69].

$$\boldsymbol{D} = \varepsilon_0 \boldsymbol{E} + \boldsymbol{P} = \varepsilon_0 \left(1 + \chi\right) \boldsymbol{E} \tag{3.1}$$

$$\boldsymbol{D} = \varepsilon \boldsymbol{E} = \left(\varepsilon_r - i\varepsilon_i\right) \boldsymbol{E} \tag{3.2}$$

where, ***E, D***, and ***P*** are the free-space electric field, the displacement field and the polarization field inside the semiconductor, respectively. ε_0 is permittivity of the empty space and χ is the electric susceptibility. ε and χ are dimensionless quantities [69]. The complex refractive index of the thin film is equal to the square root of the complex dielectric function given as in the following.

$$\tilde{n} = \sqrt{\tilde{\varepsilon}} = \sqrt{\left(\varepsilon_r - i\varepsilon_i\right)} = n - ik \tag{3.3}$$

The real and imaginary part of the refractive index, n and k, also called optical constants, embody and represent the linear optical properties of a material in terms of how an electromagnetic wave will propagate in that material [70]. For example, the real component n gives the phase velocity of light in the material. The imaginary component k represents the light absorption by the semiconductor and is associated with the absorption coefficient. In the spectral region where absorptive processes are weak or absent, as in the case of the sub-bandgap range, k is very small, whereas in regions of strong absorption, the magnitude of k is large. For most cases of optical absorption, the energy absorbed is proportional to the thickness of the film. The attenuation of the radiation intensity (not electric field) inside the absorptive medium is given by the

following relationship (Beer-Lambert law) with absorption coefficient (measured in cm^{-1}) $\alpha = 4\pi k/\lambda$ [69] .

$$I(x) = I_0 e^{-\alpha x} \quad (3.4)$$

3.2. Models of Dielectric Function

The dielectric function, $\varepsilon(\omega)$ can fully define the interaction of light with semiconductors. Alternatively, similar information about how the material reacts to the applied electric field (like n and k) can be obtained from the real and imaginary parts of the dielectric functions [69].

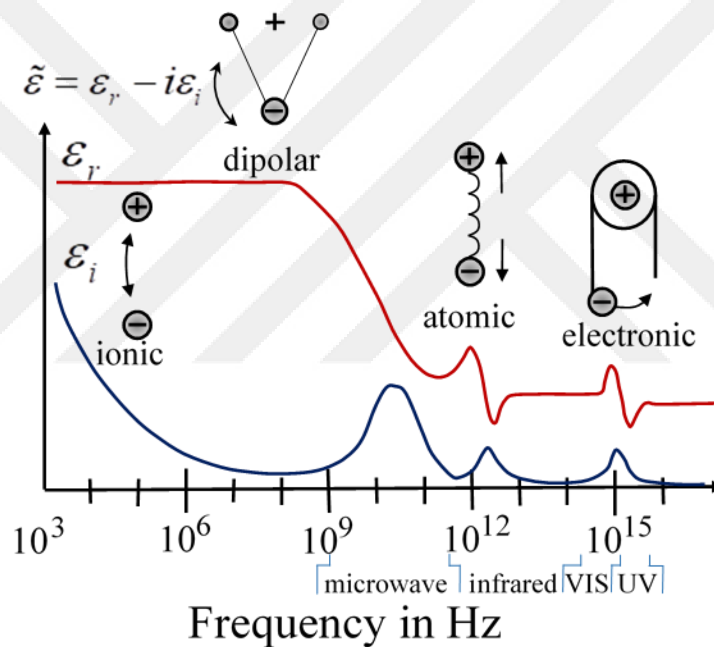

Figure 3.1. Frequency-dependent dielectric permittivity spectrum. ε_r and ε_i indicate the real and the imaginary part of the permittivity, respectively [71].

The response of materials to external fields generally depends on the frequency of the field as a result of a material's polarization not changing instantaneously. Figure 3.1 displays a dielectric permittivity spectrum through a wide range of frequencies. ε_r and ε_i indicate the real and the imaginary part of the permittivity, respectively. Different processes are labeled on the graph: ionic, dipolar relaxation, atomic and electronic resonances at higher energies [71].

In order to define various physical mechanisms, it is possible to divide the dielectric function into different independent parts, provided that the processes do not interact strongly with each other. Three of the most important mechanisms explaining the linear optical behavior of an intrinsic semiconductor are determined by electronic transitions (between the energy states available to the electrons), lattice vibrations, and free-carrier effects (i.e., mobile electrons and holes) [69].

$$\varepsilon_{\text{int}}\left(\omega\right)=\varepsilon^{L}\left(\omega\right)+\varepsilon^{FC}\left(\omega\right)+\varepsilon^{inter}\left(\omega\right) \tag{3.5}$$

In addition to these properties, impurities and dopants (especially critical in the control of electronic properties) lead to an additional contribution to the dielectric function [69], and it can be described as in following.

$$\varepsilon\left(\omega\right)=\varepsilon_{\text{int}}\left(\omega\right)+\varepsilon_{imp}\left(\omega\right) \tag{3.6}$$

The complex permeability is a frequency-dependent ω and overlapping description of dispersion phenomena that occur at different frequencies. Since the dominant physical process depends on the material and spectral region of interest, the permittivity in narrow frequency ranges (often studied in practice) can be approached independently of frequency or by model functions. Therefore, the dielectric function at different frequency regions should be represented by a suitable model. In particular, the models used in this thesis will be discussed below.

3.2.1. Electronic transition

Electronic transitions in a solid begin at the material's bandgap that generally marks the end (upper frequency) of a material's useful transparency. Above the bandgap, the material is highly reflective due to broad featured spectra produced by a large number of possible electronic transitions [69]. The dielectric constant in the transparent region, between electronic and vibrational absorption/emission, is (mostly) real. In this region, Sellmeier dispersion model [72, 73], an approximate form to the classical oscillator model, widely used to represent the real part of the relative permittivity across the ultraviolet, visible, and near-infrared spectrum [69].

$$\varepsilon\left(\lambda\right)-1=n^{2}(\lambda)-1=\sum_{i=1}\frac{A_{i}.\lambda^{2}}{\lambda^{2}-\lambda_{i}^{2}} \tag{3.7}$$

where A_i and λ_i are called Sellmeier coefficients. Another model used to parameterize the refractive index within the insignificant absorption region is the Cauchy model [74]. This model is a generalized form of the short-wavelength approximation to the Sellmeier equation[69] that handles anomalously dispersive regions and only valid for normal dispersion regions in the visible wavelength region.

$$\varepsilon(\lambda) = n^2(\lambda) = A_0 + \sum_{i=1} \frac{A_i}{\lambda^{2i}} \tag{3.8}$$

Here, A_0 and A_i are coefficients that can be obtained to fit the measured refractive index using the equation.

Unfortunately, the optical properties of electronic transitions, which are crucial for optoelectronic device performance, cannot be simply modeled because of the many electronic transitions that coupled together to create broad homogeneous absorption bands. However, Adachi [75–77] has developed models that successfully represent the complex dielectric function of electronic transitions as a function of both temperature and frequency by considering the effect of various electronic interband transitions from the valence to the conduction band [69]. This model is called the Model Dielectric Function.

3.2.1.1. Model dielectric function

The model dielectric function implemented by Adachi enables the dielectric function of the material to be obtained by making use of electronic transitions at critical energy points. The model dielectric function for the hexagonal wurtzite structure is described below.

The complex dielectric function as a function of energy $E = \hbar\omega$ is described by the sum of terms corresponding to one-electron contributions at critical points E_0 and $E_{1\beta}$ $(\beta = A, B, C)$, $\varepsilon_0(\hbar\omega)$ and, $\varepsilon_1(\hbar\omega)$ excitonic contributions at those critical point and additive constant ε_∞.

$$\varepsilon(E) = \varepsilon_0(E) + \varepsilon_{0X}(E) + \varepsilon_1(E) + \varepsilon_{1X}(E) + \varepsilon_\infty \tag{3.9}$$

Three-dimensional M_0 critical point contribution E_0 under the parabolic band assumption is given by

$$\varepsilon_0(\hbar\omega) = AE_0^{-3/2}\chi_0^{-2}\left[2-\left(1+\chi_0\right)^{1/2}-\left(1-\chi_0\right)^{1/2}\right] \tag{3.10}$$

$$\chi_0 = \frac{E+i\Gamma_0}{E_0} \tag{3.10a}$$

where; $\Gamma_0\left(eV\right)$ and $A\left(eV^{1.5}\right)$ are the damping constants and strength of E_0 transition, respectively.

$E_{0\beta}$ can be treated as a single degenerate among $\beta = A, B, C$ critical points because of very small splitting energies [77].

Exciton contributions at E_0 are given by

$$\varepsilon_{0X}(\hbar\omega) = \sum_{m=1}^{\infty}\frac{A_0^{ex}}{m^3}\frac{1}{E_0-\left(G_0^{3D}/m^2\right)-E-i\Gamma_0} \tag{3.11}$$

where $G_0^{3D}(eV)$ and $A_0^{ex}(eV)$ are three-dimensional (3D) exciton binding energy and the 3D exciton strength parameter, respectively.

The two-dimensional (2D) M_0 critical points $E_{1\beta}$ contributions are given by

$$\varepsilon_1(\hbar\omega) = -\sum_{\beta=A,B,C} B_{1\beta}\chi_{1\beta}^{-2}\ln\left(1-\chi_{1\beta}^{2}\right) \tag{3.12}$$

$$\chi_{1\beta} = \frac{E+i\Gamma_{1\beta}}{E_{1\beta}} \tag{3.12a}$$

where, $\Gamma_{1\beta}(eV)$ and $B_{1\beta}(eV)$ are damping constants and the strengths of the $E_{1\beta}$ transitions, respectively.

The Wannier type 2D excitons contributions (discrete series of exciton lines at the $E_{1\beta}$)

$$\varepsilon_{1X}(\hbar\omega) = \sum_{\beta=A,B,C}\sum_{m=1}^{\infty}\frac{B_{1\beta}^{X}}{\left(2m-1\right)^3}\times\frac{1}{E_{1\beta}-\left(G_{1\beta}^{2D}/\left(2m-1\right)^2\right)-E-i\Gamma_{1\beta}} \tag{3.13}$$

where $G_{1\beta}^{2D}(eV)$ and $B_{1\beta}^{X}(eV)$ are the binding energies and strengths of the excitons at $E_{1\beta}$ respectively.

The above described model is based on Lorentzian broadening and it is the major shortcomings to describe the absorption processes, (especially in the E_0 critical point region). This situation has already been recognized [78–82]. Kim *et al*.[82] have replaced the damping constant Γ with frequency-dependent damping constant Γ_j in their model in order to overcome this problem [83],

$$\Gamma'_j = \Gamma_j \exp\left[-\alpha\left(\frac{E-E_j}{\Gamma_j}\right)^2\right] \tag{3.14}$$

where Γ_j and α_j ($j=A,B,C$) are adjustable model parameters, while E_j is the critical points energy at which transition occurs. Therefore, the frequency-dependent gamma values defined in Eq. 3.14 are used instead of the gamma values in the equations 3.10-3.13 so that the distribution approaches the Gaussian distribution [83].

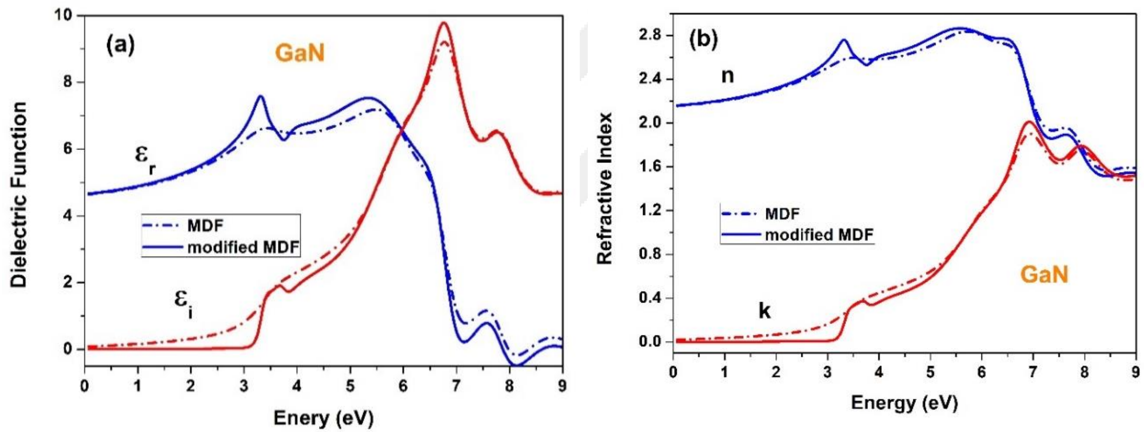

Figure 3.2. The influence of frequency dependent damping constant on real and imaginary part of (a) the dielectric function, (b) the index of refraction of GaN vs energy; dotted line- MDF and solid line-modified MDF with frequency dependent damping constant.

Figure 3.2 shows the effect of the frequency-dependent damping constant on the dielectric function and refractive index of hexagonal GaN which are recalculated by the model parameters obtained by Djurisic *et. al*. [83] dotted and solid line represent conventional MDF and modified-MDF, respectively. As can be seen from the figure, the modified-MDF model exhibits a physically meaningful behavior, especially at and below the

bandgap region, which has already been shown by Djurisic *et. al.*[83] that this model represents experimental data better.

3.2.1.2. The paramedic semiconductor model

The parametric semiconductor model was developed by Craigh Herzinger and Blaine Johns at the J. A. Woollam Co., Inc. [84] and also called *Psemi* in the software (WVASE32). Although there are many published parametric models, this model is based on the Kramers-Kronig consistent model developed by Kim and Garland [82], which can describe a semiconductor's dielectric function and higher-order derivatives model. The differences between the two models and the mathematical definition can be found in detail in ref.82. In addition, in the WVASE32 manual [85], it is possible to find parametric semiconductor model examples for many materials (GaAs, AlAs, GaN, InP, InAs, crystalline germanium, SiGe, crystalline silicon) and to identify different types of psemi oscillators.

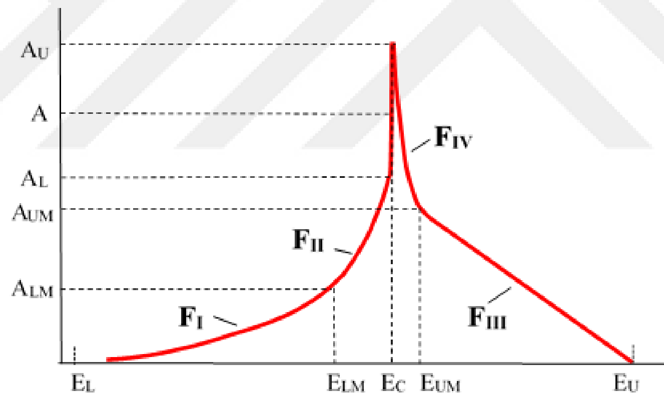

Figure 3.3. An unbroadened, generic critical point structure composed of four component polynomials, F_I, F_{II}, F_{III}, and F_{IV} [85].

To describe the model briefly, each Psemi oscillator consists of four polynomials spline functions (labeled F_I, F_{II}, F_{III}, and F_{IV} in Figure 3.3) connected end-to-end and F_I and F_{III} equal to zero at the boundaries. The polynomials shape can be altered smoothly and continuous by shifting the control points, endpoints, amplitude, and center energy. These features give the model a highly flexible curve to be useful for a very broad range of dielectric and both direct and indirect gap semiconducting materials [85–87]. But it should be remembered that the primary purpose of the Psemi oscillators is to obtain the

optical constants of the material. The parameter values have no direct relationship with the internal physical properties of the material such as critical energy points, broadening that one might obtain from other type of analysis or derivative [85].

3.2.2. Lattice Vibrations

Lattice vibration, or atomic motion, accounts for many material properties, including optical and dielectric properties, elastic constants, heat capacity, and thermal conductivity. The vibrational modes can be subdivided into two major categories: *optical phonons* that possess an oscillating dipole moment (therefore can interact with light) and *acoustic phonons* that do not possess a dipole moment (sound-like vibrations and not of primary significance in determining the optical properties) [69].

There are three types of optical modes: infrared-active, Raman-active, and optically inactive. Infrared-active modes, typically observed between 100 to 4000 cm^{-1} spectral region, are those that (elastically) absorb light owing to an interaction between the electric field in the light and the crystal's dipole moment. Raman modes produced by phonons that modulate the crystal's polarizability to induce a dipole moment weakly absorb light through an inelastic mechanism. Optically inactive modes (silent modes) do not interact with light since they have no induced or permanent dipole moment. Optically active modes, which can be simultaneously Raman- and infrared-active, are experimentally monitored by Raman or infrared spectroscopy, as well as by neutron or x-ray scattering [69].

In crystals, the number of lattice vibrations is equal to three times the number of atoms in the primitive unit cell. However, while crystal symmetries reduce the number of unique lattice vibrations (i.e., introduce vibrational degeneracies), increasing structural disorder (nonstoichiometry, impurities, defects, variable composition) will increase the number of observed infrared-active and Raman-active modes in a real material [69].

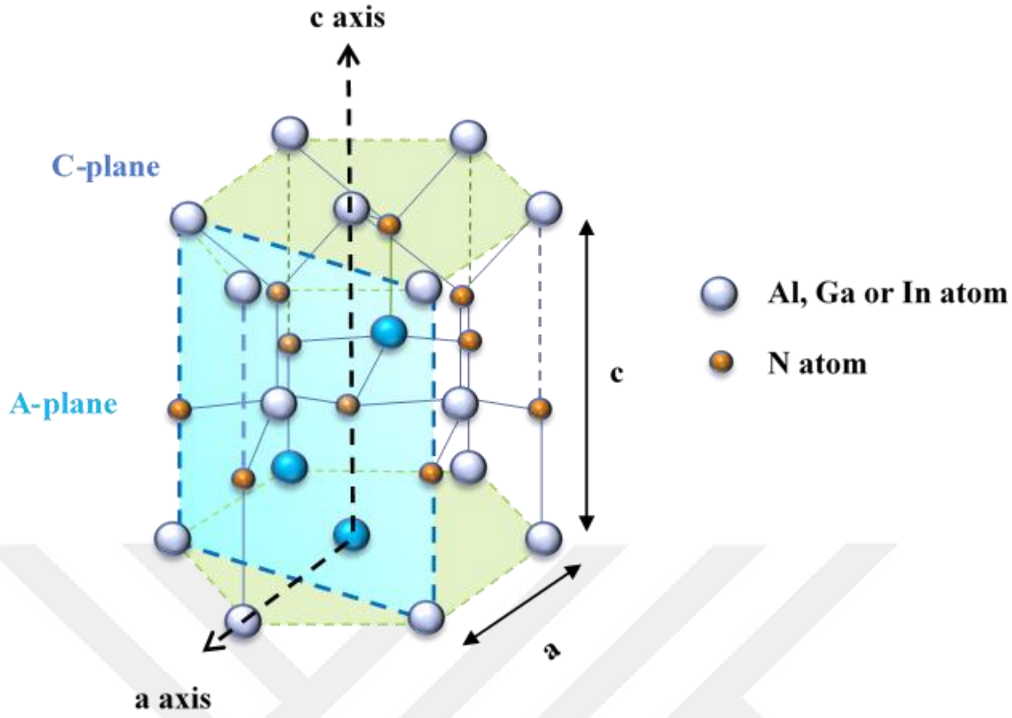

Figure 3.4. Schematic representation of the wurtzite crystal structure of binary group-III nitrides [88].

The binary wurtzite III-nitrides crystalline structure with two formula units in the primitive cell is described by the space group C_{6v}^{4} [89]. Figure 3.4 shows crystal structure of the binary wurtzite-structure of group-III nitrides. The phonons modes at the center of the Brillouin zone (Γ-point) are predicted to be eight sets by group theory, [90]. Among them, one set of E_1 and A_1 are acoustic, and remaining are optical represented by the following irreducible expression [89, 90].

$$\Gamma_{ac} + \Gamma_{opt} = \left(A_1 + E_1\right) + \left(A_1 + 2B_1 + E_1 + 2E_2\right) \tag{3.15}$$

Due to the macroscopic electric fields associated with the longitudinal phonons, both A_1 and E_1 modes split into TO (transverse-mode) and LO (longitudinal-mode) modes and possess different frequencies due to the mode anisotropy caused by the short-range interatomic forces. Since the anisotropy in the short-range forces is dominated by the electrostatic forces dominate, the TO-LO splitting is larger than the A_1-E_1 splitting. The vibrational displacement pattern of the six optical phonon modes observed in the binary wurzite-structure group-III nitrides is shown in figure 3.5 [89]. Both A_1 and E_1 modes

(the atoms move parallel and perpendicular to the c axis, respectively) are Raman and IR-active whereas the E_2 modes (E_2^L, E_2^H) are Raman-active and IR-inactive. The B_1 modes (B_1^L ,B_1^H) are neither IR- nor Raman-active (silent modes) [89, 90].

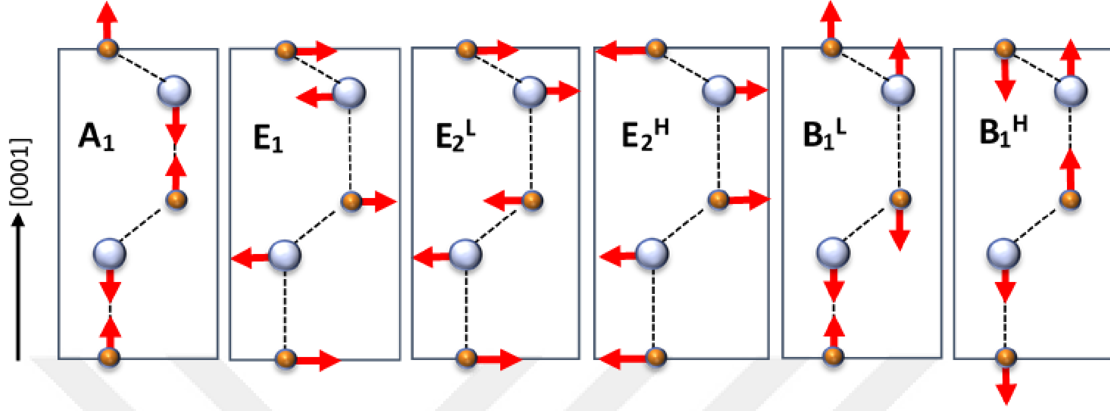

Figure 3.5. Displacement pattern for the six optical Γ-point phonon modes in the wurtzite structure [89].

Optically uniaxial materials (hexagonal and tetragonal crystals) have two principal infrared dielectric functions (hence two n and k). The c axis (or the optical axis) is the unique crystallographic axis. For these materials, the infrared dielectric function is described by following tensor [89].

$$\varepsilon = \begin{pmatrix} \varepsilon_{\perp} & 0 & 0 \\ 0 & \varepsilon_{\perp} & 0 \\ 0 & 0 & \varepsilon_{\parallel} \end{pmatrix} \tag{3.16}$$

where, light propagating along c axis and polarized to the wurtzite c-axis was represented by $\varepsilon_{\perp}$ and $\varepsilon_{\parallel}$, respectively [89].

The infrared dielectric response ε^L at photon energy $\hbar\omega$ can be described harmonic Lorentz oscillators [91–93]. But, in this thesis, the factorized model with the Lorentzian broadening model [92, 93] ,which represent anharmonic effects of phonon coupling represent better, was used especially near phonon mode frequencies. ε^L with the contribution of l polar crystal lattice modes represented by Eq. 3.17 ($j = \perp, \parallel$),

$$\varepsilon_j^L = \varepsilon_{\infty,j} \prod_{i=1}^{l} \frac{\omega_{LO,ij}^2 - \omega^2 + i\gamma_{LO,ij}\omega}{\omega_{TO,ij}^2 - \omega^2 + i\gamma_{TO,ij}\omega} \tag{3.17}$$

where ω_{TO} ,ω_{LO} ,γ_{TO} , and γ_{LO} are the TO, and LO-phonon frequencies, and broadening parameters, respectively while $\varepsilon_{\infty,j}$ is the high frequency limits. ε(ω) is negative for $\boldsymbol{\omega_{TO} \geq \omega \geq \omega_{LO}}$, (Reststrahlen band) which indicates no light propagation inside the crystal and total reflection of the incident light [69]. In order to yield $\mathrm{Im}\left\{\varepsilon^{L}\left(\omega\right)\right\}_{\omega\to\infty} \geq 0$ (necessary for physical meaning), generalized Lowndes condition specified in Eq. 3.18 must be fulfilled [94, 95].

$$\sum_{i=1}^{l}\gamma_{LO,i} \geq \sum_{i=1}^{l}\gamma_{TO,i} \tag{3.18}$$

3.2.3. Free-carrier contribution

The classical Drude approximation generally represents the contribution of a free carrier species to the dielectric function ε^{FC} [96, 97].

$$\varepsilon_{j}^{FC} = -\varepsilon_{\infty,j}\frac{\omega_{p,j}^{2}}{\omega\left(\omega+i\gamma_{p,j}\right)} \tag{3.19}$$

with

$$\omega_{p,j} = \left(\frac{Ne^{2}}{\varepsilon_{\infty,j}\varepsilon_{0}m_{j}^{*}}\right)^{1/2} \tag{3.20}$$

Here, ω_p, ε_0, e, N, and m^* represent, in order, the plasma frequency, dielectric permittivity of free space, magnitude of the electron charge, carrier concentration and effective mass. The inverse of the energy-averaged carrier-momentum relaxation time $\langle\tau_m\rangle_j$ relates to the plasmon broadening parameters $\gamma_{p,j}$.

$$\gamma_{p,j} \equiv \left(\langle\tau_{m}\rangle_{j}\right)^{-1} = \frac{e}{m_{j}\mu_{j}} \tag{3.21}$$

The plasma modes (or plasmons) that collective excitation modes are formed by free charge carriers will couple to the LO lattice modes and form the so-called LPP modes (coupled LO plasmon-phonon) which influence the dielectric function [89].

The lower (upper) LPP mode frequencies $\tilde{\omega}_{LO,1j}$ ($\tilde{\omega}_{LO,2j}$) are found with the square root of $\varepsilon_j = \varepsilon_j^L + \varepsilon_j^{FC}$ under the condition that damping is neglected ($\gamma_{TO,j} = \gamma_{LO,j} = \gamma_{p,j} = 0$; $i = 1,2$; $j = \perp, \|$).

$$\tilde{\omega}_{LO,ij} = \left\{ \frac{1}{2} \left[\omega_{LO,j}^2 + \omega_{p,j}^2 + (-1)^j \sqrt{\left(\omega_{LO,j}^2 + \omega_{p,j}^2\right)^2 - 4\omega_{p,j}^2 \omega_{TO,j}^2} \right] \right\}^{1/2} \tag{3.22}$$

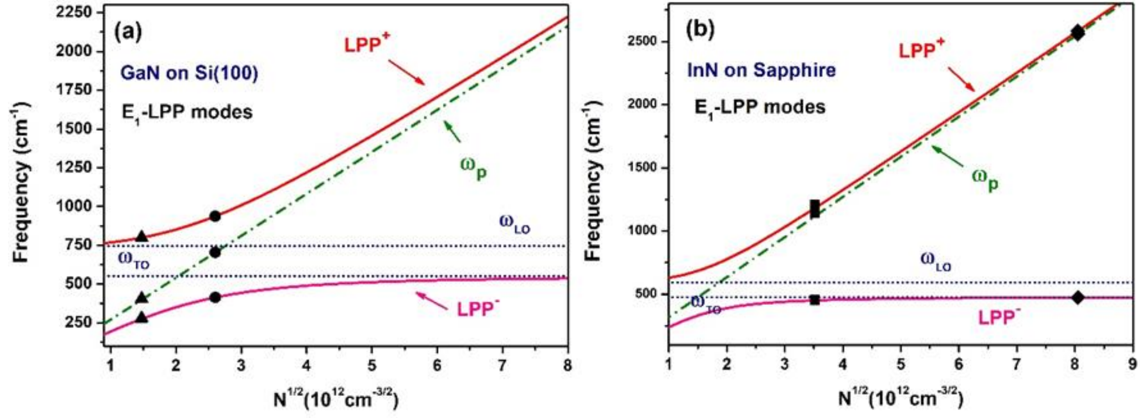

Figure 3.6. A comparison of theoretically predicted using Eq. 3.22 and experimentally derived E_1-LPP modes behavior of (a) GaN on Si(100) and (b) InN on sapphire grown by HC-PAALD.

The E_1-LPP mode behavior of GaN and InN thin films obtained experimentally and theoretically (Eq. 3.22) is shown in figure 3.6 as a function of free carrier concentration. Theoretically and experimentally behavior of E_1-LPP$^+$ and E_1-LPP$^-$ represented by solid lines and solid dots, respectively. Dashed lines show ω_{TO} and ω_{LO} whereas dotted line shows ω_p variation. When the free carrier concentration approaches zero, LPP$^-$ mode reaches zero and LPP$^+$ mode reaches ω_{LO} that shows ω_{LO} phononlike behavior at low doping. The LPP$^+$ and LPP$^-$ mode approach ω_p and ω_{TO}, respectively with the free carrier concentration increasing. Therefore, for higher doping concentrations, the LPP$^+$ mode shows plasmonlike behavior.

In multiple polar phonon mode materials, anharmonic coupling effects between LO phonons and plasmon excitations can be transformed into a factorized expression suggested by Kukharskii [98] (k species of free charge carriers).

$$\varepsilon_j^{L+FC}(\omega) = \varepsilon_{\infty,j} \frac{\prod_{i=1}^{k+1}\left(\omega^2 + i\tilde{\gamma}_{LO,ij}\omega - \tilde{\omega}_{LO,ij}^2\right)}{\omega^k \prod_{s=1}^{k}\left(\omega + i\gamma_{p,sj}\right)\prod_{i=1}^{l}\left(\omega^2 + i\gamma_{LO,ij}\omega - \omega_{LO,ij}^2\right)} \tag{3.23}$$

where and $\tilde{\gamma}_{LO,ij}, \tilde{\omega}_{LO,ij}$ and $\gamma_{p,sj}$ are the broadening values, the eigenfrequencies and plasmon broadening parameters of the *(k + l)* LPP modes, respectively.

3.2.4. Low-Polarity Mode Contributions

As mentioned above, structural defects such as impurities, defects *etc*. create additional infrared active modes. These IR-active modes ($\nu = 1,...,n$) cannot be represented by equation 3.22 because the phonon bands are greater than one ($l > 1$). Impurity modes (IM) with low polarity and small LO-TO splitting values ($\delta\omega_\nu^2 = \omega_{LO,\nu}^2 - \omega_{TO,\nu}^2$) contribute a small perturbation to the dielectric function and can be represented by Eq.3.24 [99].

$$\varepsilon_j^{L+FC+IM}(\omega) = \varepsilon_j^{L+FC}(\omega)\prod_{\nu=1}^{n}\left(1 + \frac{i\delta\gamma_{\nu,j}\omega - \delta\omega_{\nu,j}^2}{\omega^2 + i\gamma_{IM,\nu j}\omega - \omega_{IM,\nu j}^2}\right) \tag{3.24}$$

where $\omega_{IM,\nu}$, $\delta\gamma_{\nu,j}$ are IM modes frequency and broadening parameter $\left(\delta\gamma_\nu \equiv \gamma_{LO,\nu} - \gamma_{LO,\nu}\right)$, respectively.

3.3. Raman lineshape analysis

The induced polarization resulting from the interaction with the light is the elastic and inelastic scattering process. Raman scattering consists of the terms *Stoke* in which the atom or the molecule absorbs energy and the scattering radiation shifts to the lower frequency side and *anti-Stoke* scattering in which the atom or the molecule loses the energy and the scattering light shifts to the higher frequency side [100, 101]. In Raman scattering, which requires a change in polarizability, Raman transition from one state to another is only permitted when the molecular polarizability of these states is different. These Raman selection rules are very essential for determining allowed Raman modes and crystal symmetry. The allowed Raman modes with the Porto notation C(B, A)D (where C and D represent the incident and scattered light directions and B,A represent

their polarizations) for the group III-nitrides (wurtzite structure) are given in Table 3.1 [101]. For group III-nitrides thin films, the z(x, y)z and z(x, x)z configurations are easily observable if they generally grown along the [0001] direction of the substrate [101].

Table 3.1. Raman configurations of allowed in hexagonal nitrides

Configuration	*Mode*
$z(x,x)\bar{z}$	$A_1(TO), E_2^L, E_2^H$
$z(x,y)\bar{z}$	E_2^L, E_2^H
$x(z,z)\bar{x}$	$A_1(LO)$
$x(y,y)\bar{x}$	$A_1(TO), E_2^L, E_2^H$
$x(z,y)y$	$E_1(TO), E_1(LO)$
$x(y,z)\bar{x}$	$E_1(TO), E_1(LO)$

Information on the stress and crystalline quality of thin films can be extracted from the E_2^H phonon frequency and linewidth. The line shape of E_2^H phonon from Raman spectra was modelled using the following equation

$$I(\omega) \propto \int_0^1 \exp(-q^2L^2/4)\frac{d^3q}{\left[\omega-\omega(q)\right]^2+\left(\Gamma_0/2\right)^2} \tag{3.25}$$

where q is expressed in units of $\frac{2\pi}{a}$, a is the lattice constant, L is the correlation length.[102] The dispersion $\omega(q)$ for optical phonons is

$$\omega^2(q) = A - Bq^2 \tag{3.26}$$

where A and B are adjustable parameters.

The line shape analysis of A_1(LO) phonon mode leads to the determination of the free carrier concentration in the III-Nitrides. When doped with impurities, free carriers interact with the A_1(LO) optical phonons, but not with the non-polar E_2^H phonons [103]. The

mechanism of Raman scattering by LO phonon-plasmon coupled modes in GaN dominated by the deformation-potential and electro-optical scattering mechanism [102, 103]. A set of equations have been developed to determine the free carrier concentration in wide bandgap semiconductors [102]. The Raman intensity of A_1(LO) phonon mode is expressed by [102],

$$I_A = \frac{d^2S}{d\omega d\Omega} = \frac{16\pi\hbar n_2}{V_0^2 n_1}\frac{\omega_2^4}{C^4}\left(\frac{d\alpha}{dE}\right)^2 \left(n_\omega + 1\right) A\,\mathrm{Im}(-1/\varepsilon) \tag{3.27}$$

$$\begin{aligned} A = {} & 1 + 2C\omega_{TO}^2\left[\omega_p^2\gamma\left(\omega_{TO}^2 - \omega^2\right) - \omega^2\hbar\left(\omega^2 + \gamma^2 - \omega_p^2\right)\right]\Big/\Delta \\ & + C^2\left[\omega_{TO}^4\Big/\Delta\left(\omega_{LO}^2 - \omega_{TO}^2\right)\right]\left\{\omega_p^2\left[\gamma\left(\omega_{LO}^2 - \omega_{TO}^2\right) + \hbar\left(\omega_p^2 - 2\omega^2\right)\right] + \omega^2\hbar\left(\omega^2 + \gamma^2\right)\right\} \end{aligned} \tag{3.28}$$

$$\Delta = \omega_p^2\gamma\left[\left(\omega_T^2 - \omega^2\right)^2 + \left(\omega\hbar\right)^2\right] + \omega^2\hbar\left(\omega_L^2 - \omega_T^2\right)\left(\omega^2 + \gamma^2\right) \tag{3.29}$$

where V_0 is the volume of the unit cell, $n_{1,2}$ are the refractive indexes at the incident and scattered photon frequencies $\omega_{1,2}$,respectively; C is the Faust-Henry coefficient, α is the polarizability, E is macroscopic electrical field, n_ω is the Bose-Einstein factor, ω_{TO} and ω_{LO} are the TO and LO phonon frequencies, respectively. γ is the plasmon damping constant, ε is the dielectric function and η is the photon damping constant.

3.4. Transfer Matrix Method

The transfer matrix method is used to calculate the total transmittance and reflection at multiple planar, isotropic interfaces using *'Fresnel coefficient'.* Fresnel coefficient describe the reflection and transmission of light and derived from Maxwell's equations for the plane interface between different optical media [104].

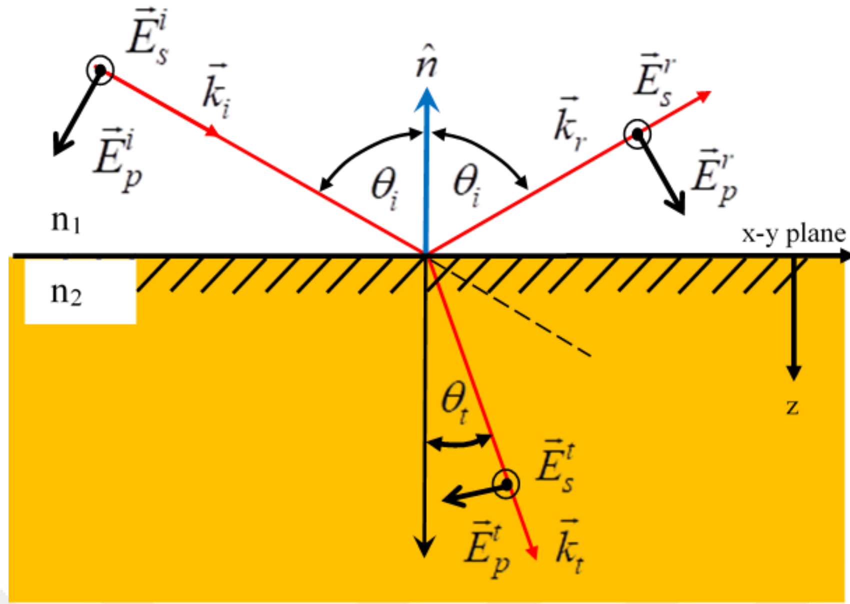

Figure 3.7. Coordinate system for measuring the *E* vectors of a plane wave reflected and refracted at a boundary between a medium of refractive index n_1 and a medium of refractive index n_2 [104].

Figure 3.8. shows coordinate system for medium of refractive index n_1 and a medium of refractive index n_2. The positive direction for the coordinates of the electric field vectors components indexed by s (s-polarized) is out of the paper, and that for the coordinates of the electric field vectors components indexed by p (p-polarized) is in the plane of the paper, as indicated by the arrows [105]. The wave vector ***k***, the direction the wave is traveling z, and angles of incidence and refraction θ_i and θ_t are also shown. The resulting Fresnel's coefficients for p-/s-polarized light with $\mu_1 = \mu_2 = 1$ (nonmagnetic material) for this system are described by Eq.30-33.

$$r_s \equiv \frac{E_s^r}{E_s^i} = \frac{n_1 \cos\theta_i - n_2 \cos\theta_t}{n_1 \cos\theta_i + n_2 \cos\theta_t} \tag{3.30}$$

$$t_s \equiv \frac{E_s^t}{E_s^i} = \frac{2n_1 \cos\theta_i}{n_1 \cos\theta_i + n_2 \cos\theta_t} \tag{3.31}$$

$$r_p \equiv \frac{E_p^r}{E_p^i} = \frac{n_2 \cos\theta_i - n_1 \cos\theta_t}{n_2 \cos\theta_i + n_1 \cos\theta_t} \tag{3.32}$$

$$t_p \equiv \frac{E_p^t}{E_p^i} = \frac{2n_1 \cos\theta_i}{n_2 \cos\theta_i + n_1 \cos\theta_t} \tag{3.33}$$

Figure 3.8 shows isotropic and homogeneous N-layer system. The arrows indicate the direction of travel of the electric fields. The electric field amplitudes (E) + and - symbols are the incident and reflected electric field amplitudes. All subscripts in the figure represent the optical media.

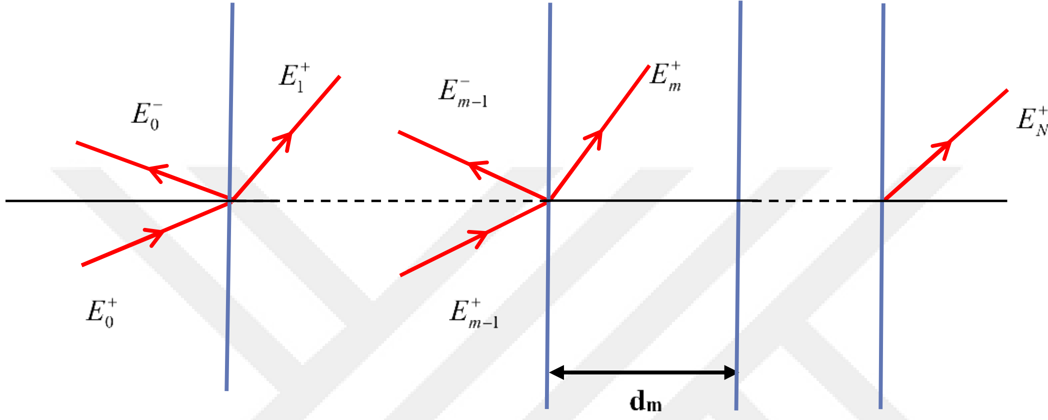

Figure 3.8. The path of the electromagnetic wave in a multi-layered structure

The matrix which gives the transmission and reflection coefficients of the electric field between these two mediums coming from the adjacent parallel m layer (m + 1) layer and connects the electric field amplitudes is called interface matrix. This matrix $M_{m,m+1}$ defined by the equation below.

$$\begin{pmatrix} E_{m+1}^+ \\ E_{m+1}^- \end{pmatrix} = \frac{1}{t_{m,m+1}} \begin{pmatrix} 1 & r_{m,m+1} \\ r_{m,m+1} & 1 \end{pmatrix} \begin{pmatrix} E_m^+ \\ E_m^- \end{pmatrix} = M_{m,m+1} \begin{pmatrix} E_m^+ \\ E_m^- \end{pmatrix} \tag{3.34}$$

The progression matrix that defines the wave propagation in the layer *m* with a thickness d_m is determined by Eq. 3.35

$$M_m = \begin{pmatrix} \exp(i\frac{2\pi}{\lambda}\tilde{n}_m d_m) & 0 \\ 0 & \exp(-i\frac{2\pi}{\lambda}\tilde{n}_m d_m) \end{pmatrix} \tag{3.35}$$

where, λ is the wavelength of the incident beam. The interface and propagation matrices obtained for layer *m* and *(m + 1)* can be applied to all consecutive layers within the structure. By multiplying the matrices obtained for all layers in the appropriate order, a result matrix (M_s) of 2x2 size is obtained for the whole structure. With this matrix, the electric field amplitudes in the last layer can be expressed in terms of the electric field amplitudes incident to the first layer. The matrix elements of the *Ms* matrix depend on the complex refractive index values of optical media and the thickness of the layers. Thus, the reflection and transmission coefficients for the whole structure can be easily found with the matrix elements of the result matrix. In addition, there is no need to obtain the electric field amplitudes of each layer by this method. Eq.3.36 shows the result matrix obtained by the transfer matrix method for an N-layer structure.

$$\begin{pmatrix} E_N^+ \\ E_N^- \end{pmatrix} = \prod_{m=0}^{N-1} \left(M_m M_{m,m+1} \right) \begin{pmatrix} E_0^+ \\ E_0^- \end{pmatrix} = M_s \begin{pmatrix} E_0^+ \\ E_0^- \end{pmatrix} = \begin{pmatrix} M_{11} & M_{12} \\ M_{21} & M_{22} \end{pmatrix} \begin{pmatrix} E_0^+ \\ E_0^- \end{pmatrix} \quad (3.36)$$

The reflection coefficient *rr* is the ratio of the reflected wave's complex electric field amplitude to that of the incident wave (Eq. (3.37)). The transmission coefficient *tt* is the ratio of the transmitted wave's electric field amplitude to that of incident wave (Eq. (3.38)).

$$tt = \left(\frac{E_N^+}{E_0^+} \right)_{E_N^- = 0} = \frac{\det(M_s)}{M_{2,2}} \quad (3.37)$$

$$rr = \left(\frac{E_0^-}{E_0^+} \right)_{E_N^- = 0} = \frac{M_{2,1}}{M_{2,2}} \quad (3.38)$$

The wavelength-dependent transmission and reflection values are obtained by squaring the absolute values of the coefficient values defined by Equations 3.39 and 3.40.

$$T = tt * tt^* = \left| \frac{\det(M)}{M_{2,2}} \right|^2 \quad (3.39)$$

$$R = rr * rr^* = \left| \frac{M_{2,1}}{M_{2,2}} \right|^2 \quad (3.40)$$

3.5. Spectroscopic Ellipsometry

Spectroscopic ellipsometer (SE) is a non-destructive, noncontact and noninvasive optical measurement technique that uses polarized light to characterize thin films, surfaces, and material microstructure. As shown in Figure 3.9, the monochromatic and linear polarized light wave interacts with the film at a desired angle. After reflection, the radiation passes a compensator and a second polarizer, which is called an analyzer and falls into the detector [106]. The detector analyzes the output elliptical polarization state after linearly polarized light is reflected obliquely off of a thin film sample. The polarization change of this reflected light is determined and information is obtained on the refractive index, dielectric function, and thickness of the film [74, 107].

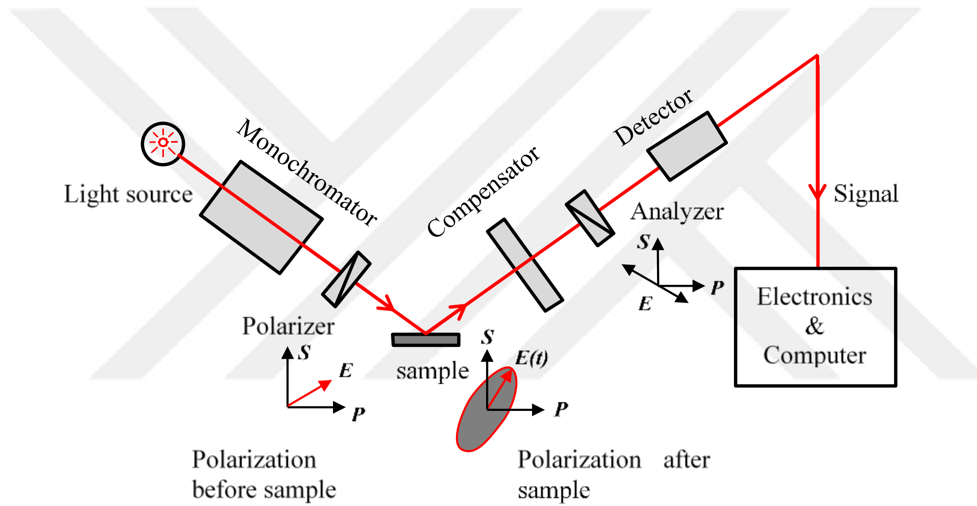

Figure 3.9. Schematic diagram of an ellipsometer

Ellipsometry measures the complex reflectance ratio ρ of a system (Eq.3.41), which may be parametrized by the amplitude component ψ and the phase difference Δ. These values are related to the ratio of Fresnel reflection coefficients r_p and r_s for p- and s-polarized light, respectively. The angle of incidence is chosen close to the Brewster angle of the sample to ensure a maximal difference in r_p and r_s [108].

$$\rho = \frac{r_p}{r_s} = Tan\psi . e^{i\Delta} = f(n_i, k_i, d_i ...) \tag{3.41}$$

3.6. Infrared Ellipsometry

Infrared spectroscopic ellipsometry (IRSE) is an infrared characterization method based on the determination of polarization change of the reflected light from the sample. The IRSE system is used to characterize the optical constants (n and k, dielectric functions), film thickness, material compositions (alloy fraction), molecular vibrations, phonon absorptions (crystalline materials), surface and interface layers, doping concentration (resistivity), and free carrier absorption of bulk and thin films in near and far infrared (1.7 to 30 microns) region [109]. The IRSE system used in this thesis integrates a Fourier Transform Infrared (FTIR) interferometer (based on Michelson interferometer) with a rotating compensator that modulates each wavelength at a different frequency and then gives the desired spectrum by Fourier transform of the detected intensity spectrum [110]. This rotating compensator allows to measure depolarization which is caused incomplete film coverage, variations in film thickness, bandwidth effects, and other factors [109]. As shown in Fig. 3.10 the light leaving the FTIR interferometer enters the ellipsometer and successively passes the wide-grid polarizer, sample, rotating compensator, analyzer and finally hits the DTSG (Deuterium triglycine sulfate) detector [110].

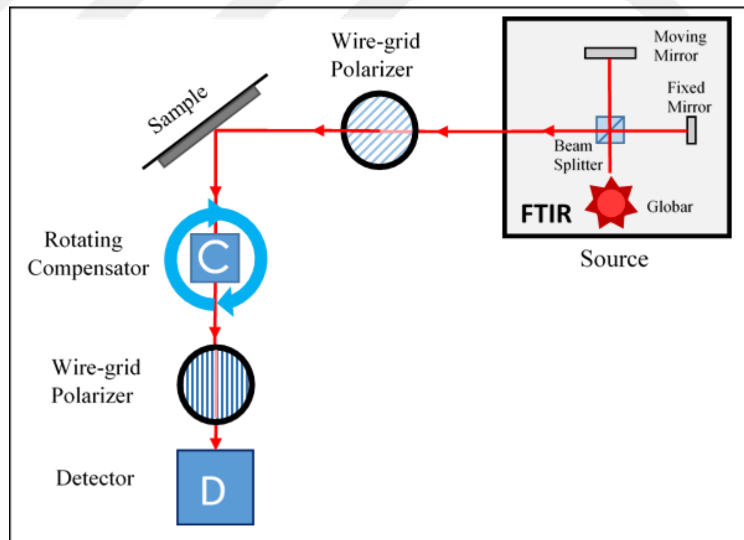

Figure 3.10. Schematic diagram of an IR-ellipsometer [109]

In this thesis, we found that there are two issues that should be considered and affect the measurement parameters during acquisition of IRSE data. The first issue is *backside reflection* and the second issue is *IR-beam size*. If back surface is not roughened quite

enough, reflected light beam from the back surface reach the detector aperture. By using sandpaper (or sandblasting, Dremel tools), the substrate surface is successfully roughened and reflected light beam can be effectively off the detector aperture [111].

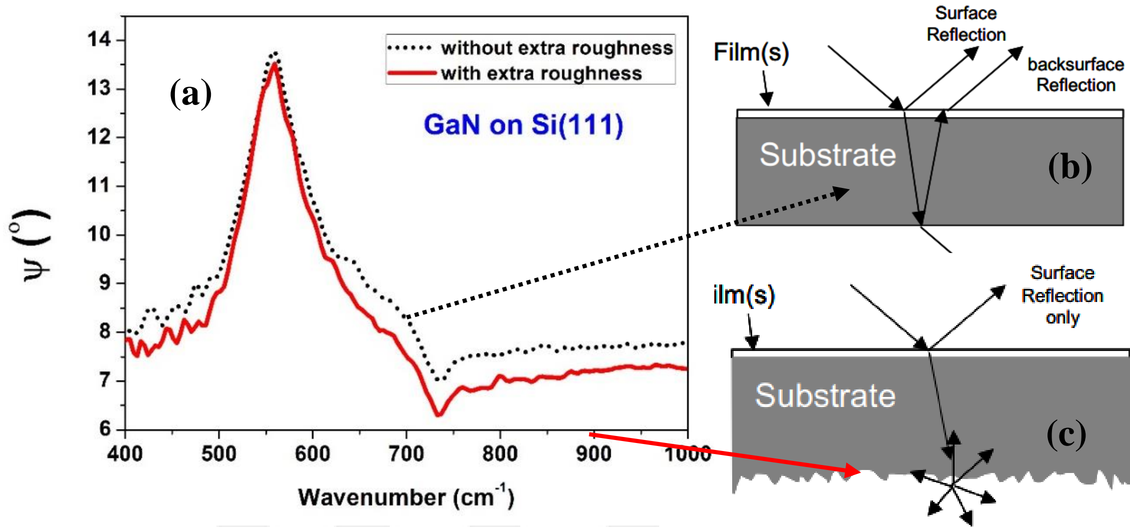

Figure 3.11. (a) Influence of backside reflection on ellipsometric Ψ data of GaN grown on double-side polished Si(111) and schematic representation of (b) reflection from the backside of the substrate [112] (c) roughened Si substrate on the backside [112].

Figure 3.11 shows that influence of the backside reflection on GaN grown on double-side polished Si(111). Ψ spectra obtained from silicon with and without additional backside roughness are indicated by solid and dotted line, respectively. Since silicon wafer used this work is 0.5 mm thick (typically 0.2 to 1 mm thick), light reflected from the front surface mixes in a partial manner with light reflected from the back surface (as shown in Fig.3.11 (b)). As can be seen from the figure, there is a slight difference between the intensities of the two Ψ spectra depending on the wavenumber, partially coherent mixing may not be observed directly. Using the normal incidence relative transmitted intensity, it can be found whether the film needs extra roughness [112].

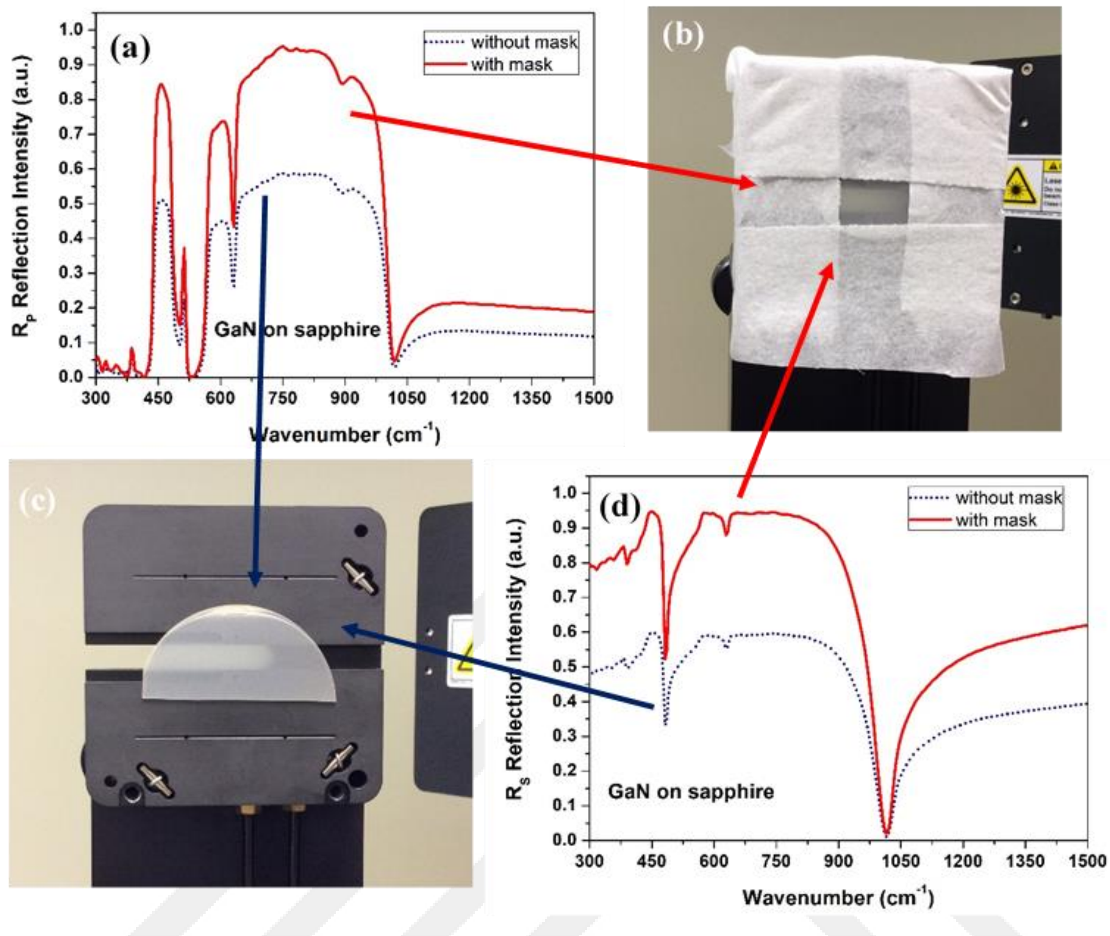

Figure 3.12. Influence of IR beam size on (a) p-polarized (R_p) and (d) s-polarized (R_s) reflection data of GaN on sapphire at 80 degrees, IRSE sample stage (b) with mask and (c) without mask

Another problem that strongly influences ellipsometric data is IR-beam size. Especially when taking measurements at high-angles, the spot size becomes quite large and IR beam cover extra areas beside the film surface. For this purpose, we use tissue paper that act as a scattering media in order to cover the external area around the substrate [112]. Figure 3.12 shows instrument sample stage and the R_s and R_p IR-reflection data of GaN obtained with and without mask. As seen from the data, the IR measurement taken without masked film exhibit a reduced intensity about 50%. The angle-dependent spot size change is described in detail in ref 112.

3.7. X-ray Diffraction

X-ray diffraction (XRD) is a powerful method to analyze all kind matter without damaging the matter. An x-ray diffraction pattern; orientation of the single crystal or particle, crystal structure of an unknown material, particle size, stress and shape can be obtained.

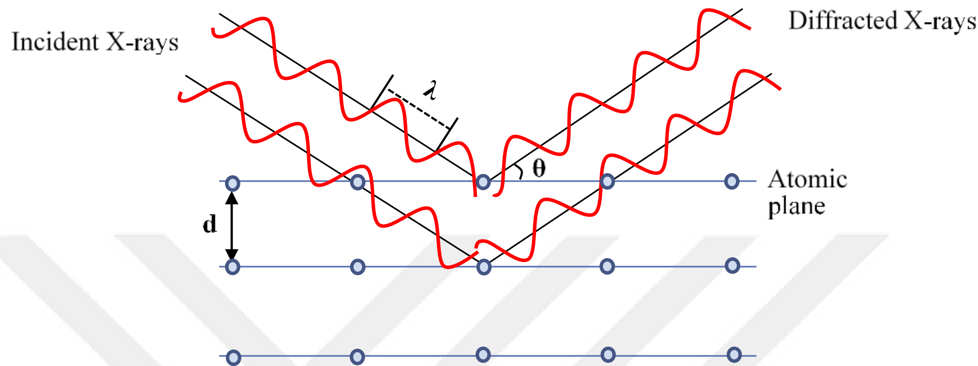

Figure 3.13. Schematic representation of X-ray diffraction

The principle of this technique is the interaction of x-rays with atomic planes in the thin film. The schematic representation of this interaction is shown in Fig. 3.13. The diffraction of X-rays in crystalline materials is simply defined by Bragg's law [113]. Because of the periodic arrangement of atoms on the crystallographic plane, they are reflected by constructive interference from the crystal surfaces they strike at certain angles.

$$n\lambda = 2d\sin\theta \tag{3.42}$$

where n is any integer, λ is wavelength of the x-ray, d is the distance between diffracting planes and θ is incident angel (Bragg angle). In addition, scanning at low incident angle, popularly known as grazing incidence XRD (GIXRD), allows XRD measurements of very thin films. Thus, a stronger signal is obtained from the film itself to obtain information about the crystal structure.

3.8. X-ray Photoelectron Spectroscopy

X-ray photoelectron spectroscopy (XPS) which provides detailed information in the high-energy regime is a widely used quantitative spectroscopic technique to analyze the surface

chemistry of a material. The empirical formula, element composition, electronic state, and chemical state of the elements in the film and to which they are bonded can be easily measured because XPS is often used to study core level study [114].

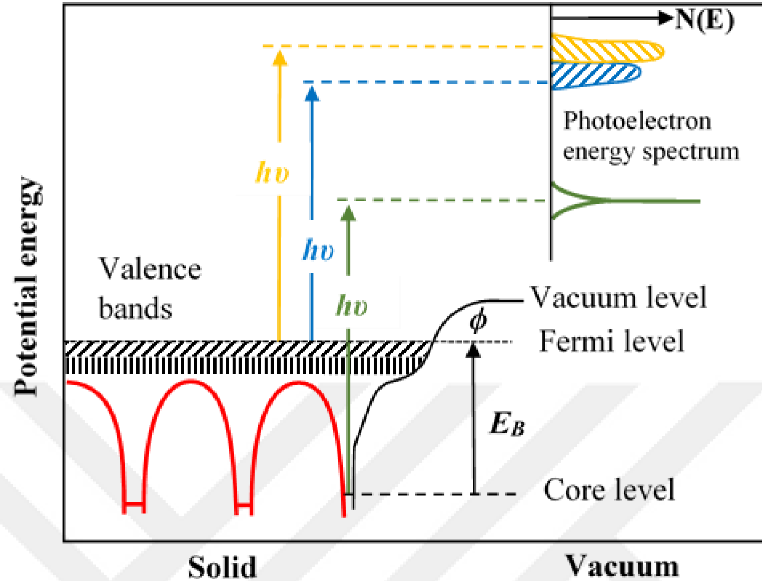

Figure 3.14. An illustration energy-level diagram of photoemission from the core and valence bands level in a solid [69].

The electrons in the semiconductor can be ejected by high-energy photons by irradiating the sample surface. Moreover, electron energy analyzer and synchrotron radiation which allows measurements to be taken over a wide spectral region are part of the XPS system under ultra-high vacuum regime [69, 115]. As shown in figure 3.14, the kinetic energies of the excited electrons are measured and analyzed to obtain the photoelectron spectrum in order to obtain the initial electron state's information. The binding energy of the emitted electron ($E_{binding}$) from valance and core level depends upon photon energy (E_{photon}), kinetic energy ($E_{kinetic}$) and the work function ϕ which is easily measured or known and is represented by Eq. 3.43 (photoelectric effect).

$$E_{binding} = E_{photon} - \left(E_{kinetic} + \phi\right) \tag{3.43}$$

In the photoelectron spectra formed by the change of kinetic energy with the binding energy, peaks are seen at certain binding energies. By analyzing these photoelectron

peaks, it can be obtained from which element and orbital the electron is emitted/ejected on both the surface and the bulk of the material.

3.9. Atomic Force Microscopy

Atomic force microscopy (AFM) is a high resolution scanning probe microscope (SPM) type that provides information on surface morphology and surface roughness of thin films. AFM is based on high sensitivity determination of interatomic forces between single atoms [116] as shown in Figure 3.15.

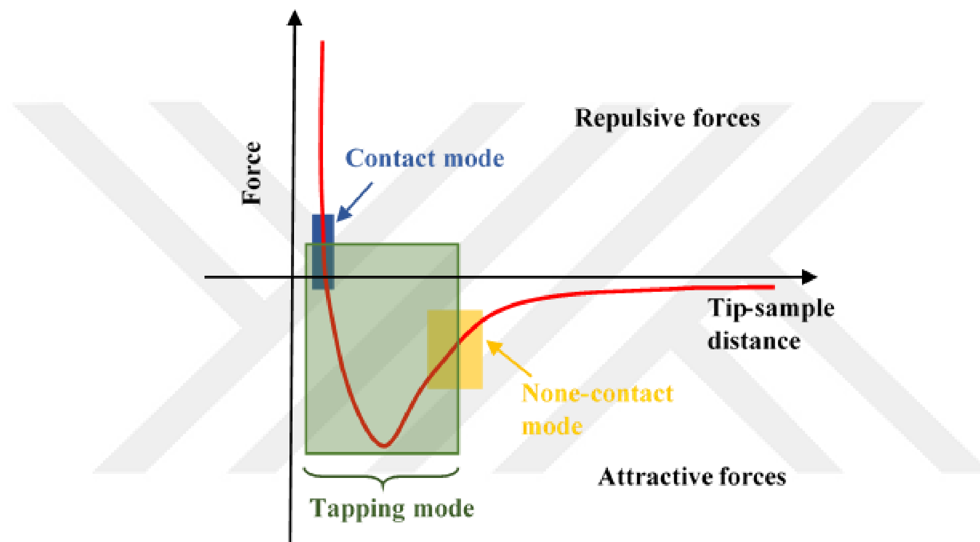

Figure 3.15. The typical force-distance curve and different regimes and modes of the tip-surface interaction in an AFM [100].

In AFM, the force (van der Waals force, electrical, magnetic, capillary, thermal, etc.) between the sharp tip at cantilever end and the surface is determined using Hook's law. Depending on the movement of the tip, there are three scanning modes. In the contact mode tip contacts surface in the short-range repulsive region. In the non-contact mode, the tip does not contact the surface but instead oscillates at or slightly above the resonance frequency in the long-range attractive region. In the tapping mode, the tip approaches the surface sufficiently in the region where the short-distance force is effective (between contact and non-contact modes) [100, 101].

In general, a semiconductor laser diode beam is focused on the back of the cantilever to determine the bending of the cantilever in the AFM. The laser beam reflected from the cantilever is collected by a position-sensitive detector (PSD) consisting of two

photodiodes close to each other during surface scanning. Moreover, Piezoelectric elements on the cantilever provide precise scanning [116].

4. PROPERTIES OF GaN GROWN BY HCPA-ALD

The work described in this chapter published as:

(1) ***"The role of film thickness on the structural and optical properties of GaN on Si (100) grown by hollow-cathode plasma-assisted atomic layer deposition."*** Neşe Güngör, Mustafa Alevli. Journal of Vacuum Science & Technology A: Vacuum, Surfaces, and Films, 36(2) (2018)

(2) ***"Visible/Infrared refractive index and phonon properties of GaN films grown on sapphire by hollow-cathode plasma-assisted atomic layer deposition."*** Neşe Güngör, Mustafa Alevli. Journal of Vacuum Science & Technology A: Vacuum, Surfaces, and Films, 37(5) (2019)

4.1. The Role of Film Thickness on The Structural and Optical Properties of GaN on Si (100)

4.1.1. Introduction

Gallium nitride is a direct wide band gap compound semiconductor (3.4 eV at room temperature) which is the key material for the fabrication of efficient lasers, detectors, high-power amplifiers and light emitting diodes (LEDs) [117, 118]. High quality GaN thin films are grown by metalorganic chemical vapor deposition and molecular beam epitaxy [119]. However, the deposition of the high quality crystalline GaN films requires high temperature deposition techniques, such as MOCVD, MBE, and hydride vapor phase epitaxy (HVPE) [1]. This situation hinders GaN deposition on many thermally sensitive substrates and device structures. It is difficult to grow bulk crystals of GaN due to the high dissociation pressure of nitrogen at the growth temperature [120]. Therefore, hetero-epitaxial growth on a foreign substrate such as sapphire and silicon carbide (SiC) is usually employed for the deposition of crystalline GaN for most applications [121]. On the other hand, high substrate temperatures can cause biaxial stress within GaN films, nitrogen loss, and GaN decomposition, which lead to the loss in the efficiency of GaN-based devices [122]. The biaxial stress occurs owing to the difference between thermal expansion coefficient of GaN layer and substrates, resulting in poor GaN based device performance [117]. In order to reduce thermal stress in GaN films, lithium Gallate ($LiGaO_2$), lithium aluminate ($LiAlO_2$), and SiC were preferred as lattice-matching

substrates [122]. However, these substrates are too expensive to be commercialized. Therefore, alternative low temperature deposition techniques is highly desired for the deposition of GaN films and related alloys.

The atomic layer deposition technique enables the deposition of GaN films at low temperatures as low as 200 °C [10, 123]. The deposition of III-Nitride films using N_2/H_2 or NH_3 at low temperature as low as 200°C requires an external energy source in order to enhance the reactivity of N-containing precursors, such as plasma. In order to decrease substrate temperature, plasma enhanced atomic layer deposition of GaN was first demonstrated using tri-methyl gallium (TMG) and ammonia (NH_3), resulting in self-limiting growth mechanism character within 185-385 °C [7]. Following that, Ozgit-Akgun *et.al.* demonstrated HCPA-ALD of GaN which is also used in this study as well in order to reduce the oxygen contamination [123]. PEALD technique is able to deposit thin films conformally due to its unique “self-limiting” growth mechanism. When compared with alternative low temperature physical vapor deposition techniques, PA-ALD stands out in terms of large area uniformity, ultimate conformality, and submonolayer precision thickness control.

In our previous studies, we reported on the polycrystalline GaN thin films deposition on Si and sapphire subtrates using TMG and TEG as gallium precursor in conjunction with NH_3 or N_2/H_2 plasma reactant as nitrogen precursor [7, 10, 58, 123]. In this study, we have studied the crystallinity, chemical composition, surface morphology and optical properties of highly oriented (002) GaN films with different thicknesses, ranging from 5.37 to 81.40 nm deposited on Si substrates via low-temperature HCPA-ALD. GaN crystal quality generally improves with increasing layer thickness for film deposited at high temperatures [120, 124] whereas we observed that GaN films with thicknesses above 48.65 nm have different behavior compared to the thinner GaN films.

4.1.2. Experimental

GaN thin films were grown on Si(100) substrate using a modified Fiji F200-LL ALD reactor (Ultratech/CambridgeNanotech, Inc., Cambridge, MA) in which quartz-based inductively coupled RF-plasma source was replaced with a stainless steel hollow-cathode plasma source (Meaglow Ltd., Canada). Prior to depositions, Si (100) substrates were

cleaned sequentially using isopropanol, acetone, methanol, and deionized (DI) water in an ultrasonic bath. In order to remove native oxide on the substrate surface, Si substrates were dipped into diluted hydrofluoric acid solution (2 %) for ~2 min, followed by rinsing with DI water and drying with N_2. Substrates were immediately loaded into the ALD reactor and kept at the deposition temperature for at least 20 min before the deposition process was started.

GaN thin films were deposited using optimized process parameters [58]. Prior to GaN deposition, the substrates were exposed to the N_2/H_2 plasma (60s) and afterwards 60 s of N_2 plasma at 200 °C in order to form a SiN_x monolayer. This nitridation step provides additional strain relaxation paths, and enhances the crystalline quality of the deposited thin film layer [125]. For the purpose of comparison, GaN films were grown with identical parameters. TEG and N_2/H_2 plasma precursors were used as gallium (Ga) and nitrogen (N) precursors, respectively. Ga and N precursors were adjusted in order to achieve the self-limiting growth scheme, which is an evidence of ideal atomic layer deposition [123]. Each ALD cycle consisted of four steps: (1)TEG pulse for 0.5 s, (2) 10 s Ar purge, (3) 300 W N_2/H_2 plasma for 60 s (50 sccm each), and finally (4) 10 s Ar purge. GaN layers were deposited at 200 °C with 130, 500, 1500 and 2500 deposition cycles.

Crystalline phases of the GaN films were identified using a PANAnalytical X'Pert PRO MRD diffractometer in θ-2θ mode with Cu K_α radiation. GIXRD were performed in the range of 20°-75°. Incidence angle (ω) was 0.3 for GIXRD measurements in order to avoid intensive signal from substrate. GIXRD patterns were obtained by performing scans with a step size of 0.1°. In order to determine elemental compositions and chemical bonding states of the GaN films, XPS (Thermo Scientific) measurements were carried out using Al K_α radiation. The pass energy, step size, and spot size were 30 eV, 0.1 eV, and 400 µm, respectively. Peak deconvolution was performed using the AVANTAGE software, without applying any restrictions to spectral location and full width at half maximum values. Surface morphology was investigated by using AFM, (Park systems Corp., XE-100). The film thicknesses and optical constants of the samples were extracted from the measured SE (V-VASE, J.A. Woollam Co., Inc.) data in the wavelength range of 300–1000 nm at various incidence angles.

4.1.3. Structural characterization of GaN films

The epitaxial orientation, crystallization, lattice parameter and strain of HCPA-ALD grown GaN thin films with different thickness (i.e., 5.37, 21.01,48.65, and 81.40 nm) were obtained using GIXRD. Fig. 4.1 shows the GIXRD patterns of GaN films deposited at 200 °C with different thickness. All GaN films shows single-phase polycrystalline character with hexagonal wurtzite structure due to the existence of multiple GaN diffraction planes. The same reflection peaks are observed for all samples and are referred to the (002) and (200) planes of h-GaN. For the 5.37 nm GaN film, only the (103) diffraction peak is not evident. When the thickness is increased to 21.01 nm, the (002) and (103) diffraction peaks are clearly observed in the GIXRD patterns of GaN films. A prominent (002) peak indicates that the (002) is the preferred orientation with the increase in the thickness. For this reason, epitaxial growth of (002)-oriented GaN at 200 °C is feasible by improving the film thickness to a certain value around ~40 nm.

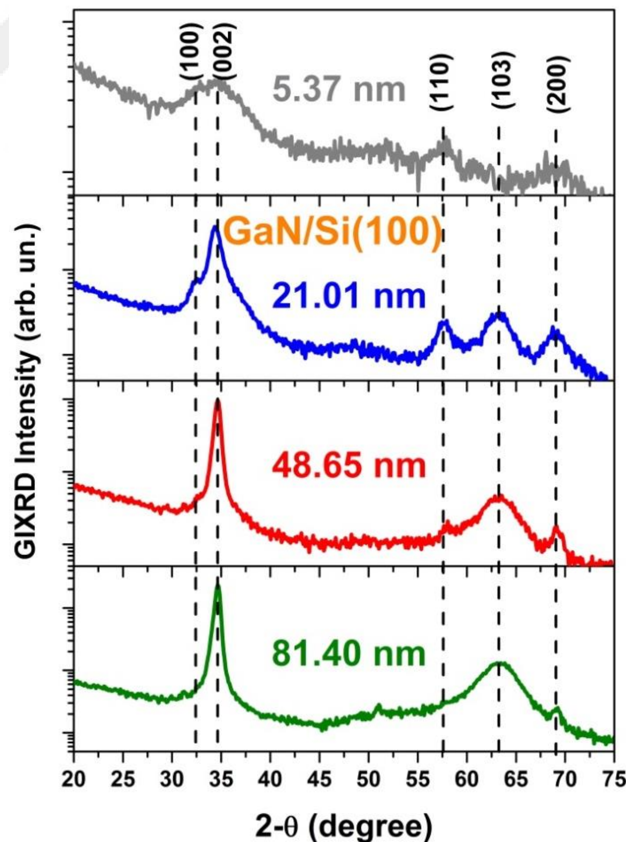

Figure 4.1. GIXRD patterns of GaN thin films with different thickness on Si(100) substrate.

Furthermore, no other phase or impurity related diffraction peak is observed in the GIXRD patterns of all films, confirming the synthesis of polycrystalline ~5 nm GaN film at 200°C with (002) preferential growth direction. It has been reported that the deposition of epitaxial GaN film with (002) orientation requires substrate temperatures higher than 600°C [126]. However our results indicate that epitaxial growth of GaN at a low temperature as low as 200°C is achievable.

The full width of at half-maximum (FWHM) of the (002) diffraction peak is decreased with increasing film thickness (4.44, 1.23, 0.63 and 0.56 for 5.37, 21.01, 48.65, and 81.40 nm, respectively), which indicates that GaN films with film thickness 48.65 nm and 81.40 nm exhibit better crystalline quality and lattice arrangement compared to thinner films [127]. However, the effect of film thickness on crystallinity is often interlinked to other factors, such as temperature and substrate [14]. But it is clear that the film thickness can directly affect the crystalline properties of the films as shown in our study. Furthermore, the size of the grain in the GaN films grown with different growth cycles were estimated from the FWHM of (002) diffraction peaks using Scherrer equation since FWHM of (002) is an indicator of crystal order [127]. This estimate yields values of average grain size 1.96, 7.07, 13.81 and 15.54 nm for the increasing film thickness from 5.37 nm to 81.40 nm. Film thickness had a marked effect on the grain size of the films and this size increases with film thickness. Our experimental observations on grain size and its dependence on film thickness are comparable with our AFM work for GaN films of thickness less than or equal to 48.65 nm. This issue is discussed later in this section.The lattice constants in *c*-axis and *a*-axis for each GaN film were calculated using Bragg's law from the (002) and (101) diffraction peak positions. The calculated lattice parameters are summarized in Table 4.1. These values are almost comparable to values reported for the unstrained GaN (a_0= 3.189 Å, c_0=5.185 Å) [128]. As the thickness is increased, the lattice constant *a* increases and *c* decreases. The difference in the lattice constant *c* and *a* of GaN films is correlated to the strain in the film. It is assumed that the strain in the GaN films is almost completely relaxed at thickness greater than 21.01 nm and less than 48.65 nm. The relaxation mechanism occurs for HPCA-ALD GaN film thicker than ~21.01 nm.

The strains of GaN films were calculated using the lattice constants of GaN films. The out-of-plane (ε_{zz}) and in-plane (ε_{xx}) strain tensor components were obtained from $\varepsilon_{zz}=(c_{epi}$-

$c_0)/c_0$ and $\varepsilon_{xx}=(a_{epi}-a_0)/a_0$, where c_{epi} , a_{epi} and c_0, a_0 are lattice constants for epilayer and bulk material, respectively [128]. The calculated strain components ε_{zz} and ε_{xx} are listed in Table I. For the films whose thickness is less than 48.65 nm, the GaN layer is found to be tensilely strained in out-of-plane directions. The negative values of out-of-plane (ε_{zz}) indicate that 48.65 and 81.40 nm thick GaN films are under compressive strain along c-axis. Furthermore, the estimated in-plane strain (ε_{xx}) in GaN films indicates tensile strain in 21.01, 48.65 and 81.40 nm thick films, while the compressive strain is dominant in 5.31 nm thick film.

Table 4.1. Lattice constants and elastic strain (in parallel (ε_{xx}) and perpendicular (ε_{zz}) directions) in the GaN layers. The negative values of calculated strain show the existence of compressive strain while the positive value denotes tensile strain.

Thickness (nm)	c_{epi} (Å)	a_{epi} (Å)	ε_{zz} (10^{-3})	ε_{zz} (10^{-3})
5.31	5.1951	3.1852	1.946	-1.1965
21.01	5.1907	3.1907	1.102	0.526
48.65	5.1769	3.195	-1.556	1.884
81.40	5.1766	3.1977	-1.625	2.720

The difference in in-plane and out-of-plane strain might be attributed to the increase in film thickness. Moreover, large thermal and lattice mismatches between the GaN film and the Si substrate also play significant roles in affecting strain [120, 127]. From the GIXRD studies, the increase in GaN lattice constant *a* with increasing film thickness point to a continuous variation in the tensile strain with further deposition.

4.1.4. Compositional analysis

Chemical compositions and bonding states of GaN films were studied using XPS. The survey scans from the surface of the films were charge-corrected by shifting all peaks to the adventitious C 1s spectral component binding energy at 284.8 eV. The survey scans

from the bulk of the films were charge corrected by shifting all peaks to the Ar 2p peak at 242 eV. The elemental compositions of the GaN films obtained from XPS survey scans of surface and bulk are presented in Table 4.2. It is evident that the surface of GaN films was contaminated with oxygen (up to 13.94 at. %) and carbon (up to 17.41 at. %) which arise from postdeposition atmospheric exposure. There was no evidence of carbon impurities in the bulk of the films which clearly shows effective removal of carbon ligands. On the other hand, the ratio of oxygen in the bulk of the films are around ~6-8 at.% for the thickness of 5.37 and 21.01 nm and ~3 at. % for the thickness of 48.65 and 81.40 nm. The amount of oxygen decreases with increasing thickness. The lower amount of oxygen, compared to the surface, shows that a significant portion of oxygen is the result of atmospheric oxidation [129].

Table 4.2. Elemental at. % of GaN grown on Si(100) as extracted from XPS survey scans.

	Surface elemental composition (at %)				Bulk elemental composition (at %)		
Thickness (nm)	Ga	N	O	C	Ga	N	O
5.37	22.75	46.02	13.94	17.29	26.58	64.86	7.81
21.01	25.14	46.50	12.93	15.43	30.75	63.09	6.16
48.65	25.72	45.40	11.46	17.41	30.96	65.02	3.25
81.40	25.45	46.78	13.43	14.34	31.01	65.41	3.59

Fig. 4.2 shows the Ga 3d and N 1s high resolution core level XPS (HR-XPS) scans from the bulk of the GaN films with different thickness. The HR-XPS scans of Ga 3d for GaN thin films were fitted by two subpeaks which are assigned to Ga–N and Ga–Ga bonds (Fig. 4.2 (a)). All the Ga 3d HR-XPS scans are dominated by Ga–N main peak which appears at 19.5 and 19.4 eV for 5.37 and 21.01 nm thick GaN films while it appears at 19.2 and 19.18 eV for 48.65 and 81.40 nm thick GaN films. These values are in agreement with previously reported values [10]. It is believed that the Ga–Ga bond is not associated

with the films, but forms during Ar ion etching due to the accumulation of metallic Ga on the surface of the GaN thin film samples [123].

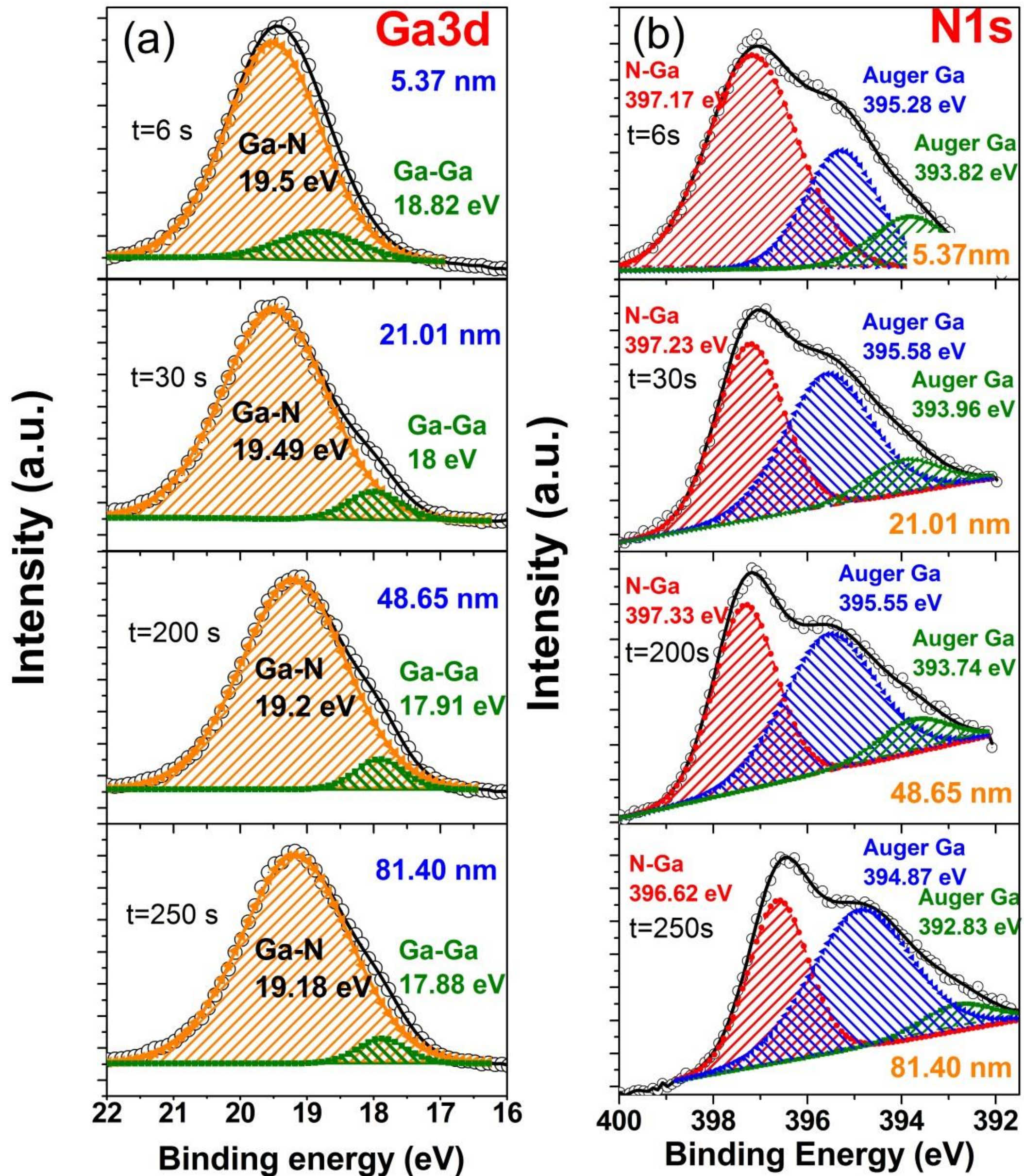

Figure 4.2. High resolution XPS scans of (a) Ga 3d and (b) N 1s for GaN films of different thickness on Si(100) at 200 °C.

N 1s HR-XPS scans for the GaN films were decomposed into three components which are assigned to N–Ga bond (397.23 eV) and Auger LMM Ga peaks (395.58 and 393.96 eV). Energy position values (Fig. 4.2(b)) for Ga-N bond are close to earlier reported values [130]. All the Ga LMM peaks for the 5.37 and 21.01 nm thick GaN films appear on the higher energy side as compared to 48.65 and 81.40 nm thick GaN films. In

summary, as the thickness of the film increases, the spectral locations of the Ga 3d binding energies (BEs) shifted from lower BE to the higher BE whereas the N 1s BEs shifted from higher BE to the lower BE energies except 81.40 nm thick GaN film. Ga 3d and N 1s core levels binding energies shift was observed to be 0.32 eV and 0.55 eV, respectively. This shift might be attributed to a change in band bending, which is a result of oxygen reduction in the GaN structure. This explanation agrees well with the atomic percentage of oxygen obtained from the XPS analysis.

Survey scans from the surface and bulk of GaN films of different thickness reveal nonstoichiometric films with higher atomic percentages for nitrogen (Table 4.2). In order to provide a more realistic stoichiometric ratio of Ga/N, we take into consideration that the atomic concentration of N and Ga are overestimated due to the significant contributions of Ga Auger peaks and minor contributions of Ga-Ga peak, respectively.

Table 4.3. Relative percentage of different bonding states in the Ga 3d core-level spectra (Fig. 4.2 (a)) and N 1s core level spectra (Fig. 4.2 (b)) of the grown GaN films.

		Bulk components effective composition (at %)			
Element	*Peak*	*5.37 nm*	*21.01 nm*	*48.65 nm*	*81.40 nm*
Ga 3d	Ga-N	23.79	28.69	29.01	29.43
	Ga-Ga	2.79	2.06	1.95	1.58
N 1s	N-Ga	39.52	28.93	28.43	25.01
	Ga LMM	17.43	28.18	30.90	4.77
	Ga LMM	7.91	5.99	5.70	35.62
Ga/N	Ga-N/N-Ga	1:1.66	1:1.01	1:0.98	1:0.85

Table 4.3 shows the relative percentage contribution of different chemical bonding states in the Ga 3d and N 1s core levels of the GaN films. Relative percentage contribution of fitting components is calculated using bulk elemental composition of Ga and N given in Table II and normalized area ratio of components of Ga 3d and N 1s HR-XPS scans. For instance; only 38.24% of the 65.41% N element ratio is composed of the N-Ga bond contribution, which corresponds to an effective nitrogen concentration of 39.52% for 81.40 nm film. Calculated Ga/N stoichiometry turned out to be 1:1.66, 1:1.01, 1:0.98 and 1:0.85 for 5.37, 21.01, 48.65, and 81.40 nm, respectively. It is seen that for 5.37 nm thick sample, the bulk layer is considerably N-rich, for GaN films with thicknesses > 21.01, the stoichiometric ratio is found to be close to the value of unity. The near-ideal stoichiometry implies the improvement of the crystallinity of the films. As the thickness increases from 21.01 to 81.40 nm, the Ga/N ratio changes from N rich to Ga rich.

4.1.5. Surface morphology analysis

The effect of thickness on the surface morphologies of GaN films is revealed by atomic force microscopy. AFM images are shown in Fig. 4.3. Root mean square (rms) surface roughness and grain size of GaN films were obtained using AFM measurements with scan area of 1x 1μm^2. Those values are summarized in Table 4.4.

Table 4.4. Grain size and RMS roughness values of GaN layers determined from AFM images.

Thickness (nm)	*RMS roughness (nm)*	*Grain size (nm)*
5.37	0.248	7.40
21.01	1.1	11.10
48.65	0.586	13.10
81.40	0.575	7

RMS surface roughness and grain size values were calculated using free AFM analysis software (Gwyddion). AFM images of GaN films clearly show how the granular structure

changes with the film thickness. When the film thickness increases, the islands started to coalesce and the roughness increases due to the growth of conical pyramids (Fig. 4.3b,c,d). The coalescence has started when the thickness is approximately ~20 nm. However, the topography of the sample surface of GaN films with thickness of 5.37 and 21.01 nm reveals a more uniform distribution of island heights throughout the growth area compared to GaN films with thickness of 48.65 and 81.40 nm. As the GaN film thickness increases from 5.37 to 48.65 nm, the surface of these three films is covered with dense grains and their grain size increases from 7. 40 nm to 13.10 nm.The grain density decreases with increasing grain size. These findings are found to be consistent with earlier reports [131]. These results show that smaller grains aggregate to form larger grains for GaN films with thickness less than or equal to 48.65 nm. It has been demonstrated that the RMS roughness and grain size increase with the film thickness for GaN films with thickness less than or equal to 48.65 nm, but decrease for 81.40 nm thick film. According to the AFM measurements one could conclude that the coalescence became dominant when the thickness is at 48.65 nm and the roughness decreases down to 0.586 nm due to the coalescence of grains.

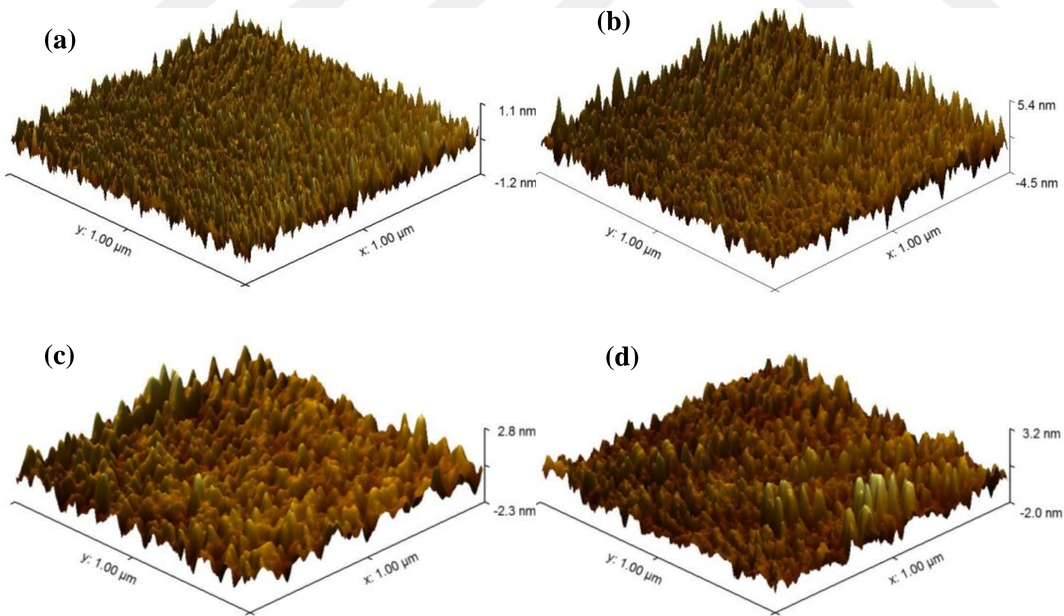

Figure 4.3. AFM images of GaN films with different thicknesses (a) 5.37 nm, (b) 21.01 nm, (c) 48.65 nm, and (d) 81.40 nm.

4.1.6. Optical properties

Optical properties of GaN films with different thickness, including refractive index dispersion curves and optical band gap, were determined using spectroscopic ellipsometry measurements. The experimental and fitted Ψ and Δ of GaN films with thickness 5.37 and 81.40 nm are shown in Fig. 4.4 (a) and (b) for angles of incidence 65°, 70° and 75°, respectively. A good agreement is obtained between the experimental data and fitting data with mean squared error (MSE) < 5 for all samples. It is critical to parameterize the unknown optical functions for fitting SE data. The ellipsometric data were interpreted in two independent steps assuming a five-phase model (ambient/roughened GaN/GaN/SiO_2/Si) for the accurate determination of the optical constants. In the first step, the unknown thickness and dielectric function of the GaN films were obtained. Thus, the dielectric functions for the transparent region (400 – 1000 nm) were obtained with the Cauchy model for bulk-like GaN and Bruggeman effective medium approximation (EMA) layer consisting of 50% of the GaN and 50% void for roughened GaN surface layer. Both the thickness of bulk-like GaN and surface roughness layer were determined by minimizing the MSE value for all measured spectra by varying Cauchy parameters and thickness of layers. The bottom layers Si and SiO_2 were modelled with the dielectric function given in the WVASE32 analysis program. The thicknesses of bulk-like GaN film were found to be 5.37±0.011 nm, 21.01±0.009 nm, 48.65±0.01 nm, and 81.4±0.014 nm whereas the thicknesses of surface roughness layer were found as 0.03±0.032 nm, 3.98±0.036 nm, 8.32±0.043 nm, and 12.10±0.045 nm for 130, 500, 1500 and 2500 growth cycles, respectively. From the fitted results, the film thickness increases linearly with increasing number of deposition cycles, as expected for well-behaved ALD process. In the second step, we have used modified model dielectric function (MDF) with adjustable broadening for hexagonal materials proposed by Adachi *et al.* [77, 132] and modified by Kim *et al.*[82] in order to model the dielectric function of GaN over wide spectral region (300-1000 nm). Furthermore; the obtained thicknesses of bulk-like GaN and surface roughness layers from the 1st step were used as input parameters in the 2nd step. The complex dielectric function in MDF (Eq. (4.1) given below) is described by the sum of the terms corresponding to band-to-band transition (ε_0 and ε_1) and excitonic contributions (ε_{0X} and ε_{1X}) at critical points E_0 and E_1 and the additive constant term (ε_∞)

[132, 133]. The modified-MDF reproduces accurately the experimental data especially around the fundamental absorption edge [83, 134].

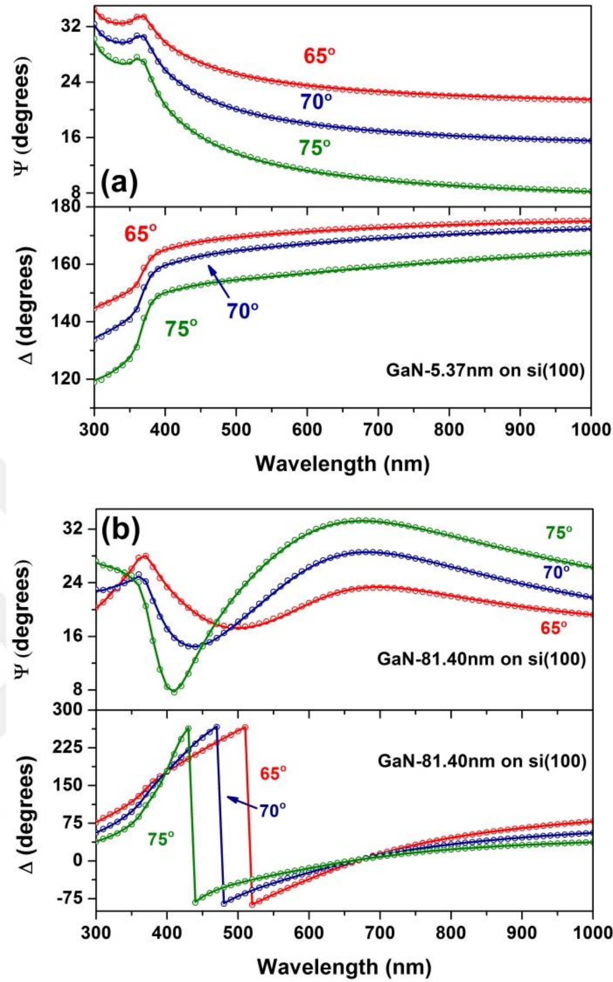

Figure 4.4. Ellipsometry spectra of (a) 5.37 nm and (b) 81.40 nm GaN films grown on Si(100) at room temperature (circle) compared with calculations (solid line).

$$\varepsilon_{GaN}(E) = \varepsilon_0(E) + \varepsilon_{0X}(E) + \varepsilon_1(E) + \varepsilon_{1X}(E) + \varepsilon_\infty \tag{4.1}$$

The refractive index n(λ) and extinction coefficient k(λ) of GaN films on Si(100) were determined using the spectroscopic ellipsometry measurements and plotted in Fig. 4.5(a) and (b) as a function of wavelength, respectively. The refractive index increases with film thickness up to 21.01 nm and is saturated gradually above this thickness. This thickness-dependence of the refractive index has been reported for GaN[126] and various semiconductors [135–138].

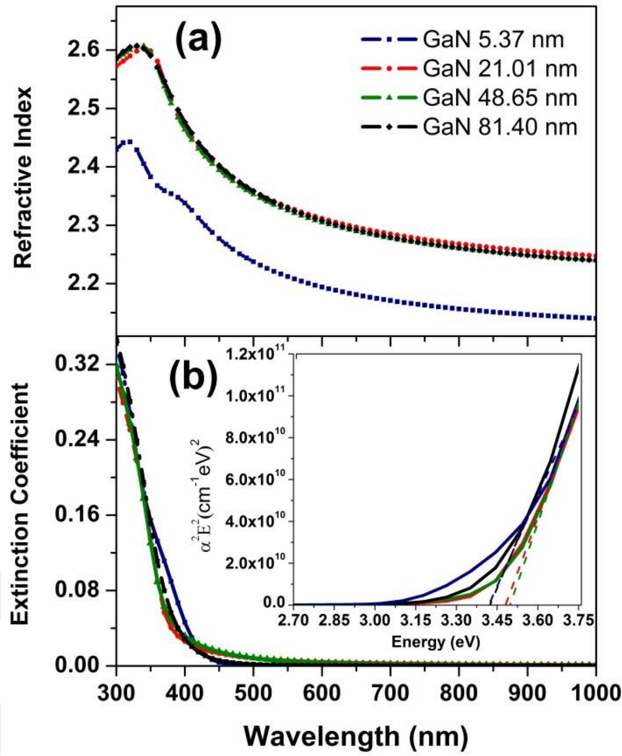

Figure 4.5. Evolution of (a) the refractive index and (b) extinction coefficient as a function of the wavelength for GaN having different film thicknesses. The inset displays optical band edge values calculated from spectroscopic ellipsometry data.

The value of *n* at 630 nm is 2.186, 2.302, 2.295 and 2.298 for increasing film thickness from 5.37, to 81.40 nm. These values agreed well with refractive index values of polycrystalline GaN films previously reported [10, 139]. The extinction coefficient values increase rapidly below 450 nm in wavelength and have similar behavior for all GaN films. For higher wavelengths *k* is zero,indicating that films are transparent above 400 nm in wavelength. Therefore the thickness does not affect the optical absorption in the visible region significantly [140]. Moreover, the spectral behavior of *k* in this study is consistent with previously published results. The optical band gap determined using $\alpha(\lambda)=4\pi k(\lambda)/\lambda$ by linear regression analysis for the optical absorption spectrum as shown in inset plot in Fig. 4.5(b), where $\alpha(\lambda)$ was calculated from the $k(\lambda)$ values. The deduced optical band gap values of GaN films were found to be 3.44, 3.472, 3.49 and 3.447 eV for films with thickness 5.37, 21.01, 48.65 nm and 81.40 nm, respectively. The optical band gap values

are slightly larger than the bulk GaN value of 3.4 eV [141]. The origin of this difference is discussed later in this section.

The refractive index values of the layers, as shown above, are lower than for bulk single crystalline GaN, indicating changes in film microstructure and morphology [91, 137]. The Bruggeman effective medium model is utilized to estimate the effect of void fraction in the GaN bulk layer [20]. The variation of the refractive index with film thickness is modelled using Bruggeman EMA. The fill fraction is as in the following:

$$f_{GaN}\frac{\varepsilon_{air}-\varepsilon_{GaN}}{\varepsilon_{air}+2\varepsilon_{GaN}}+\left(1-f_{GaN}\right)\frac{\varepsilon_{bulk}-\varepsilon_{GaN}}{\varepsilon_{bulk}+2\varepsilon_{GaN}}=0\,, \tag{4.2}$$

where ε_{GaN} , ε_{air}, and ε_{bulk} correspond to the dielectric constants of the experimentally achieved GaN film, air, and ideal single-crystal GaN, respectively, and f_{GaN} is the fill fraction of the GaN component.[20]

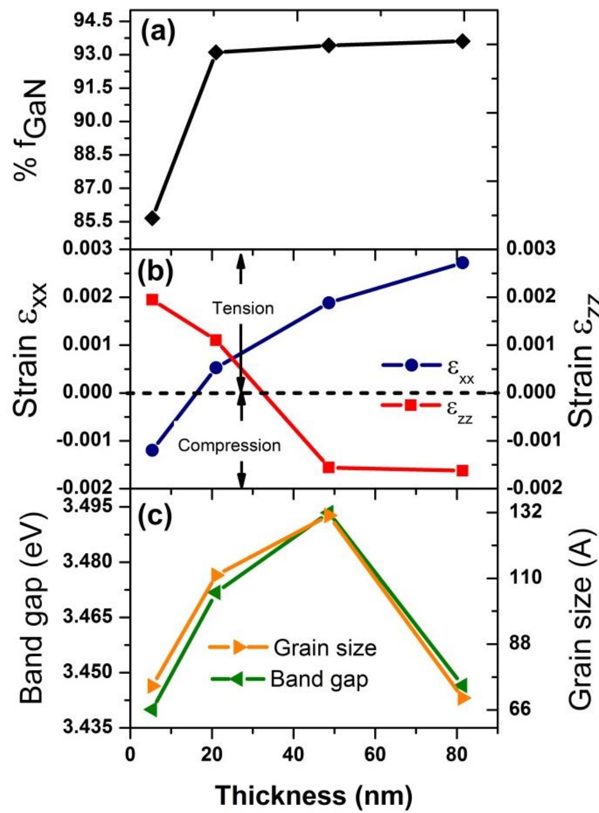

Figure 4.6. The estimated (a) fill fraction (b) strain in GaN films (c) grain size and optical band gap in dependence on the thickness of the GaN films.

The fill fraction as a function of film thickness is shown in Fig. 4.6(a). It is clear from Fig.4.6(a) that the fraction of voids is significantly decreased with increasing film thickness from 5.37 nm to 21.01 nm and then is almost stable above 48.65 nm. This suggests that optical film density and local crystallinity are improved with increasing film thickness to 48.65 nm, but increasing film thickness further does not seem to improve these features. Strain dependence vs. thickness for HCPA-ALD grown GaN films is shown in Fig. 4.6(b). The calculated strain values are listed in Table 4.1. The highest tensile strain of the GaN film was observed in the out of-plane directions for the film thickness below 48.65 nm. An increase in thickness of the film (<48.65 nm) results in a change of the sign of stress from tensile to compressive in out of plane direction. On the other hand, the in-plane tensile strain was observed for the film thickness below 21.01 nm. As the thickness of the film increased above 21.01 nm, tensile strain was dominant in the films in in-plane direction. Clear correlation between the optical band gap and the grain size of the films can be seen from Fig. 4.6(c). The plot shows similar trend between band gap and grain size with increasing film thickness. This trend reveals that the grain size or optical band gap indeed affects each other. As the film thickness increased to 48.65 nm, both the optical band gap and the grain size increased, and then started to decrease. The widening of the optical bandgap with an increase in thickness from 5.37 to 48.65 nm might be attributed to strain- induced defects and/or the quantum confinement effect due to small grain size [142]. However, in the case of 81.40 nm thick GaN film, the potential effect on the optical band gap might be attributed to defect states at grain boundary regions of GaN [143].

4.2. Thickness Effect of GaN on Sapphire

4.2.1. Introduction

III-V nitrides semiconductors are the materials of choice with tunable direct bandgaps ranging from UV to IR wavelengths such as light-emitting diodes, laser diodes, photodetectors, and high power devices, etc.[144] High-quality GaN films are typically grown by plasma-assisted molecular beam epitaxy or by metalorganic chemical vapor deposition at high growth temperatures (> 650 °C). Therefore, the available substrates compatible with these techniques are limited to Si, silicon carbide, and sapphire

substrates. Among these materials, the most widely used substrate for the growth of GaN has been sapphire. Sapphire promises two advantages: readily available as a single crystal with diameters up to 8 inches and transparent over the spectral range needed to study GaN optically. On the other hand, sapphire is insulating, thus confining the electrical transport to the GaN layer grown on it. One of the reasons sapphire has been so successful as a substrate for GaN epitaxy is simply that more research has gone into developing procedures for producing good quality films and high-performance devices on it compared to other substrates. However, sapphire has a lattice mismatch of 16% to GaN. The large lattice mismatch between the sapphire and GaN results in high dislocation density which degrades the electronic and optical performance of the devices. A thin buffer layer was introduced between GaN and the substrate in order to reduce the biaxial stress. In addition, the large disparity in optimal growth temperatures limits the indium corporation into the InGaN alloy due to the low vapor pressure and disassociation temperature of InN [145]. Furthermore, potential optoelectronic application of this wide bandgap material could be extended to wearable electronics if the deposition of III-N materials on flexible polymeric substrates is established. Apparently, low-temperature growth is promising to get rid of these drawbacks. Atomic layer deposition offers alternative pathways that make it possible to deposit films at lower temperatures with good process control and high conformality.

Recently, atomic layer deposition has been examined for deposition of GaN and shows a great promise [10, 55, 139, 146, 147]. Plasma-assisted atomic layer deposition is utilized to decrease the substrate temperature substantially as low as 200°C. Deposited films on Si (100), Si (111) and sapphire were poly-crystalline with hexagonal (002) preferred orientation [58]. Another study [148] reported PA-ALD of GaN with triethylgallium and forming gas, where they observed the crystallinity of GaN films at 275 °C. Recently, electron enhanced ALD of polycrystalline hexagonal wurtzite GaN was reported at 100 °C and room temperature using trimethylgallium, hydrogen radicals and ammonium (NH_3) as reactants [147]. A survey of this literature shows that there is no comprehensive report on the UV and IR optical properties of GaN thin films grown on sapphire by PA-ALD method. No ellipsometric measurement of the IR dielectric function and Raman measurement of E_2^{High} phonon modes on PA-ALD grown GaN in low-temperature region

were reported so far. To fill this knowledge gap, this study aims to investigate the optical constants and phonon modes of GaN films.

In the present work, we report the influence of the film thickness on the refractive index and phonon properties of GaN thin films that were grown on sapphire substrates by HCPA-ALD. We present the model dielectric functions (MDFs) of GaN obtained from single layer structure for wavelength from 300 nm to 1000 nm (visible) and for wavenumbers from 300 to 1200 cm^{-1} (IR). These MDFs were used to calculate the complex optical dielectric functions $\epsilon = \epsilon_1 - i\epsilon_2$ and refractive index $\sqrt{\epsilon} = n - ik$ for GaN with different thicknesses studied in this work. The optical constants and the bandgap of the GaN deposited on sapphire substrates at low-temperature were obtained and comparatively analyzed. A combination of two techniques was used: infrared spectroscopic ellipsometry and Raman spectroscopy where two techniques are complementary. IRSE allows an identification of $E_1(TO)$ and $E_1(LO)$ phonon parameters, while Raman spectroscopy ensures access to $A_1(TO)$ and E_2^{High}. In addition, the dielectric functions are basic parameters for FIR detector designs. We have also observed an interesting phenomenon that GaN films with thicknesses above 52.01 nm have different behaviors compared to the thinner GaN films.

4.2.2. Film Growth

GaN thin films with different thickness ranging between 6.57 and 84.35 nm were grown on *c*-plane sapphire templates using a HCPA-ALD system. Prior to the depositions, sapphire substrates were cleaned using the RCA cleaning procedure in order to minimize the adventitious oxide and surface contaminants. The substrates were exposed to the N_2/H_2 plasma (60s) and afterwards 60 s of N_2 plasma at 200 °C before GaN deposition. The nitridation of sapphire before the growth of GaN is an important step for reducing the defect density, and enhancing the electron mobility [149]. GaN thin films were deposited using optimized process parameters [123] and triethylgallium (TEG) was used as gallium (Ga) precursor as suggested in Ref [10]. For the purpose of comparison, GaN films were grown with identical parameters on the sapphire substrate. Ga and N precursors were adjusted in order to achieve the self-limiting growth scheme, which is an evidence of ideal atomic layer deposition [123]. Each ALD cycle consisted of four steps: (1) TEG pulse for 0.5 s, (2) 10 s Ar purge, (3) 300 W N_2/H_2 plasma for 60 s (50 sccm

each), and finally (4) 10 s Ar purge. GaN layers were deposited at 200 °C with 130, 500, 1500 and 2500 deposition cycles.

4.2.3. Characterization of synthesized samples

Raman spectroscopic studies were carried for all GaN films with different thicknesses. All Raman measurements were performed with WITECH Alpha 300S Raman system in a backscattering geometry with 532 nm excitation wavelength. The Raman spectra were collected through a 100X objective lens and recorded with a grating of 2400 lines/mm which has a spectral resolution of 0.25 cm^{-1}. For a reference, Raman spectra of a c-plane sapphire were also measured.

All samples were measured at room temperature by variable-angle spectroscopic ellipsometry for photon wavelength from 300 to 1000 nm at various incidence angles (60°,65°, and 70°). The film thicknesses and optical constants of the samples were extracted from the measured SE (V-VASE, J.A. Woollam Co., Inc.) data. IRSE measurements were performed in the wavenumber range of 300 to 1200 cm^{-1} with a spectral resolution of 8 cm^{-1} using a VASE-Woolam rotating-compensator apparatus at 72° angle of incidence.

4.2.4. Raman spectroscopy line shape analysis and determination of carrier concentration

Raman spectroscopic studies were carried for all GaN films with different thickness. For a reference, Raman spectra of a c-plane sapphire were also measured. Figure 4.7 shows the Raman spectra of GaN thin films with different thickness and sapphire substrate. The two peaks E_2^{High} and A_1(LO) phonon mode around 567 and 730 cm^{-1}, respectively, are the characteristic peaks of the GaN lattice and due to the vibration of Ga and N atoms [102, 150].

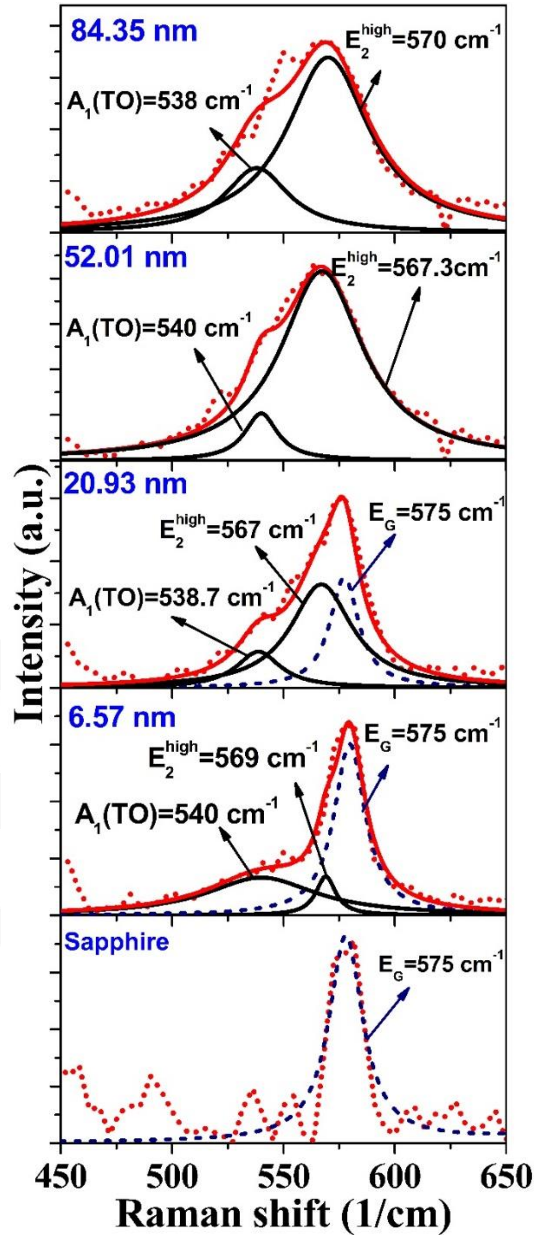

Figure 4.7. The Raman E_2^{High} phonon mode spectra of GaN films and theoretical fit of phonon modes.

Those peaks are related to the phonon modes of hexagonal wurtzite lattice and confirm the crystalline nature of the GaN films. We observe that the peaks around the 567 and 730 cm^{-1} from HCPA-ALD GaN films appear and strengthen as the film thickness increases. Those major GaN Raman modes are located near sapphire E_G modes at 575 and 750 cm^{-1} (See Fig. 4.7 and Fig 4.8). The broadening parameter of the sapphire phonon peaks at 575 cm^{-1} and 750 cm^{-1} is 18.4 cm^{-1}. These obtained parameters for sapphire

substrate were taken in to account in all subsequent Raman spectra calculations for analyzing the E_2^{High} and A_1(LO) phonon modes. As shown in Figure 4.7, the GaN E_2^{High} mode is influenced by Raman signal from the sapphire substrate for thinner films, which might cause incorrect assignments of phonon modes. It is apparent that the E_2^{High} mode is enlarged toward the low wavenumber side because of the presence of the A_1(TO) phonon centered at ~538 cm^{-1}. Therefore, we modelled the line shape of those two major phonon modes using Raman spectroscopy measurements. More details are given later in this section. The first question we have investigated was the Raman peaks shift with increasing thickness. It has been shown by various authors [102, 151, 152] that stress in crystalline samples can be correlated with Raman peak shift, since the GaN E_2^{High} mode is sensitive to biaxial stress. However, up to now, there has been no Raman study on PEALD grown GaN film. Raman spectroscopy has the advantage of being non-destructive and providing very detailed insight in to the variations of the stress in GaN structure. Using the measurement presented in Figure 4.7, a peak-shift analysis of the E_2^{High} phonon frequency was performed. For this purpose, information on the stress and crystalline quality can be extracted from the E_2^{High} phonon frequency and linewidth. The line shape of E_2^{High}phonon from Raman spectra was modelled using the following equation

$$I(\omega) \propto \int_0^1 \exp(-q^2 L^2/4) \frac{d^3 q}{\left[\omega - \omega(q)\right]^2 + \left(\Gamma_0/2\right)^2} \tag{4.3}$$

where q is expressed in units of $\frac{2\pi}{a}$, a is the lattice constant, L is the correlation length [102]. The dispersion $\omega(q)$ for optical phonons is

$$\omega^2(q) = A - Bq^2 \tag{4.4}$$

where A and B are adjustable parameters. The full width half maximum (FWHM) and wavenumber position of the E_2^{High} phonon modes that were obtained from the fitting of Raman spectra are briefly summarized in Table 4.5. Raman measurement and curve fitting for GaN samples with different thickness are shown in Figure 4.7. As seen in

Figure 4.7, our fits consist of contributions from the E_2^{High} phonon mode, Lorentzian shape mode for sapphire E_G at 575 cm^{-1} and A_1(TO) at ~ 540 cm^{-1}. Usually, compressive stress induces blue shift in phonon frequencies, while tensile stress induces a red shift. A standard value of 567.2 cm^{-1} for the E_2^{High} peak stress-free GaN is reported in the literature [153]. In our study, the frequency of E_2^{High} modes for GaN films with 6.57 and 84.35 nm thickness is higher than those observed values of stress-free bulk GaN film which is a result of the compressive stress. The Raman results indicate that large lattice mismatch between the GaN and sapphire produce larger compressive stress for GaN films with thickness 6.57 nm and blue shift of 2 cm^{-1}. As the thickness increases above 6 nm the stress state of GaN is affected by introduction of new GaN layers and compressive stress in films diminish from samples. However, the blue shift of E_2^{High} peak gradually enlarge for the GaN film thickness value above 52.01 nm and GaN films with thickness 84.35 nm are under compressive stress which might be due to thermal strain [151] and free carrier concentration in GaN film [154]. The FWHM of E_2^{High} can be used to assess the quality of grown materials. From Raman analysis of FWHM of E_2^{High}, it is found that the GaN film has better crystalline quality with decreasing film thickness. It obvious that the crystalline quality of GaN film does not further changes with increasing layer thickness above 52.01 nm.

Table 4.5. The Phonon frequencies (for q=0) of GaN films at room temperature

Thickness (nm)	*E_2^{high} (cm^{-1})*	*FWHM (cm^{-1})*	*A_1(LO) (cm^{-1})*	*FWHM (cm^{-1})*	*$N_{//}$ (10^{16} cm^{-3})*
6.57	569	10.80	740	60	2.184
20.93	567	33.40	730	35.34	1.1
52.01	567.3	45	731	43.41	1.22
84.35	570	45	731.5	48.58	12.18

The line shape analysis of A_1(LO) phonon mode leads to the determination of the free carrier concentration in the GaN. When doped with impurities in GaN, free carriers interact with the A_1(LO) optical phonons, but not with the non-polar E_2^{High} phonons [103]. The mechanism of Raman scattering by LO phonon-plasmon coupled modes in

GaN dominated by the deformation-potential and electro-optical scattering mechanism [102, 103]. A set of equations have been developed to determine the free carrier concentration in wide bandgap semiconductors [102]. The Raman intensity of A_1(LO) phonon mode is expressed by [102],

$$I_A = \frac{d^2S}{d\omega d\Omega} = \frac{16\pi\hbar n_2}{V_0^2 n_1}\frac{\omega_2^4}{C^4}\left(\frac{d\alpha}{dE}\right)^2 \left(n_\omega + 1\right) A\,\mathrm{Im}(-1/\varepsilon) \tag{4.5}$$

$$\begin{aligned} A = {} & 1 + 2C\omega_{TO}^2\left[\omega_p^2\gamma\left(\omega_{TO}^2 - \omega^2\right) - \omega^2\hbar\left(\omega^2 + \gamma^2 - \omega_p^2\right)\right]/\Delta \\ & + C^2\left[\omega_{TO}^4/\Delta\left(\omega_{LO}^2 - \omega_{TO}^2\right)\right]\left\{\omega_p^2\left[\gamma\left(\omega_{LO}^2 - \omega_{TO}^2\right) + \hbar\left(\omega_p^2 - 2\omega^2\right)\right] + \omega^2\hbar\left(\omega^2 + \gamma^2\right)\right\} \end{aligned} \tag{4.6}$$

$$\Delta = \omega_p^2\gamma\left[\left(\omega_T^2 - \omega^2\right)^2 + \left(\omega\hbar\right)^2\right] + \omega^2\hbar\left(\omega_L^2 - \omega_T^2\right)\left(\omega^2 + \gamma^2\right) \tag{4.7}$$

where V_0 is the volume of the unit cell, $n_{1,2}$ are the refractive indexes at the incident and scattered photon frequencies $\omega_{1,2}$,respectively; C is the Faust-Henry coefficient, α is the polarizability, E is macroscopic electrical field, n_ω is the Bose-Einstein factor, ω_{TO} and ω_{LO} are the TO and LO phonon frequencies, respectively. γ is the plasmon damping constant, ε is the dielectric function and η is the photon damping constant. The screened plasma frequency ω_p is given by

$$\omega_p = \sqrt{Ne^2 / \left(\varepsilon_\infty \varepsilon_0\right) m^*} \tag{4.8}$$

where N is the free carrier concentration, ε_∞ is the high frequency dielectric limit, ε_0 is the vacuum permittivity and m^* the electron effective mass. By taking γ , η, and ω_p and therefore the free carrier concentration as fitting parameters, the line shape of the A_1(LO) phonon can be fitted. This method has been successfully applied to obtain the carrier concentration in GaN. Figure 4.8 shows our theoretical fit and the individual contribution of A_1(LO). Because of the existence of a sapphire E_G mode at 750 cm^{-1}, our fits consist of a contribution from the A_1(LO) phonon mode and a Lorentzian shape mode for sapphire E_G, which is similar to the previous fit for E_2^{High} phonon mode. A fairly good fit

has been obtained with reasonable values of the A_1(LO) phonon frequencies and free carrier concentration values and tabulated in Table 4.5.

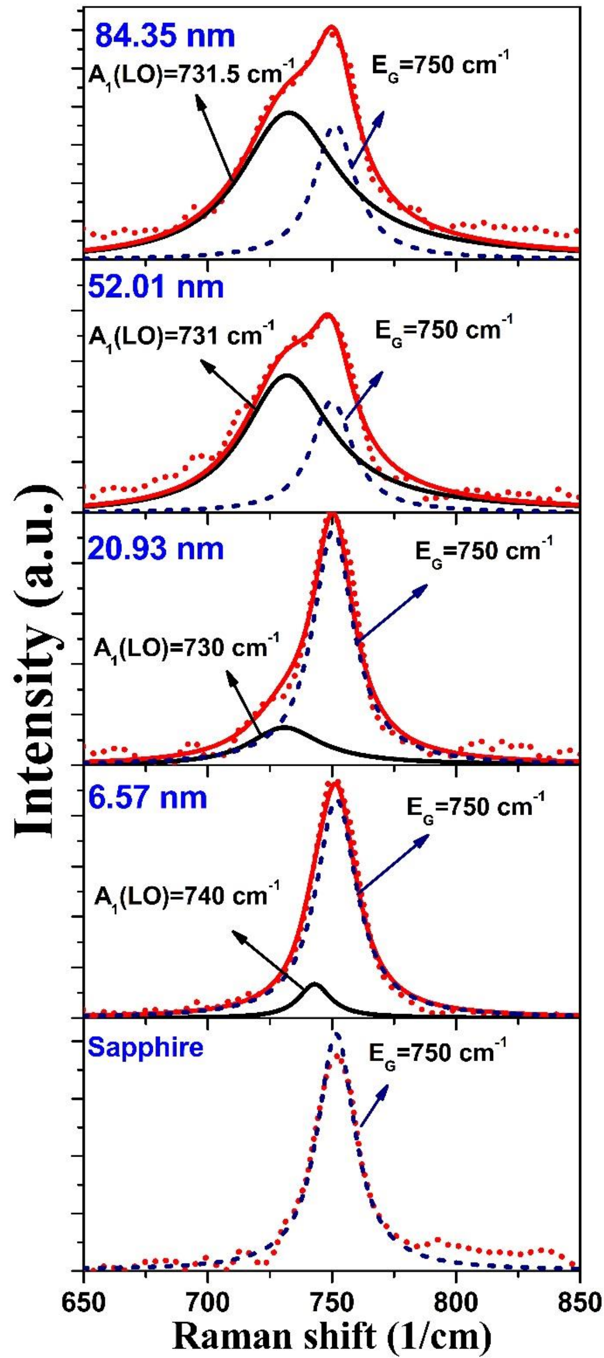

Figure 4.8. Raman lineshape analysis for the LO-phonon and theoretical fit of A_1(LO) phonon mode.

The frequency of A_1(LO) (735 cm^{-1}) mode is lower than those observed value of bulk GaN or thick epitaxial film. A_1(LO) line shape analysis gives electron concentration

values in the range of low 10^{16} cm^{-3} for GaN films with thickness equal to and less than 52.01 nm. The highest electron concentration of ~2×10^{16} cm^{-3} has been obtained for the thinnest and thickest film. In Figure 4.9, the E_2^{High} Raman peak positions of GaN film is plotted alongside with the free carrier concentrations calculated as a function of film thickness. We propose that a further contribution to the blue shift in E_2^{High} phonon peak position arises from the higher doping levels in the 84.35 nm GaN film. Therefore, we observe a blue shift of E_2^{High} phonon mode due to the compressive stress and higher free carrier concentration in GaN films. We cannot find a direct correlation between A_1(LO) phonon mode frequency and free carrier concentration for the 6.57 nm GaN film. However, the increase in the peak of A_1(LO) Raman shift signifies an increase in the carrier concentration. Moreover, the line broadening of A_1(LO) and E_2^{High} with increasing thickness indicates disordered structure of these films.

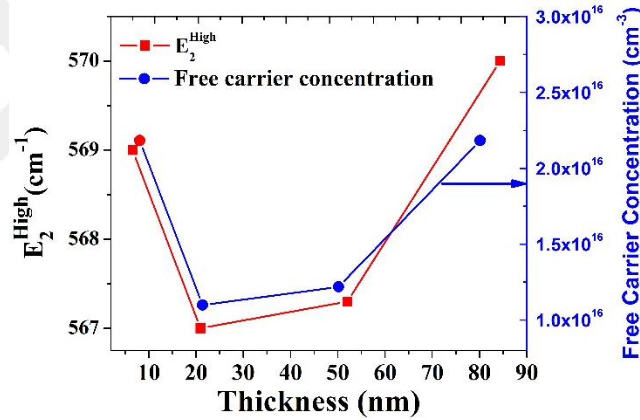

Figure 4.9. Free carrier concentration and E_2^{high} phonon peak position as a function of GaN thickness.

4.2.5. Influence of thickness on UV-Visible refractive index

The complex optical dielectric function $\varepsilon(\lambda)$ of GaN films were derived from spectroscopic ellipsometry by comparing the measured data with best-fit model calculations. The standard ellipsometric parameters were defined through Ψ and Δ of GaN films for angles of incidence 60°, 65° and 70°, respectively. Figures 4.10(a) to 4.10(d) show the ellipsometric angles Ψ and Δ for 6.57 and 84.35 nm GaN film on sapphire, respectively. A good agreement is obtained between the experimental data and fitting data

with mean squared error (MSE) < 5 for all samples. The ellipsometric data were interpreted in two independent steps assuming a 4-layer model (ambient/roughened GaN /GaN/Sapphire) for the accurate determination of the optical constants. In the first step, the unknown thickness of the GaN films and roughness layers were obtained. Thus, the dielectric functions for the transparent region (400–1000 nm) were obtained with the Cauchy model for bulk-like GaN and Bruggeman effective medium approximation (EMA) layer consisting of 50% of the GaN and 50% void for roughened GaN surface layer. Both the thickness of bulk-like GaN and surface roughness layer were determined by minimizing the MSE value for all measured spectra by varying Cauchy parameters and thickness of layers. The thicknesses of bulk-like GaN film were found to be 6.57, 20.93, 52.01, and 84.35 nm whereas the thicknesses of surface roughness layer were found as 0.15 nm, 3.18, 6.21 nm, and 6.49nm for 130, 500, 1500 and 2500 growth cycles, respectively. From the fitted results, the film thickness increases linearly with increasing number of deposition cycles, as expected for well-behaved ALD process.

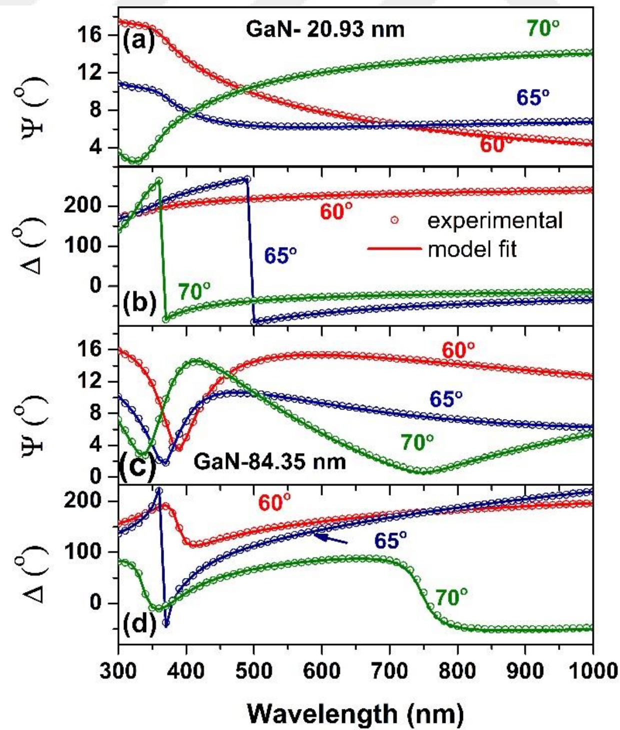

Figure 4.10. Ellipsometric angles Ψ and Δ as a function of wavelength for (a)-(b) 20.93 and (c)-(d) 84.35 nm GaN films, grown on sapphire substrates, acquired with incidence angles ranging from 60° to 70°; circles and lines represent experimental data and theoretical fit, respectively.

In the second step, we have used modified model dielectric function (MDF) with adjustable broadening for hexagonal materials proposed by Adachi et al.[77, 83] and modified by Kim et al.[82] in order to model the dielectric function of GaN over wide spectral region (300-1000 nm). Furthermore, the obtained thicknesses of bulk-like GaN and surface roughness layers from the first step were used as input parameters in the second step. In the UV visible spectral region of the complex dielectric function (DF) $\varepsilon_{GaN}(\lambda)$ is sensitive to band to band transitions ($\varepsilon_0(\lambda) and\ \varepsilon_1(\lambda)$), excitonic contributions ($\varepsilon_{0X}\ and\ \varepsilon_{1X}$) and additive constant ε_∞ [132, 133] given by

$$\varepsilon_{GaN}(\lambda) = \varepsilon_0(\lambda) + \varepsilon_{0X}(\lambda) + \varepsilon_1(\lambda) + \varepsilon_{1X}(\lambda) + \varepsilon_\infty \tag{4.9}$$

The refractive index n(λ) and the extinction coefficient k(λ) of GaN films on sapphire with different thickness were determined using the spectroscopic ellipsometry fitting and are shown in Fig. 4.11(a) and (b) as a function of wavelength, respectively. The peaks in the spectra of refractive index are due to the excitonic transitions at the bandgap edge, indicating the GaN samples are transparent in the wavelength region of the decrease of refractive index. The refractive index increases with film thickness up to 52.01 nm and is saturated gradually above this thickness. The value of *n* at 630 nm is 2.05, 2.23, 2.27 and 2.25 for increasing film thickness from 6.57 to 84.35 nm. These values agreed well with refractive index values of polycrystalline GaN films previously reported [10, 139]. The reduction of refractive index value with decreasing film thickness has been reported by other authors [135–138]. In order to give more qualitative and quantitative information on this reduction, we performed the Bruggeman EMA given by the following expressions:

$$f_{GaN}\frac{\varepsilon_{air}-\varepsilon_{GaN}}{\varepsilon_{air}+2\varepsilon_{GaN}} + \left(1-f_{GaN}\right)\frac{\varepsilon_{bulk}-\varepsilon_{GaN}}{\varepsilon_{bulk}+2\varepsilon_{GaN}} = 0\,, \tag{4.10}$$

where ε_{GaN} , ε_{air}, and ε_{bulk} correspond to the dielectric constants of the experimentally achieved GaN film, air, and crystalline GaN, respectively, and f_{GaN} is the fill fraction of the GaN component.

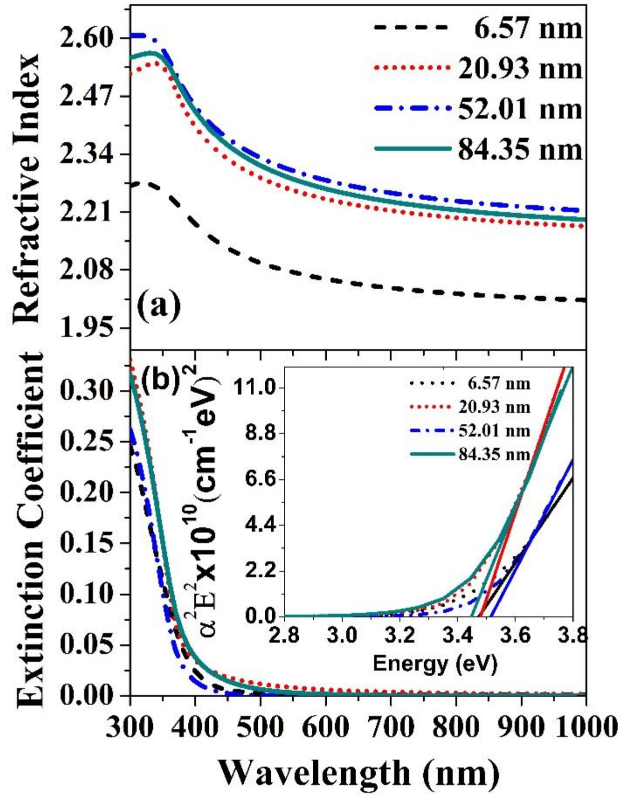

Figure 4.11. Optical functions (a) n and (b) k of the GaN layers calculated using the MDF and best-fit parameters obtained in this work. The inset of (b) shows the square of the absorption coefficient (α^2) vs. photon energy for GaN films with different thickness.

The fill fraction as a function of the film thickness is shown in Fig. 4.12(a). The analysis yields that the fraction of voids is significantly decreased with increasing film thickness from 6.57 nm to 52.01 nm and then is almost stable above 52.01 nm. The fraction of voids are effectively modulating the real and imaginary parts of the refractive index. Another important finding from Fig. 4.12(b) is the thickness dependence of the roughness layer. The increasing film thickness is also found to greatly reduce the increase in roughened overlayer thickness on the GaN surfaces. E_2^{High} modes in the Raman spectra are sensitive to biaxial stress in GaN films. The stress is reduced with increasing thickness to 52.01 nm (Fig. 4.12(c)) which is well correlated to the fill fraction and lattice defects. However, increasing film thickness further does not seem to improve these features.

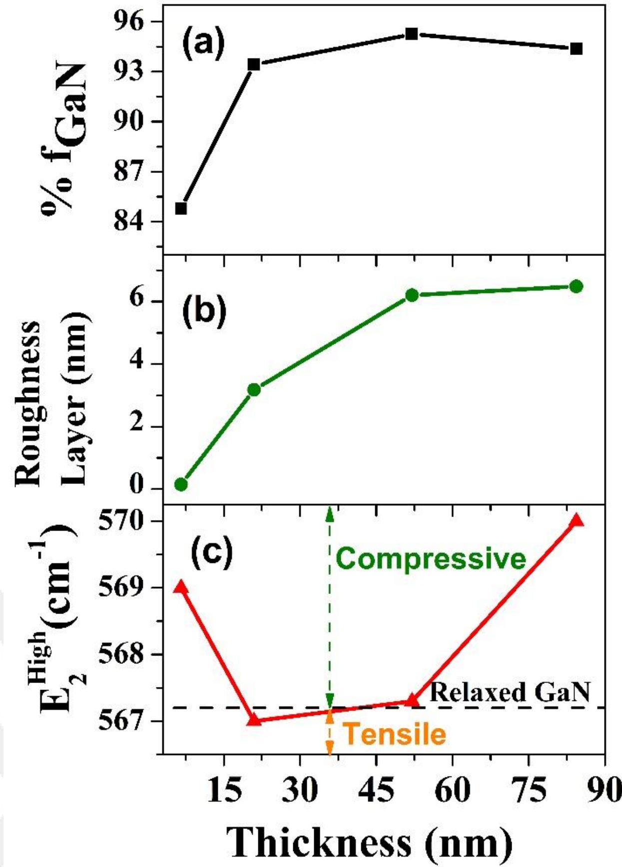

Figure 4.12. (a) Fill fraction, (b)surface roughness layer thickness (b), and (c) $\boldsymbol{E_2^{High}}$ phonon peak position of the GaN layers obtained from Bruggeman EMA, fitting to the SE data and fitting to the Raman Spectra as a function of the thickness.

The optical absorption coefficient (α) (defined as $\alpha(\lambda)=4\pi k(\lambda)/\lambda$, where λ is the wavelength of the incident light) was calculated over wavelength range (300-1000 nm). The optical band gap for GaN film was determined using a linear extrapolation of tangential line to the energy axis of $(\alpha(E))^2=0$, which is shown in the inset Fig. 4.11 (b).

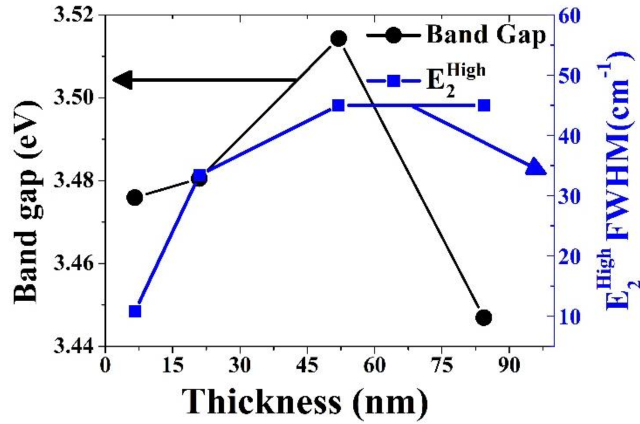

Figure 4.13. Band gap of the GaN layers with various thicknesses obtained from the exploration of $(\alpha(E))^2$ vs E. FWHM of the $\boldsymbol{E_2^{High}}$ phonons of GaN as a function of the thickness obtained from the analysis of Raman Spectra.

Fig. 4.13 shows the room temperature optical bandgap as a function of film thickness. The optical bandgap extracted from $(\alpha(E))^2$ fitting is not in good agreement with refractive indexes obtained by SE fitting. We expect that there would be a decrease in the bandgap of GaN film while an increase is observed in the refractive index. However, we have found a clear correlation between the bandgap and grain size of GaN grown on Si(100) in our previous report [57]. We reported that the optical bandgap increases with increasing grain size as the thickness increased up to ~ 52.01 nm and then reverse to decreasing behavior [57]. In this study, we have also observed that the tendency of the increase in the optical bandgap of GaN film reverses to decreasing behavior at 52.01 nm. In addition, we have found out that the GaN film has better crystalline quality with decreasing film thickness from Raman analysis of FWHM of E_2^{High}. The broadening of the Raman E_2^{High} peak indicates the increasing crystalline disorder with increasing thickness. The widening of the optical bandgap with an increase in thickness from 6.57 to 52.01 nm might be attributed to the crystalline disorder (Fig. 4.13). However, when the thickness is larger than the value of 52.01 nm, the band gap decreases to 3.45 eV which is still larger than the band gap of bulk crystalline GaN. The band gap is larger due to the compressive stress for thickness larger than 52.01 nm [57].

4.2.6. Influence of thickness on infrared refractive index and phonon modes

We determine the frequencies of E_1(LO), E_1(TO), and A_1(LO) phonon modes, the broadening values and the high-frequency dielectric constants for GaN films. IRSE is better than Raman spectroscopy for the study of the E_1(LO), E_1(TO) phonon modes because the strong intensity of E_2^{High} limits the resolution in Raman studies. At IR wavelengths, the dielectric function differs for electric field polarization parallel ($\varepsilon_{\parallel}$) and perpendicular ($\varepsilon_{\perp}$) to the c-axis. Therefore, the ordinary dielectric function ($\varepsilon_{\perp}$) and extraordinary dielectric function ($\varepsilon_{\parallel}$) was obtained by fitting Ψ and Δ data from 72° angle of incidence in a multilayer model, which accounts for the surface roughness layer via Bruggeman effective medium approximation.

Figures 4.14 (a-b) present the spectra of the ellipsometric parameters Ψ and Δ at 72° angle of incidence for the thinnest and thickest GaN films in the spectral range from 300 to 1200 cm^{-1}. The calculated data in Fig. 4.14 were obtained using a four phase model (ambient/surface roughness layer/GaN/ sapphire) for thinner films (6.57, and 20.93 nm) and five phase model (ambient/surface roughness layer/surface layer/GaN/ sapphire) for thicker films (52.01, and 84.35 nm). An extra layer is considered for thicker films and the dielectric function of surface layer was calculated by assuming GaN layer isotropic. Furthermore, we add two Gaussian oscillators to the dielectric function of surface layer. We use Lorentzian oscillator under harmonic oscillator approximation for the complex infrared dielectric function in order to fit the IRSE experimental results. The complex dielectric function is given by

$$\varepsilon_{\perp,\parallel} = \varepsilon_{\infty\perp,\parallel} \frac{\omega^2 - i\omega\gamma_{LO\perp,\parallel} - \omega_{LO\perp,\parallel}^2}{\omega^2 - i\omega\gamma_{TO\perp,\parallel} - \omega_{TO\perp,\parallel}^2} \tag{4.11}$$

where ω_{TO}, ω_{LO}, γ_{TO} and γ_{LO} denote the TO and LO mode frequencies, and the lattice mode broadening parameters parallel and perpendicular to the GaN c-axis, respectively[99].

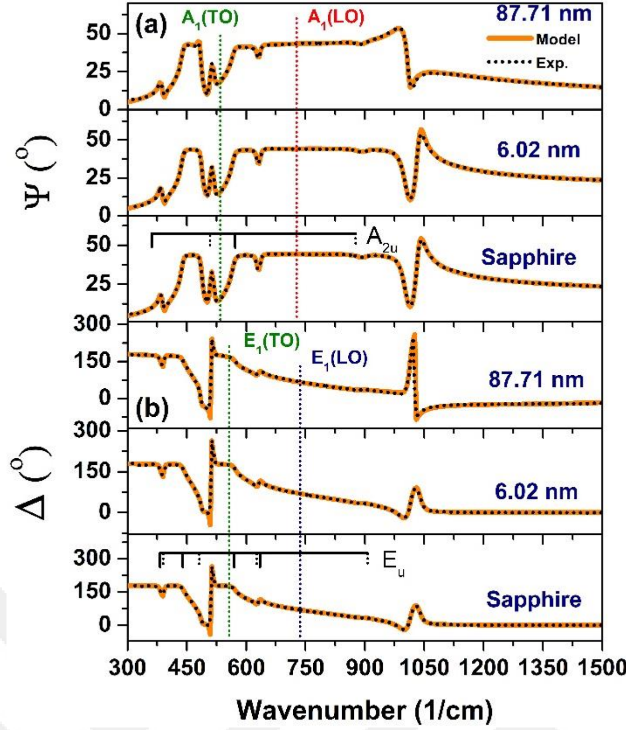

Figure 4.14. Experimental (dot) and calculated (solid lines) IRSE (a) Ψ and (b) Δ spectra of GaN films studied at 72° angle of incidence. The spectra of a bare sapphire substrate are included for comparison. The phonon modes are indicated by vertical lines. The solid (dotted) brackets indicate IR-active TO(LO) modes of sapphire.

In this work, the parameters $\omega_{TO,\parallel}$, $\omega_{TO,\perp}$, $\omega_{LO,\parallel}$, and $\omega_{LO,\perp}$ denote the frequencies of the GaN A_1(TO), E_1(TO), A_1(LO), and E_1(LO), respectively. $\varepsilon_{\infty,\perp}$ and $\varepsilon_{\infty,\parallel}$ are the high frequency limits for polarization perpendicular and parallel to the *c*-axis, respectively. Unfortunately, the entire parameter set cannot be obtained by the IRSE experiment. A_1(TO) phonon mode cannot be sensed by the IR probe beam due to the geometry of the experiment and crystal axis orientation of GaN, and A_1(TO) frequency taken as input parameter from our Raman results. Furthermore, GaN samples used in the present study are undoped with background carrier concentration lower than 5×10^{16} cm^{-3}, and therefore term related to plasmon was ignored. The model parameters that were allowed to vary during IRSE data analysis are the frequency and broadening parameters of the E_1(LO), E_1(TO), and A_1(LO) modes of GaN layer. The GaN film thickness was also allowed to vary during the data analysis.

Good agreement was obtained between the measured and calculated data for both samples. The spectral positions of the IR active GaN phonon modes are indicated by vertical lines (TO modes; LO modes) in Fig. 4.14. The IR active sapphire phonon modes of A_{2u} and E_u symetry are indicated for comparison within the lower parts of Fig. 4.14. (dotted: TO modes; solid LO modes). The plateaus in Fig. 4.14, where Ψ~45° corresponds to the bands of total reflection (restrahlen bands). In Figs. 4.14 total reflection occurs between the E_1(TO) and E_1(LO) phonon mode frequencies. A line shape analysis as described above is done to obtain the phonon modes of the GaN film. For the determination of the GaN film properties through the IRSE model calculations the dielectric function of the sapphire substrate was required. The sapphire dielectric function was determined previously by IRSE [94]. The dielectric function of the sapphire is calculated using Eq. 4.11. All sapphire parameters were taken from the literature [94] and kept constant during data analysis. The best-fit parameter values obtained for the samples are given in Table 4.6. Despite the apparently large number of unknown parameters, we have obtained very stable fits. As a result of IRSE data modelling, E_1(TO), E_1(LO), and A_1(LO) phonon mode frequencies determined are in good agreement with the strain-free frequencies of bulk GaN (558.2 cm^{-1}, 742 cm^{-1}, 735 cm^{-1} respectively) [155] and the variation of their frequencies as the thickness of the layer is varied is notable. The parameters of E_1(TO) and E_1(LO) modes from the GaN layers were extracted with small uncertainties and the parameters of A_1(LO) were determined from the IRSE data analysis with large uncertainties. IRSE results for the A_1(LO) frequency are very close to the frequency values determined from the Raman measurement excluding the frequency of 6.57 nm GaN film. However, A_1(LO) mode could not be obtained in reliable manner from the IRSE results. Therefore, the parameters deduced for A_1(LO) mode from Raman measurements are more accurate and reliable in this study (see Fig. 4.8). As seen in Table 4.6, a slight decrease in E_1(TO) frequency with increasing thickness up to 52 nm is observed, while E_1(TO) frequency is blue shifted with respect to stress free GaN bulk layer above 52 nm thickness. The observed blue shift of the phonon frequency indicates compressive stress for the thinnest and thickest film. We also observe from Raman analysis that a similar shift for the frequencies of E_2^{High} phonon as the thickness of GaN film increases. The E_1(TO) shift deduced from the IRSE data analysis show good agreement with the Raman scattering of E_2^{High} phonon shift. On the other hand, the

broadening values of the E_1(TO) phonon show a slightly increasing trend with increasing thickness. It indicates that crystalline disorder increases with increasing thickness. Note that the broadening values do not change so far for GaN films with thickness 52.01 nm and above. The IRSE broadening values for the E_1(TO) ($\gamma_{TO,\perp}$) modes of thinner GaN samples are smaller compared to thicker GaN samples, indicating a better crystalline quality. Accordingly the linewidth analysis of E_2^{High} phonon mode is in good agreement with IRSE data analysis of E_1(TO) mode. The parameters of the E_1(LO) modes were determined from the line shape analysis of the IRSE data. The E_1(LO) frequencies were determined with smaller uncertainties than those of the A_1(LO) mode. The E_1(LO) frequency shows a redshift for 20.93 nm and 52.01 nm thick GaN whereas E_1(LO) mode of GaN film shows a blue shift with increasing layer thickness above 52.01 nm. The fitted film thicknesses from the IRSE fitting listed in Table 4.6. The film thickness values obtained in infrared side slightly changes with respect to the values obtained in UV-visible side, which might be due the effects from infrared optical phonon modes. On the other hand, GaN film is transparent in the visible wavelength, which is crucial to determine film thickness. Therefore, thickness values obtained using UV-visible SE are taken as reference for this study. We observe that the high-frequency dielectric, $\varepsilon_{\infty,\perp}$ remained around 5.2 for GaN films with thickness larger than 20 nm. However, the lower $\varepsilon_{\infty,\perp}$ is 4.5 for 5.67 nm thick GaN film might be due to defects and vacancies which is well correlated to the fill fraction. We observe that the values $\varepsilon_{\infty,\parallel}$ found here range from 5.3 to 5.92 and the uncertainty limit for $\varepsilon_{\infty,\parallel}$ is ten times larger than for $\varepsilon_{\infty,\perp}$. The reason for that is the ellipsometry provides only little sensitivity to the index of refraction for polarization parallel to the *c*-axis of c-plane oriented uniaxial films.

Table 4.6. The Best-fit values of GaN from the IRSE data analysis for layer thickness d, GaN lattice phonon frequencies, high frequency dielectric constant, and the broadening values of the TO and LO phonon modes. The error limits, which correspond to 90% reliability, are given in parentheses.

[a] Assumed values, not varied during data analysis.

Film d(nm)	*Roughness layer* d(nm)	*Surface layer* d(nm)	$\varepsilon_{\infty,\perp}$	$\varepsilon_{\infty,\parallel}$	$\omega_{TO,\perp}$ [E_1(TO)] (cm^{-1})	$\omega_{LO,\perp}$ [E_1(LO)] (cm^{-1})	$\omega_{LO,\parallel}$ [A_1(LO)] (cm^{-1})	$\gamma_{TO,\perp}$ [$\gamma_{E_1(TO)}$] (cm^{-1})	$\gamma_{LO,\perp}$ [$\gamma_{E_1(LO)}$] (cm^{-1})	$\gamma_{LO,\parallel}$ [$\gamma_{A_1(LO)}$] (cm^{-1})
6.02 (0.231)	0.03	~	4.50 (0.11)	5.3 (1.43)	561.94 (7.81)	741.97 (10.77)	720.59 (7.68)	63.55 (13.16)	128[a]	23.38 (15.36)
19.32 (0.209)	3.35 (0.534)	~	5.20 (0.03)	5.74 (0.55)	561.65 (2.16)	734.75 (2.62)	733.57 (12.04)	48.51 (3.63)	96[a]	65.48 (23.41)
52.73 (0.333)	2.39	3.97	5.38 (0.02)	5.9[a]	556.38 (1.40)	738.45 (1.62)	728.00[a]	74.66 (2.49)	81.40 (2.34)	300.00[a]
87.71 (0.784)	2.36	3.97	5.19 (0.03)	5.92 (0.46)	559.90 (1.40)	747.18 (1.80)	735.00[a]	73.88 (2.74)	97.85 (2.90)	186.05 (60.23)

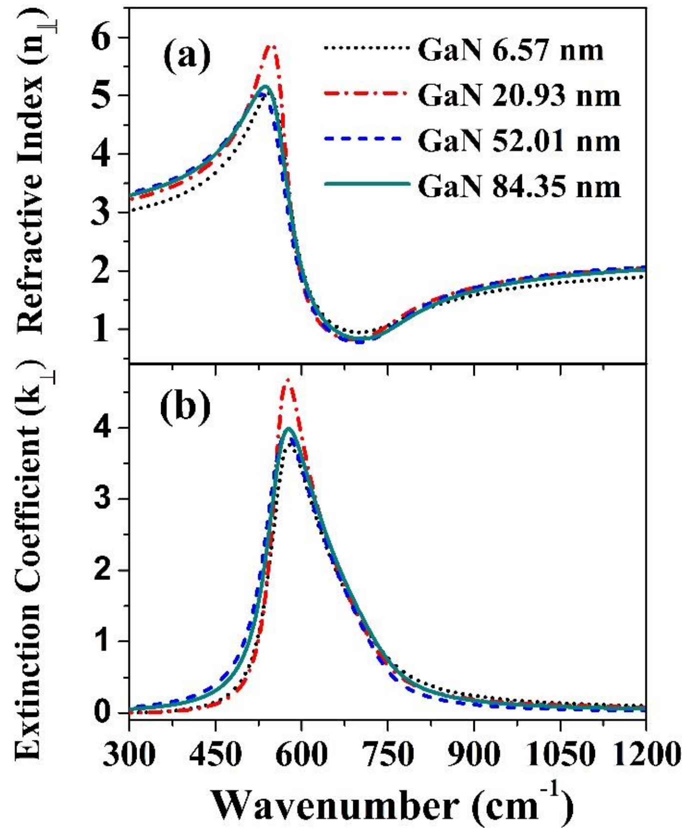

Figure 4.15. (a) Refractive index (n) and (b) extinction coefficient (k) of GaN layers with different thickness perpendicular to the *c*-axis obtained from the best fit IRSE data analysis.

Figure 4.15 presents the optical constants $n_\perp$ and $k_\perp$ of the GaN layer in the FIR spectral range calculated with the FIR dielectric function (Eq. 4.11) by using the values of the parameters given in Table II. The low-frequency part of the refractive index of the GaN films is related to the E_1(TO) and A_1(TO) phonon modes where TO phonons give rise to peaks in $n_\perp$. In the transparent region above 750 cm^{-1} refractive index ($n_\perp$) is about 2.0, which is closer to the reported values (2.2) obtained from the IR reflection spectra of GaN [156]. The refractive index of the GaN films are slightly below that high-quality GaN films indicating a weakening of the local structural bonding in the wurtzite lattice. Moreover, the refractive index of GaN films does not obviously change with increasing thickness at the high wave numbers. The difference for refractive index of the GaN thin films might be due to the crystalline quality of the GaN films. The peak position of the extinction coefficient (correspondingly to the E_1(TO) phonon) shows a redshift trend with

increasing thickness. The extinction coefficient ($k_{\perp}$) increases with increasing thickness indicating that the far infrared absorption coefficient increases. In addition, the extinction coefficient increases with decreasing thickness at the high wave numbers (short wavelength), where GaN films are nearly transparent.

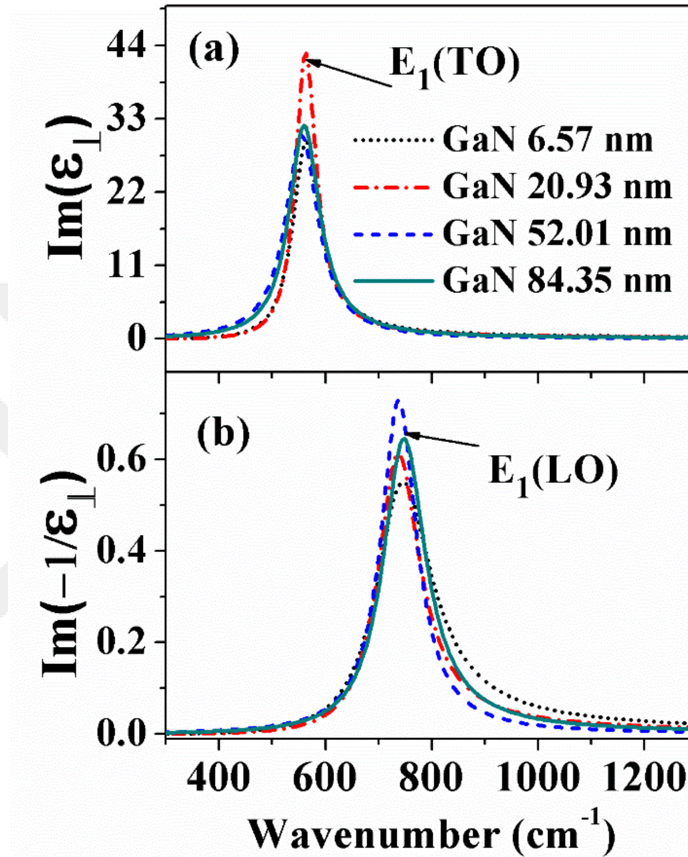

Figure 4.16. (a) $\{\boldsymbol{Im\varepsilon_{\perp}}\}$ and (b) $\{\boldsymbol{Im}\,{}^{-1}/_{\varepsilon_{\perp}}\}$ spectra of all GaN layers obtained from the best fits to the experimental IRSE spectra and showing the E_1(TO) and E_1(LO) modes.

The $\{\mathrm{Im}\varepsilon_{\perp}\}$ and $\{\mathrm{Im}\,{}^{-1}/_{\varepsilon_{\perp}}\}$ spectra of all four GaN layers, which were obtained from the best fits to the experimental IRSE spectra, are depicted in Fig. 4.14 (a) and (b). The E_1(TO) phonon mode appears as a peak in the imaginary part of the GaN dielectric function perpendicular to the *c*-axis (Fig. 4.14 (a)). The degree of the stress in the GaN films with respect to the shift of the E_1(TO) frequency was previously explained in this section. The E_1(LO) phonon was extracted from the best fit to the IRSE data and it appears

as a peak in the dielectric loss function parallel to the *c*-axis plotted in Fig. 4.16(b) for all GaN films. Table 4.6 summarizes the E_1(LO) and E_1(TO) phonon mode parameters.

5. PROPERTIES OF GROUP III-NITRIDES GROWN BY HCPA-ALD

The work described in this chapter published as:

"Influence of N_2/H_2 and N_2 plasma on binary III-nitride films prepared by hollow-cathode plasma-assisted atomic layer deposition." *Mustafa Alevli, Neşe Güngör. Journal of Vacuum Science & Technology A: Vacuum, Surfaces, and Films, 36(1), 01A110 (2018).*

5.1. Introduction

There are increased number of publications focusing on the PA-ALD of III-N compounds using either metal organic or halides as metal precursors in the last decade. [123, 126, 157, 158] On the other hand, besides the conventional NH_3 precursor used for high-temperature III-N epitaxy, AlN, GaN, and InN films can also be grown using N_2/H_2 or N_2-only plasma where H_2 is reducing agent [123, 126, 157, 158]. If carefully tuned, N_2/H_2 or N_2-only plasma species might allow more efficient chemical bond breaking via their high nitrogen radical densities. Recently, we reported the HCPA-ALD of crystalline AlN, GaN, and InN films using either N_2-only and N_2/H_2 plasma [123, 139, 158]. This study reports the effect of plasma gas composition on the structural and optical properties of deposited binary nitride thin films. Towards this goal, AlN, GaN, and InN films were deposited on Si (100) substrates using N_2-only (50 sccm), as well as N_2/H_2 (50+50 sccm, 50+25 sccm) plasma in order to investigate the impact of H_2 flow. A comprehensive analysis of the optical properties, variations of the thicknesses, phonon positions, refractive indexes and band gaps by increasing H_2 flow are discussed. Recently, spectroscopic ellipsometry (SE) has been used to determine the influence of different N_2/H_2 plasma flows on the optical properties of GaN and InN films grown using HCPA-ALD [123, 159]. However, comprehensive SE characterization for the optical properties of GaN and InN films deposited with different N_2/H_2 plasma flows has not been reported. To the best of our knowledge, there are no reports on infrared optical properties of HCPA-ALD grown III-N binary layers by varying N_2/H_2 plasma gas as well.

5.2. HCPA-ALD III-Nitride Film Deposition

III-N binary layers (AlN, GaN, InN) were grown on Si (100) using a modified Ultratech/Cambridge Fiji 200 ALD system in which quartz-based ICP source was replaced with a stainless steel hollow-cathode plasma source (Meaglow, Inc.). For comparison purpose, only N_2/H_2 flows were varied while III-N binary layers were grown at 200 °C using optimized HCPA-ALD parameters [123, 158]. HCPA-ALD process parameters including organometallic precursor pulse time, N_2/H_2 plasma exposure time, purge time have been optimized for self-limiting depositions of (Al, Ga, In)N layers and the details have been reported elsewhere [123, 158]. The(Al, Ga, In)N layers were grown at 200 °C using Trimethylaluminum (TMA), Trimethylgallium(TMG) and Trimethylindium(TMI) as aluminum, gallium, and indium metal precursors; whereas N_2/H_2 and N_2 plasma were used as nitrogen precursors, respectively. Each ALD cycle consisted of four steps: (1) 0.06 s TMA/ 0.03 s TMG/ 0.07 s TMI (duration of metal precursors feed in all experiments), (2) 10 s Argon(Ar) purge (The chamber is purged with Ar for all III-N binary layers growth in order to remove any unreacted precursor or reaction by products), (3) 40 s (AlN, GaN)/100 s (InN) of N_2/H_2 plasma exposure with 50 /(0, 25, 50) sccm N_2/H_2 flow rates under 300 W rf-plasma power (counter reactant nitrogen precursor pulse), (4) 10 s Ar purge, repeated for 600/900/700 cyles in order to deposit AlN, GaN, and InN films, respectively.

5.3. Film Characterization

In order to identify crystalline natures of (Al, Ga, In)N films, grazing-incidence X-ray diffraction (GIXRD) measurements were performed with a PANalytical X`Pert PRO MRD diffractometer using Cu K_α radiation. GIXRD data were collected in the 2Θ range of 25-75° with a step size of 0.1°. Incidence angle (ω) was 0.3° for GIXRD measurements. Chemical compositions of (Al, Ga, In)N films were determined by X-ray photoelectron spectroscopy (XPS) using a Thermo Scientific K-Alpha spectrometer with a monochromatized Al K_α X–ray source. For XPS survey scan from the bulk of films, etching of the (Al, Ga, In)N films was carried out *in situ* with a beam of Ar ions having an acceleration voltage of 1 kV. SE of (Al, Ga, In)N films were measured in the wavelength range of 200-1500 nm (200–1000 nm for GaN and AlN, 600–1500 nm for

InN) at various incidence angles (65, 70 and 75°) and a rotating analyzer (V-VASE, J. A. Woollam Co., Inc.). Vibrational properties of all films were primarily studied by room temperature infrared spectroscopic ellipsometry (IRSE) measurements and phonon mode frequencies were obtained from line shape analysis of the dielectric function. We use measured optical phonon mode positions to gain insight about the strain and bonding in (Al, Ga, In)N films. Ellipsometric measurements were carried out in the wavelength range 33.3-8.33 μm (300-1200 cm^{-1}) at room temperature at 70° angle of incidence using a variable J.A. Woollam IR-Vase ellipsometer.

5.4. Optical Modelling

We will discuss in detail how to extract the optical constants of InN, GaN, and AlN layers from the ellipsometric spectra. Experimental quantities measured by ellipsometry are the angles Ψ and Δ, which are acquired over a range of wavelengths and at multiple angles of incidence. The measured visible SE spectra from a layer sample were modeled using an iterative fitting in order to determine layer thicknesses and optical constants [160]. The structural model for modelling examined samples consists of three layers on top of a Si substrate. The top layer shows surface roughnesses of (Al, Ga, In)N thin films which were modelled as a homogeneous mixture of III-N bulk layer and void layer where $n=1+i0$ for void layer. The Bruggemann effective medium approximation (EMA model) was used to calculate the effective optical constants of this roughness layer [141]. The bottom layer is SiO_2 that was modelled with the dielectric function given in the WVASE32 analysis program.[160] The main target is the modelling of the middle (Al, Ga, In)N layers. The n and k for (Al, Ga, In)N are fit to the Gen-Osc model consisting of Psemi-MO function, which is a subset of the Herzinger-Johs Parameterized Semiconductor Oscillator function (Psemi) [160, 161]. Fitting parameters of (Al,Ga,In)N oscillators were refined until the best fit between the experimental and stimulated spectra was achieved. However, the structural model for modelling SE spectra of InN films deposited using N_2/H_2 plasma (50/25 sccm, 50/50 sccm) consists of four layers on top of Si substrate. The structural model and parameters determined from these analyses are given in Figures 5.4(c) and (d). Film thickness values were obtained along with the optical constants n and k. Finally, optical bandgap values for different N_2/H_2 plasma gas flows were calculated based on the extracted k values. The absorption coefficient, $\alpha(\lambda)=4\pi k(\lambda)/\lambda$, was calculated from the k

values determined from SE. Optical band gap (E_g) is expressed by the following equation for direct band gap materials, which can be analytically extracted via extrapolation of the linear part of the absorption spectrum to $(\alpha h\upsilon)^2=0$.

IRSE data were modeled using a four phase model: roughness layer/ III-N Layer/ SiO_2 layer/ Si (100) for (Al, Ga, In)N films for different flows of N_2/H_2 plasma. Top surface roughness layer was modeled using EMA layer of 50% bulk and 50% void [141]. The bottom layer is SiO_2 that was modelled with the dielectric function given in the WVASE32 analysis program [160]. Anisotropic (Al, Ga, In)N dielectric functions were parameterized using optically active IR phonon modes with Lorentzian line shapes which account for transverse (A_1(TO), E_1(TO)) and longitudinal optic (A_1(LO), E_1(LO)) phonon frequencies, $\omega_{TO,j}$ and $\omega_{LO,j}$, respectively, for polarization j= "∥", "⊥" to the crystal *c*-axis:

$$\varepsilon_j(\omega)=\varepsilon_{\infty,j}\prod_{i=1}^{l}\frac{\omega^2+i\gamma_{LO,ij}\omega-\omega_{LO,ij}^2}{\omega^2+i\gamma_{TO,ij}\omega-\omega_{TO,ij}^2} \tag{5.1}$$

$\gamma_{TO,j}$, and $\gamma_{LO,j}$ are the corresponding mode broadening parameters, and $\varepsilon_{\infty,\perp}$, and $\varepsilon_{\infty,\parallel}$ are the high-frequency limits for polarization perpendicular and parallel to the (Al, Ga, In)N *c*-axis. On the other hand, structural model shown in Figures 5.4(c) and (d) was used for modelling the IRSE spectra of InN films which were deposited using N_2/H_2 plasma.

Crystalline binary (Al, Ga, In)N dielectric functions were parameterized using dielectric function given in Eq. (5.1). However, this dielectric function is inadequate for modeling the infrared spectra of amorphous GaN and AlN films presented in this study. We think that the electron scattering in the disordered atomic structure exceeds the scattering induced by phonons. Therefore, a possible contribution from the free carriers to the dielectric functions of the amorphous (Al, Ga) N films is taken in to account using the classical Drude model:

$$\varepsilon_j(\omega)=-\varepsilon_{\infty,j}\frac{\omega_{p,j}^2}{\omega\left(\omega+i\gamma_{p,j}\right)} \tag{5.2}$$

with

$$\omega_{p,j} = \left(\frac{Ne^2}{\varepsilon_{\infty,j}\varepsilon_0 m_j} \right)^{1/2} . \tag{5.3}$$

Here, ω_p, ε_0, e, N, and m_j represent, in order, the plasma frequency, vacuum permittivity, magnitude of the electron charge, carrier concentration and effective mass.

5.5. Crystalline structure and composition

GIXRD patterns of the AlN and GaN thin films deposited with N_2/H_2 (50+50, 50+25 sccm) and N_2 (50 sccm) plasma were presented by Ozgit-Akgun *et. al.* [123] Therefore, GIXRD patterns of the InN films are the only XRD data presented in our study (Figure 5.1). Ozgit-Akgun *et. al.* have observed that GIXRD patterns of AlN and GaN thin films deposited with N_2/H_2 plasma remained almost unchanged when H_2 flow rate decreased from 50 to 25 sccm. AlN and GaN thin films were shown to be single-phase hexagonal wurtzite polycrystalline structure. On the other hand, the use of N_2 plasma without any H_2 resulted in amorphous GaN thin film with significant carbon and oxygen impurities within the bulk film. XPS scans detected 9.15 at % C and 11 at. % O in the amorphous GaN thin film. In the case of AlN thin film deposited using N_2 plasma, similar behavior was observed as the crystal structure is significantly altered to amorphous-like material due to the presence C and O impurities (8 and 54 at. %). The O concentration is much higher in the case of AlN thin film due to the oxidization of the film upon atmospheric exposure.[123] Interestingly, we did not observe similar results in InN thin films grown with N_2/H_2 plasma. We found out that the addition of H_2 plasma with N_2 plasma yielded InN film with poor crystalline quality showing high level of C (8.33 at. %) impurity with significant voids in the film. Furthermore, XPS studies do not reveal any C impurities for InN films deposited with N_2 (50 sccm) plasma only. GIXRD patterns of InN films deposited with different H_2 content in the N_2/H_2 plasma gas are shown in Figure 5.1. As seen from those figures, InN films deposited on Si(100) substrates using N_2 plasma (Figure 5.1(a)) and N_2/H_2 plasma with H_2 flow of 25 sccm (Figure 5.1(b)) retain their polycrystalline structures as single phase hexagonal InN. InN thin films deposited using N_2/H_2 plasma (50+50 sccm) show additional crystalline structures (Figure 5.1(c)). In contrast to AlN and GaN films deposited using N_2/H_2 plasma (50+50 sccm), phases of deposited InN films change from InN to In+ InN as hydrogen content in the plasma gas

is increased. The single hexagonal wurtzite InN phase can be grown using 0-25% hydrogen content in the N_2/H_2 plasma gas.

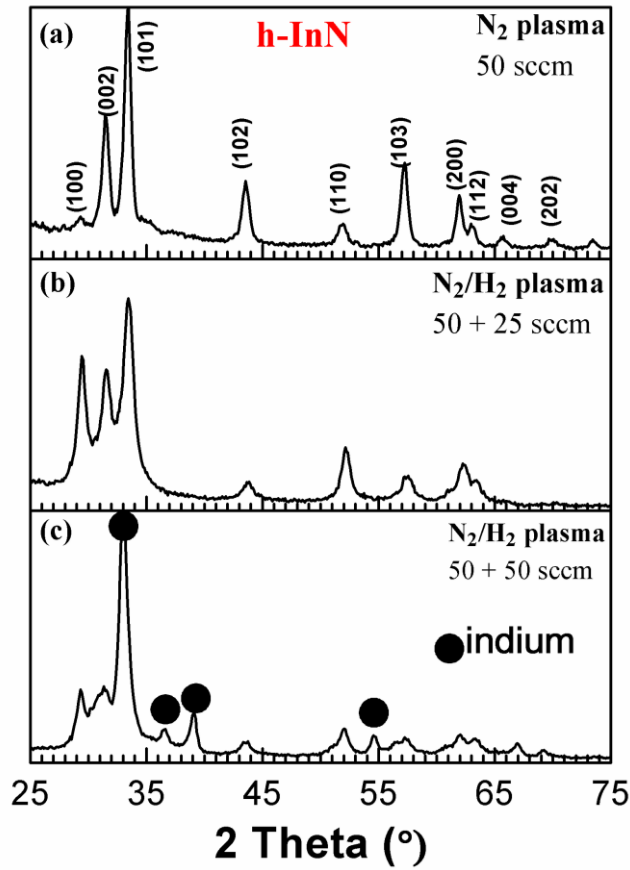

Figure 5.1. GIXRD patterns of InN thin films deposited at 200 °C on Si (100) substrates using (a) N_2 (50 sccm), (b) N_2/H_2 (50+25 sccm), and (c) N_2/H_2 (50+50 sccm) plasma.

In order to understand how the indium constituent of the InN films is bonded, In $3d_{5/2}$ high resolution XPS (HR-XPS) spectra of InN films were analyzed for different N_2/H_2 plasma flows, as shown in Figure 5.2. Chemical bonding states in the InN bulk films (t_{etch}=30 s for each InN film) were determined for the samples by the evaluation of their HR-XPS scans. Three distinct chemical states were observed for InN films and these three subpeaks are assigned to indium oxide, indium nitride and metallic indium. The In $3d_{5/2}$ HR-XPS spectra obtained from InN thin film deposited using N_2 plasma was fitted by two subpeaks located at 444.79 and 443.92 eV, corresponding to In-O[162] and In-N[163] bonds, respectively. According to the previous studies, In-O was about 1.0 eV higher in

binding energy compared to the binding energy of In-N bond [162, 163]. Therefore, the binding energy of 444.79 eV is assigned to In-O.

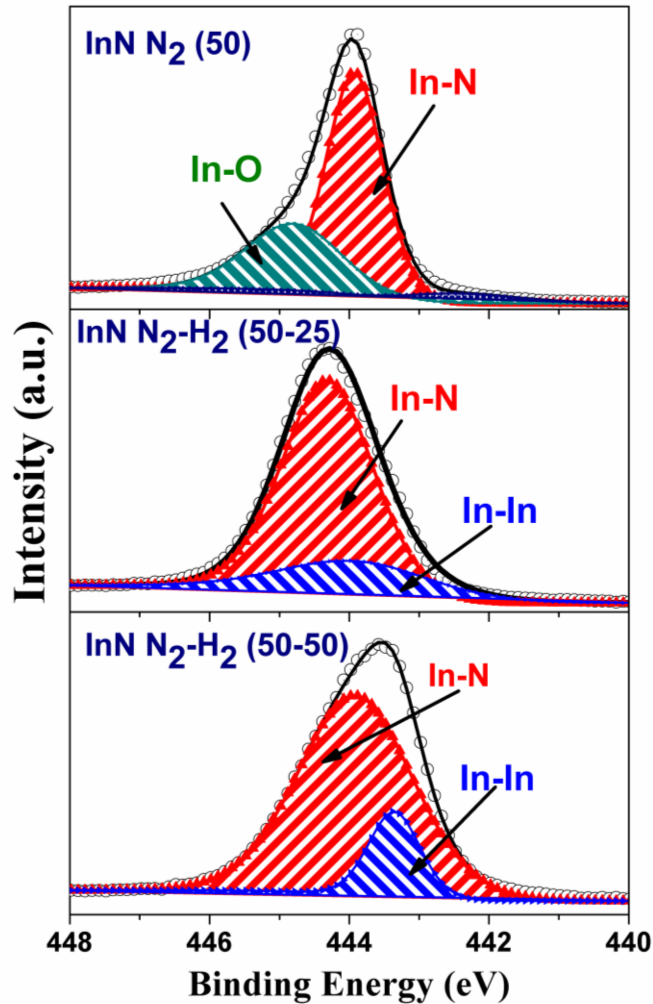

Figure 5.2. XPS of In $3d_{5/2}$ from InN thin films deposited at 200 °C on Si (100) substrates using different N_2/H_2 plasma flows. Solid line and open circles show experimental data and fitted curve, respectively.

Upon the use H_2 plasma, subpeak corresponding to the In-O bond disappeared, and the In $3d_{5/2}$ HR-XPS scan was fitted with another subpeak, which was attributed to the In-In bonding state. In $3d_{5/2}$ HR-XPS spectrum of InN film deposited using N_2/H_2 plasma (50+25 sccm) was fitted using two subpeaks located at 444.30, and 443.80 eV corresponding to In-N and In-In bonding states, respectively. The In $3d_{5/2}$ spectrum obtained from InN film deposited using N_2/H_2 plasma (50+50 sccm), which were again assigned to the In-N bond (443.90 eV) and In-In bond (443.36 eV). In-In bonding was

observed about 0.5 eV lower in binding energy compared to the case of In-N bond. Therefore, the binding energy less than binding energy of In-N bonding is assigned to In-In bonding. Furthermore, the XPS findings of In3$d_{5/2}$ are in line with the results obtained from the analysis of GIXRD and spectroscopic ellipsometry measurements. The existence of metallic indium in InN films deposited using N_2/H_2 plasma is confirmed.

5.6. Optical properties

Optical properties of (Al, Ga, In) N thin films on Si, namely, the refractive index, absorption coefficient, bandgap, and optical phonon modes were determined using UV-visible and infrared spectroscopic ellipsometry. Figures 5.3(a) and 5.3(b) show variations in the refractive index (*n*) and extinction coefficient (*k*) as a function of wavelength for (Al, Ga)N thin films grown with different N_2/H_2 plasma gas flows. For N_2/H_2 plasma processes, the refractive index of both AlN and GaN films deposited using N_2/H_2 plasma (50+50 sccm) found to be comparable to these of the films deposited using N_2/H_2 plasma (50+25 sccm). GaN films deposited with N_2/H_2 plasma exhibit a refractive index value of ~2.14 which is close to values of ~2.1 and 2.2 reported for the polycrystalline GaN film and slightly less than epitaxial GaN film deposited by MOCVD [141]. This refractive index value of GaN film is expected for thin films which might not be completely crystalline (less dense packing) [141]. Refractive indexes of AlN films increase from 1.99 to 2.01 when the H_2 flow increased from 25 to 50 sccm. Extracted refractive index values are in good agreement with polycrystalline AlN film refractive index values reported in literature [22]. Furthermore, a drop is seen in values of refractive index to ~1.57 and 1.87 for AlN and GaN films, respectively, upon the use of N_2 plasma, which indicates the deterioration of the film quality. Thicknesses of AlN films deposited with N_2/H_2 (50/50 sccm), N_2/H_2 (50/25sccm) and N_2 (50 sccm) plasma were determined to be 56.49, 56.16 and 103.87 nm, respectively. Thicknesses for GaN films deposited with N_2/H_2 (50/50 sccm), N_2/H_2 (50/25sccm) and N_2 (50 sccm) plasma are 19.44, 20.90, and 144.73 nm, respectively. Thicknesses of both AlN and GaN films follow similar behavior depending on the use of N_2 plasma and thicknesses increased enormously. As mentioned above, the use of N_2 plasma yielded high concentrations of C and O impurities in the AlN and GaN films which destroyed crystallinity. These results show that AlN and GaN PEALD process is very sensitive to the supply of reactive hydrogen radicals during film deposition

which might be avoided at higher growth temperatures due to the decomposition of methyl ligands of precursors.

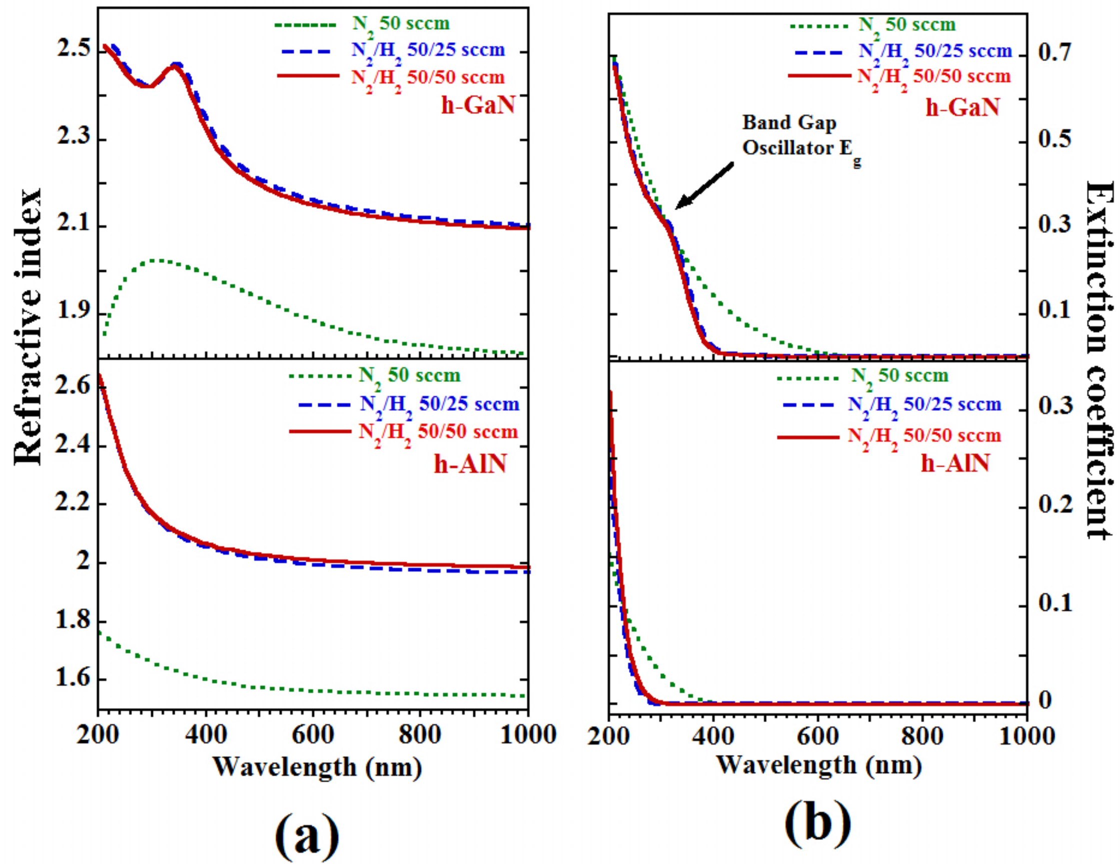

Figure 5.3. (a) Refractive index (n) and (b) extinction coefficient (k) for (Al, Ga)N films with different N_2/H_2 flows.

Modelling of InN films deposited with N_2/H_2 plasma is quite challenging since the optical properties of these films are affected by the amount of disorder in the samples. The Figures 5.4(c) and (d) summarize structural parameters determined from the SE analysis. The SE analysis yields that both three InN films have a rough over layer containing 50% voids. No metallic indium is observed in structures of InN films deposited with N_2 plasma. Therefore, the same structural model as in AlN and GaN films was used for modelling the SE spectra of InN films deposited with N_2 plasma. Nevertheless, a layer is described underneath the top rough surface layer which is a mixture of InN, metallic indium, and voids through Maxwell-Garnett EMA for InN films deposited with N_2/H_2 plasma.

The presence of metallic indium in the films indicates that the addition of H_2 with N_2 limit TMI-Nitrogen reaction. Values for *n* and *k* are shown in Figures 5.4(a) and (b) as a function of wavelength for InN thin films grown with different N_2/H_2 flows. Refractive index values of InN films deposited using N_2 (50 sccm), N_2/H_2 (50/25 sccm), and N_2/H_2 (50/50 sccm) were found to be 2.61, 2.38, and 2.36 at 650 nm, respectively which agree with reported values of polycrystalline InN thin films in the literature [159].

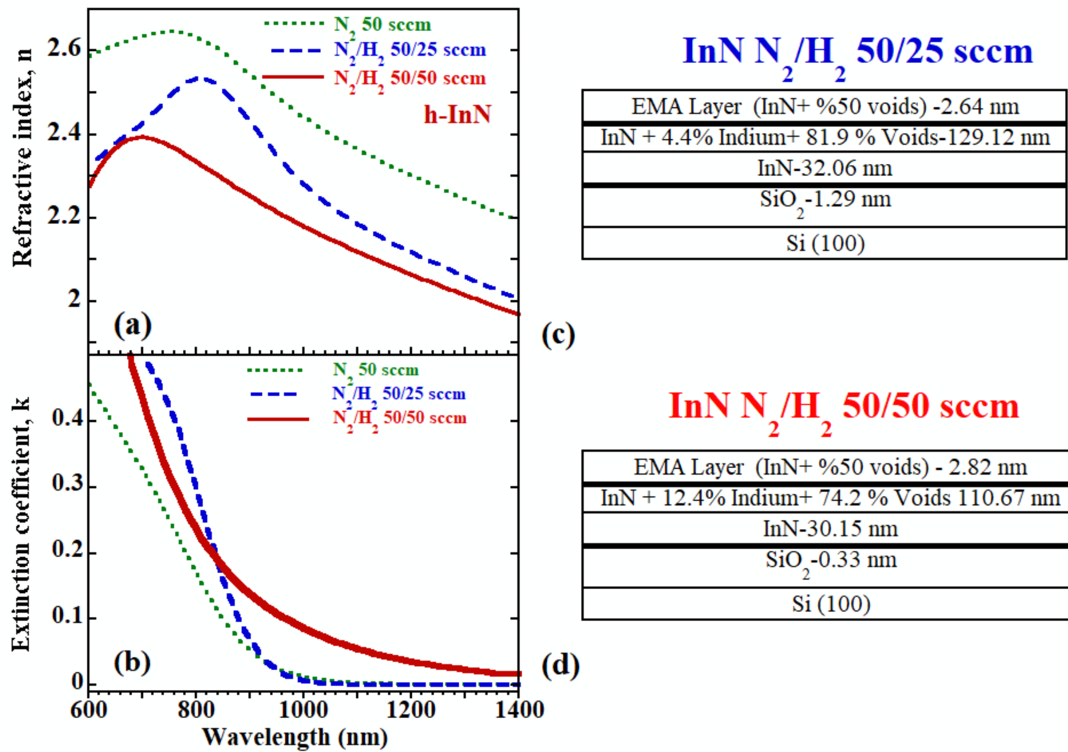

Figure 5.4. (a) Refractive index (*n*) and (b) extinction coefficient (*k*) for InN films deposited using different N_2/H_2 flows. (c) and (d) Structural sketch for InN films deposited using N_2/H_2 plasma.

By the way, increasing the H_2 flow rate to 50 sccm decreases the thickness of InN from 42.73 to 30.15 nm. Thickness and also refractive index values represent average values of InN films (one layer model). Thickness is the highest for the InN film (42.73 nm) deposited using N_2 plasma which also produced film with maximum refractive index (2.61).

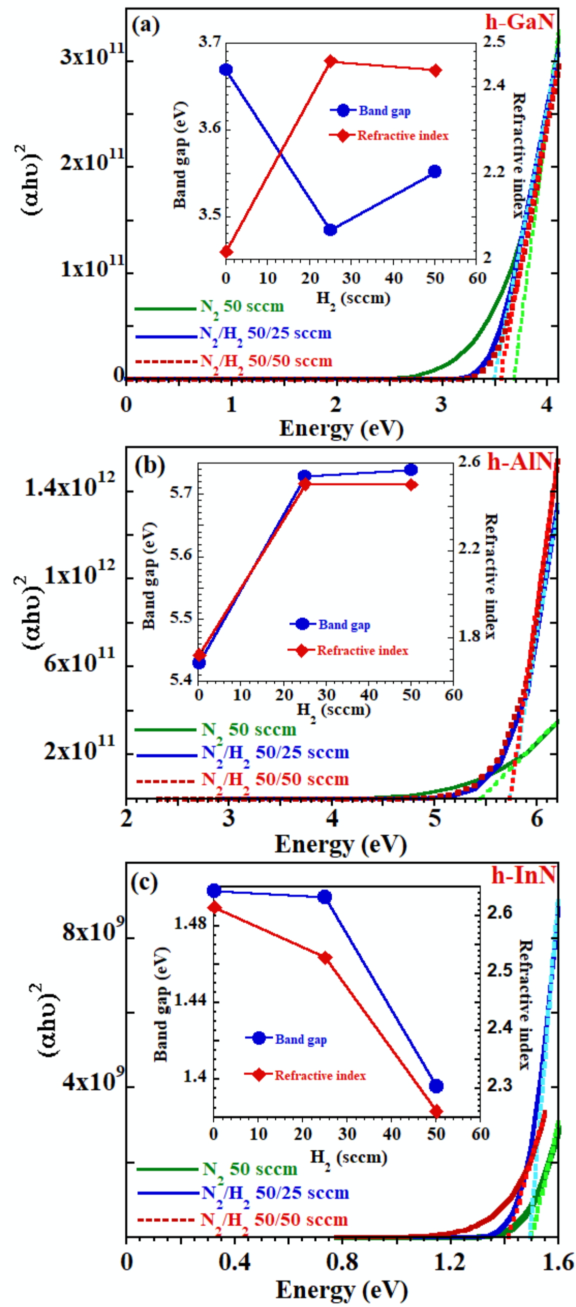

Figure 5.5. Optical absorption coefficient plots of (a) GaN, (b) AlN, and (c) InN films deposited on Si (100) substrates using different N_2/H_2 flow rates. The inset shows the optical band gap and refractive index versus hydrogen flows. The optical band gap was extracted from the optical absorption coefficient.

The magnitude of refractive index is stated by densities and/or polarizabilities of ions (due to material change). Therefore, the improvement of the refractive index might be

attributed to film densification as the thickness of the film is increased. On the other hand, carbon and oxygen concentrations were further increased with the introduction of H_2 plasma which deteriorates InN film quality. According to the SE analysis, formation of InN film deposited with N_2/H_2 plasma occurred on the substrate. Consequently, phases of deposited films change to In+ InN+voids. Clearly extensive amount of carbon and oxygen impurities present in InN films deposited using N_2/H_2 plasma were diffused into InN+In+voids matrix and were trapped inside this matrix. Direct optical bandgaps of (Ga, Al, In)N films were determined from optical absorption plots shown in Figure 5.5. An extrapolation is applied to the linear part of the plot (Figure 5.5) and then extended to $(\alpha h\upsilon)^2=0$. Optical band gap is extracted and correlated to the H_2 flow (Figure 5.5). The optical band gap of GaN film decreases from 3.67 eV to 3.48 eV as the H_2 flow increased to 25 sccm. The higher optical band gap of amorphous GaN film deposited using N_2 plasma might only be due to O and C impurities present in the film. Therefore, the decrease in the optical band gap is mainly due to the structural evolution from amorphous to polycrystalline state as observed in our previous GIXRD measurements [123].

Furthermore, the optical band gap of GaN increases to 3.55 eV as H_2 flow is increased from 25 to 50 sccm. Further increase in the optical band gap observed in crystalline GaN films might be attributed to the internal stress developed in the polycrystalline film and effective increase in imperfections at grain-boundary regions because concentrations of C and O impurities are similar in both GaN films deposited using N_2/H_2 plasma. Optical band gap values of AlN films deposited using N_2/H_2 plasma (50/0 sccm, 50/25 sccm, 50/50 sccm) were found to be 5.43, 5.73, and 5.74 eV, respectively. Optical band gap values of AlN thin films deposited with N_2/H_2 plasma agree well with values reported in the literature for polycrystalline AlN films in the range of 5.6-5.75 eV. Lower band gap value of AlN film deposited using N_2 plasma only is an indication of disorder and impurities in the film. Observations of band gap values are in good agreement with refractive indexes of both GaN and AlN films. Both GaN and AlN films begin to form a denser structure as the band gap value approaches to the bulk value of both AlN and GaN films. The band gap calculated for InN films deposited using N_2/H_2 plasma (50/0 sccm, 50/25 sccm, 50/50 sccm) is 1.498, 1.495 and 1.415 eV, respectively. These bandgap values are much larger than the well-established value of 0.7 eV reported for high quality single crystalline InN grown by MBE [164].

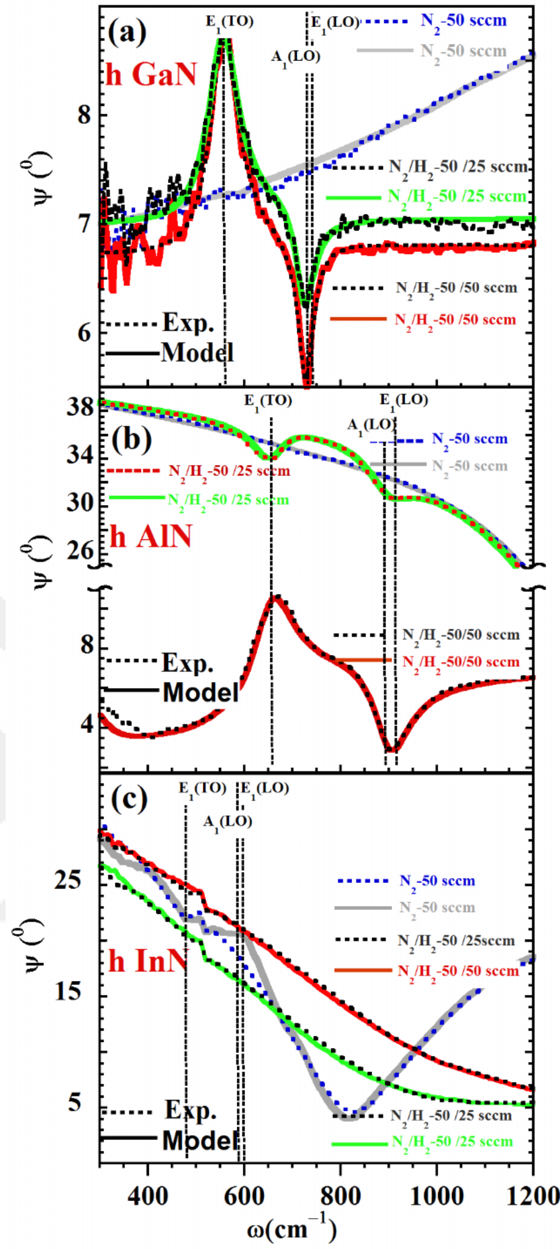

Figure 5.6. Experimental (dashed lines) and best-fit (solid lines) IR ellipsometric Ψ spectra of the (a) GaN, (b) AlN, (c) InN films deposited using N_2/H_2 and N_2 plasma. E_1(TO), A_1(LO) and E_1(TO) phonon modes of GaN, AlN and InN films were deposited on Si(100) substrates using different N_2/H_2 flow rates. Dashed lines are reported frequencies of phonon modes in the literature for strain free structures.

Origins of higher band gaps in these films are attributed to presences of oxygen inclusions and to the polycrystalline nature of InN films. However, SE analysis of InN films indicate that their band gap is inversely correlated with calculated refractive index. The InN films

presented in this work are not as dense as bulk InN films and band gap values obtained for InN films decrease with decreasing refractive index (insets Figure 5.5). Indeed, we expect the opposite at which the refractive index increases with decreasing optical band gaps of InN films. Further the optical band gap decreases as indium inclusions embedded in InN films are increased. Indium inclusions can affect the optical properties of InN films and can lower band gap due to the Mie resonances [164].

IRSE Ψ spectra of (Al, Ga, In)N films are shown in Figure 5.6. Model parameters that were allowed to vary during the IRSE data analysis are the E_1(TO), A_1(LO) and E_1(LO) frequency parameters. Consequently, the A_1(TO) phonon modes of GaN, AlN and InN could not be found since IR beam is insensitive to A_1(TO) phonon mode. Therefore, A_1(TO) phonon frequencies of GaN, AlN, and InN determined from literature were used in the modeling of IRSE spectra as parameters are fixed (532, 614, 447 cm^{-1}, respectively) [165]. For AlN and GaN films, features corresponding to the E_1(TO), A_1(LO) and E_1(LO) phonon modes are clearly observed for the deposition with N_2/H_2 plasma. On the other hand, IRSE spectra analyses do not reveal any AlN and GaN phonon modes for samples deposited using N_2 plasma. For GaN and AlN films, excellent agreement between the experimental (dashed lines) and best-fit (solid lines) data was obtained in the entire spectral range. Both GaN and AlN phonon mode frequencies determined by IRSE are consistent with those obtained previously by other deposition methods within usual variation range [165]. These values of the phonon mode frequencies derived from the fitting of the IRSE spectra are listed in Table 5.1. E_1(TO), E_1(LO) and A_1(LO) phonon modes of AlN have frequency values which coincide with strain-free layer values (670.8, 890, 912 cm^{-1}, respectively).E_1(TO) mode frequencies obtained for AlN films deposited with N_2/H_2 plasma are less than the strain-free value indicating the biaxial compressive stress of AlN films (Table 5.1).[166] However, we find slight differences for A_1(LO) and E_1(LO) mode frequencies between AlN films presented in this study and AlN relaxed layer. Frequency shifts of LO mode frequencies might be due to the existence of nitrogen vacancy point defects within AlN films. Strain-free frequencies of 558.8, 734 and 740 cm^{-1} are determined in the literature for GaN E_1(TO), A_1(LO), and E_1(LO) phonon modes, respectively [165].

Table 5.1. E_1(TO), A_1(LO) and E_1(LO) phonon frequencies (cm^{-1}) of GaN, AlN and InN deposited using N_2/H_2 and N_2 plasma

	GaN		AlN		InN		
N_2/H_2 (sccm)	50/25	50/50	50/25	50/50	50/0	50/25	50/50
Phonon Mode							
E_1(TO)	557.06	554.20	660.38	655.06	478.60	475.00	480.00
E_1(LO)	740.00	740.15	910.48	913.00	594.21	590.75	590.75
A_1(LO)	727.91	722.87	890.66	891.73	586.00	582.11	580.00

E_1(TO) and A_1(LO) values appear slightly blue-shifted with respect to the strain-free GaN, which might be related to the presence of interface disorder or possible delocalization effects [167]. At the same time, the E_1(LO) mode remains at the same frequency as the bulk GaN phonon mode with the increasing H_2 flow. In contrast to phonon modes of AlN and GaN, spectral features due to E_1(TO), A_1(LO) and E_1(LO) phonon modes of InN films are strongly damped and they almost vanish (see Figure 5.6). Therefore, E_1(TO), A_1(LO) and E_1(LO) phonon mode parameters of InN films were obtained from the line-shape analysis. For strain-free InN films, frequency positions corresponding to E_1(TO), A_1(LO) and E_1(LO) phonon modes are reported at 476, 586 and 593 cm^{-1}, respectively [90].

Determined E_1(TO), A_1(LO) and E_1(LO) frequencies from the IRSE spectra of the InN films are shown in table 5.1, which are in good agreement with published works. InN films deposited using N_2 (50 sccm) and N_2/H_2 (50/50 sccm) plasma experience compressive strain, while InN film deposited with N_2/H_2 (50/25 sccm) experiences tensile in-plane strain [168]. Here, we have related the shift of the E_1(TO) phonon frequency to the strain in the III-N layers. A_1(LO) phonon frequency shifts to lower frequencies as H_2 flow is increased, which confirms the disorder in InN films deposited using N_2/H_2 plasma.

Furthermore, both A_1(LO) and E_1(LO) modes appear at slightly lower frequencies than those of bulk InN which is attributed to phonon confinement effect.[169] Phonon propagation is interrupted in an isolated grain at the boundaries and remain confined within the grain.[169]

6. CONCLUSIONS

In this dissertation, group III-Nitride (AlN, GaN and InN) thin films grown by hollow-cathode plasma assisted atomic layer deposition (HCPA-ALD) was investigated with the motivation of (i) the deposition of III-nitride thin films at low temperatures required for temperature sensitive structures, (ii) effect of film thickness and substrate on properties of low-temperature grown GaN thin films, and (iii) the effect of plasma gas composition on the properties of deposited binary III-nitride thin films.

A series of GaN films with various thickness were prepared on Si(100) substrate by HCPA-ALD at low temperature as low as 200°C. In summary, the layer thickness can effectively influence the properties of GaN epilayers and the influence is due to the different grain sizes and residual strain in GaN films. The grain size values obtained from analysis of AFM images strongly correlated to the optical band gap values of GaN film. The SE analysis revealed that the tendency of increase of the optical band gap and grain size values reverses to decreasing behavior at ~48.65 nm. However, the refractive index increases for thickness < 21.01 nm and stabilizes at thickness ~48.65 nm. The crystal structure of the GaN films is hexagonal wurtzite and the films show strong preferential (002) orientation along the c-axis. It is found that the average residual strain in GaN thin films strongly correlates to the film thickness and changes from compressive to tensile strain with increasing thickness in the in-plane direction. The strain in out-of-plane direction has a large value at a film thickness of larger than 48.65 nm and assumed to be relaxed for the film thickness between 21.01 and 48.65 nm. The optimal thickness of the GaN layer deposited using HCPA-ALD to achive the best crystal quality, low strain and high optical properties is ~40 nm. These results are important for the growth control of high quality epitaxial GaN films at low temperatures and will open a pathway for producing future group III nitride devices at low temperatures on flexible materials.

We have also studied the phonon behavior in GaN films on sapphire with different thicknesses from 6.57 nm to 84.35 nm by combining the IRSE and Raman spectroscopy. A_1(TO), A_1(LO) and E_2^{High} modes were detected by Raman measurements. E_1(TO), E_1(LO), and A_1(LO) modes were detected by IRSE measurements. The analysis of E_1(TO), E_1(LO), and E_2^{High} modes indicated that GaN films with thickness 20-50 nm are

nearly stress free layers. The Raman spectroscopic measurement shows the GaN layers under study are polycrystalline and present an increasing structural disorder with increasing thickness. The broadening of Raman E_2^{High} peak indicates that the increasing crystalline disorder with increasing thickness and no further increase in crystalline disorder occurs above 52.01 nm thickness. A direct correlation has been found between E_2^{High} phonon frequency shift and the electron concentration. We propose that a further contribution to the blue shift in E_2^{High} phonon peak position arising from the higher doping levels in the 84.35 nm GaN film. The refractive index perpendicular (⊥) to *c*-axis of GaN films in the FIR region were determined by modelling SE spectra. The refractive index in the FIR region does not obviously change with increasing thickness. We further derived lattice phonon frequencies and broadening values. The lattice-mode parameters are in an excellent agreement with previous IRSE and Raman studies.

The band gap and optical properties of GaN thin films with various thickness below 100 nm have been determined using MDF based model. Both the band gap and optical properties show a strong dependence on the film thickness. The UV-visible SE analysis revealed that the refractive index GaN films increases with increasing thickness and stabilizes around 52 nm. For thickness smaller than 52.01 nm, the band gap expansion is observed due to structural disorder, however, for thickness larger than 52.01 nm, compressive stress is the dominant mechanism leading to the increase in the band gap of GaN.

GaN, AlN and InN films were prepared utilizing HCPA-ALD at 200 °C using trimethyl metal precursors and N_2/H_2 plasma. Three different values were used for the N_2/H_2 plasma flow. Resulting (Ga, Al and In)N films were evaluated as a function of hydrogen content in the N_2/H_2 plasma gas. Observations can be summarized as in the following:

1) Amorphous GaN and AlN films were obtained with N_2 flow of 50 sccm. However, phases of InN films changed from polycrystalline InN, to In+InN as H_2 flow in the plasma was increased. Best crystalline InN films were obtained when pure nitrogen was used as the plasma gas. Behavior of InN films is different from GaN and AlN films. The use of N_2 plasma yielded high concentration of O impurities in AlN and GaN films, whereas InN film deposited using N_2 plasma includes low concentration

of O impurities. Our results suggest that incorporation of O can easily occur in AlN and GaN at low temperature growth.

2) In the case of InN films, the refractive index increases with decreasing hydrogen concentration in the plasma gas mixture, while in GaN and AlN films the refractive index increases with increasing H_2 flow. Thicknesses of GaN and AlN films increased when N_2 plasma was used. On the other hand, thicknesses of InN films decreased but overall the thickness of InN structure increased including InN+In+voids matrix when N_2/H_2 plasma was used. The analysis shows the coexistence of two types of materials when InN films were deposited using N_2/H_2 plasma: InN and Indium. Amounts of active N species were not sufficient for the growth of InN using N_2/H_2aplasma. Decreases in refractive indices and reduction in thicknesses could be explained with the higher C and O content and less densification in the films.

3) Small sub band gap absorption, present in GaN and AlN films is effectively minimized due to increasing H_2 flow in plasma. The optical band gap of InN films decreases with increasing H_2 flow which might be due to the metallic indium and impurities in InN films.

4) Frequency shifts of GaN, AlN and InN phonon modes with respect to strain-free positions are analyzed in order to assess the strain in these films. AlN films exhibit biaxial stress and it increases as H_2 concentration increases. Phonon frequencies change with changing H_2 flow in the GaN films as a result of in-plane strain in the film. In contrast to GaN and AlN, there is no direct correlation between frequency shifts of E1(TO) modes of InN films and H_2 flow.

In conclusion, we showed that the AlN and GaN films deposited in presence of H_2 plasma contained few contamination of oxygen, where as AlN and GaN films deposited usingaN_2 plasma contained high concentration of O and C impurities. Therefore, for realization of GaN and AlN films by using plasma enhanced ALD method, N_2/H_2 plasma gas should be preferable and it should be at the optimal condition. On the other hand, InN films deposited in the presence of H_2 in the plasma exhibited reduced crystalline quality and high concentrations of O and C impurities were incorporated in the deposited film. These results are key issues to understand and establish depositions of indium rich group III-

nitride alloys at low temperatures using PEALD since the H_2 concentration in the plasma gas is restricting the properties of InN films.

REFERENCES

[1] Keller, S., Li, H., Laurent, M., Hu, Y., Pfaff, N., Lu, J., Brown, D.F., Fichtenbaum, N.A., Speck, J.S., et al. (2014) , Recent progress in metal-organic chemical vapor deposition of (0001¯) N-polar group-III nitrides. Semicond. Sci. Technol. 29(11)

[2] Nakamura, S., Krames, M.R. (2013) , History of gallium-nitride-based light-emitting diodes for illumination. Proc. IEEE 101(10), 2211–2220

[3] Wu, J. (2009) , When group-III nitrides go infrared: New properties and perspectives. J. Appl. Phys. 106(1)

[4] Dietz, N., Alevli, M., Atalay, R., Durkaya, G., Collazo, R., Tweedie, J., Mita, S., Sitar, Z. (2008) , The influence of substrate polarity on the structural quality of InN layers grown by high-pressure chemical vapor deposition. Appl. Phys. Lett. 92(4), 2006–2009

[5] Shen, K.-C., Jiang, M.-C., Liu, H.-R., Hsueh, H.-H., Kao, Y.-C., Horng, R.-H., Wuu, D.-S. (2013) , Pulsed laser deposition of hexagonal GaN-on-Si(100) template for MOCVD applications. Opt. Express 21(22), 26468–74

[6] Junaid, M., Hsiao, C.L., Palisaitis, J., Jensen, J., Persson, P.O.., Hultman, L., Birch, J. (2011) , Electronic-grade GaN(0001)/Al2O3(0001) grown by reactive DC-magnetron sputter epitaxy using a liquid Ga target. Appl. Phys. Lett. 98(14), 2–5

[7] Ozgit, C., Donmez, I., Alevli, M., Biyikli, N. (2012) , Atomic layer deposition of GaN at low temperatures. J. Vac. Sci. Technol. A Vacuum, Surfaces, Film. 30(1), 01A124

[8] Xu, X.H., Wu, H.S., Zhang, C.J., Jin, Z.H. (2001) , Morphological properties of AlN piezoelectric thin films deposited by DC reactive magnetron sputtering. Thin Solid Films 388(1–2), 62–67

[9] Yang, H.F., Shen, W.Z., Qian, Z.G., Pang, Q.J., Ogawa, H., Guo, Q.X. (2002) , Optical constants of InN thin films on (111) GaAs grown by reactive magnetron sputtering. J. Appl. Phys. 91(12), 9803–9808

[10] Alevli, M., Haider, A., Kizir, S., Leghari, S.A., Biyikli, N. (2016) , Comparison of trimethylgallium and triethylgallium as “Ga” source materials for the growth of ultrathin GaN films on Si (100) substrates via hollow-cathode plasma-assisted atomic layer deposition. J. Vac. Sci. Technol. A Vacuum, Surfaces, Film. 34(1), 01A137

[11] Ye, P.D., Wilk, G.D., Yang, B., Kwo, J., Gossmann, H.J.L., Hong, M., Ng, K.K., Bude, J. (2004) , Depletion-mode InGaAs metal-oxide-semiconductor field-effect transistor with oxide gate dielectric grown by atomic-layer deposition. Appl. Phys. Lett. 84(3), 434–436

[12] Lee, S.W., Kwon, O.S., Han, J.H., Hwang, C.S. (2008) , Enhanced electrical properties of SrTiO3 thin films grown by atomic layer deposition at high temperature for dynamic random access

memory applications. Appl. Phys. Lett. 92(22)

[13] Tripp, M.K., Stampfer, C., Miller, D.C., Helbling, T., Herrmann, C.F., Hierold, C., Gall, K., George, S.M., Bright, V.M. (2006) , The mechanical properties of atomic layer deposited alumina for use in micro- and nano-electromechanical systems. Sensors Actuators, A Phys. 130–131(SPEC. ISS.), 419–429

[14] Miikkulainen, V., Leskelä, M., Ritala, M., Puurunen, R.L. (2013) , Crystallinity of inorganic films grown by atomic layer deposition: Overview and general trends. J. Appl. Phys. 113(2)

[15] Suntola n.d., T. Suntola and J. Antson, U.S. patent 4,058, 430 (15 November 1977)

[16] Leskelä, M., Ritala, M. (2002) , Atomic layer deposition (ALD): From precursors to thin film structures. Thin Solid Films 409(1), 138–146

[17] Suntola, T. Atomic Layer Epitaxy, North-Holland Amsterdam, 1989

[18] Parsons, G.N., Elam, J.W., George, S.M., Haukka, S., Jeon, H., (Erwin) Kessels, W.M.M., Leskelä, M., Poodt, P., Ritala, M., et al. (2013) , History of atomic layer deposition and its relationship with the American Vacuum Society. J. Vac. Sci. Technol. A Vacuum, Surfaces, Film. 31(5), 050818

[19] Alevli, M., Ozgit, C., Donmez, I. (2011) , The Influence of Growth Temperature on the Properties of AlN Films Grown by Atomic Layer Deposition. Przyrbwn.Icm.Edu.Pl 120(6), 58–60

[20] Alevli, M., Ozgit, C., Donmez, I., Biyikli, N. (2011) , The influence of N2/H2 and ammonia N source materials on optical and structural properties of AlN films grown by plasma enhanced atomic layer deposition. J. Cryst. Growth 335(1), 51–57

[21] Alevli, M., Ozgit, C., Donmez, I., Biyikli, N. (2012) , Optical properties of AlN thin films grown by plasma enhanced atomic layer deposition. J. Vac. Sci. Technol. A Vacuum, Surfaces, Film. 30(2), 021506

[22] Alevli, M., Ozgit, C., Donmez, I., Biyikli, N. (2012) , Structural properties of AlN films deposited by plasma-enhanced atomic layer deposition at different growth temperatures. Phys. Status Solidi 209(2), 266–271

[23] Bosund, M., Sajavaara, T., Laitinen, M., Huhtio, T., Putkonen, M., Airaksinen, V.M., Lipsanen, H. (2011) , Properties of AlN grown by plasma enhanced atomic layer deposition. Appl. Surf. Sci. 257(17), 7827–7830

[24] Kim, K., Kwak, N., Lee, S. (2009) , Fabrication and properties of AlN film on GaN substrate by using remote plasma atomic layer deposition method. Electron. Mater. Lett. 5(2), 83–86

[25] Ozgit, C., Donmez, I., Alevli, M., Biyikli, N. (2012) , Self-limiting low-temperature growth of crystalline AlN thin films by plasma-enhanced atomic layer deposition. Thin Solid Films 520(7), 2750–2755

[26] McIntosh, F.., Piner, E.., Roberts, J.., Behbehani, M.., Aumer, M.., El-Masry, N.., Bedair, S..

(1997) , Epitaxial deposition of GaInN and InN using the rotating susceptor ALE system. Appl. Surf. Sci. 112, 98–101

[27] Ye, P., Yang, B., Ng, K., Bude, J. (2004) , GaN MOS-HEMT using atomic layer deposition Al2O3 as gate dielectric and surface passivation. Int. J. High Speed Electron. Syst. 14(3), 791–796

[28] Groner, M.D., Fabreguette, F.H., Elam, J.W., George, S.M. (2004) , Low-Temperature Al2O3 Atomic Layer Deposition. Chem. Mater. 4(16), 639–645

[29] Fenwick, W.E., Li, N., Xu, T., Melton, A., Wang, S., Yu, H., Summers, C., Jamil, M., Ferguson, I.T. (2009) , MOCVD growth of GaN on Si(111) substrates using an ALD-grown Al2O3 interlayer. J. Cryst. Growth 311(18), 4306–4310

[30] Lee, J., Ju, H., Lee, J.K., Kim, H.S., Lee, J. (2010) , Atomic layer deposition of TiO2 nanotubes and its improved electrostatic capacitance. Electrochem. Commun. 12(2), 210–212

[31] Kim, S., Kim, D.H., Hong, S.H. (2012) , Epitaxial growth of orthorhombic SnO 2 films on various YSZ substrates by plasma enhanced atomic layer deposition. J. Cryst. Growth 348(1), 15–19

[32] Baji, Z., Lábadi, Z., Horváth, Z.E., Bársony, I. Structure and morphology of aluminium doped Zinc-oxide layers prepared by atomic layer deposition, in: Thin Solid Films, Elsevier B.V., 2012: pp. 4703–4706

[33] Wachnicki, L., Krajewski, T., Łuka, G., Witkowski, B., Kowalski, B., Kopalko, K., Domagala, J.Z., Guziewicz, M., Godlewski, M., et al. Monocrystalline zinc oxide films grown by atomic layer deposition, in: Thin Solid Films, Elsevier B.V., 2010: pp. 4556–4559

[34] Lin, Y.T., Chung, P.H., Lai, H.W., Su, H.L., Lyu, D.Y., Yen, K.Y., Lin, T.Y., Kung, C.Y., Gong, J.R. (2009) , Self-limiting growth of ZnO films on (0 0 0 1) sapphire substrates by atomic layer deposition at low temperatures using diethyl-zinc and nitrous oxide. Appl. Surf. Sci. 256(3), 819–822

[35] Ku, C.S., Lee, H.Y., Huang, J.M., Lin, C.M. (2010) , Epitaxial growth of ZnO films at extremely low temperature by atomic layer deposition with interrupted flow. Mater. Chem. Phys. 120(2–3), 236–239

[36] Krajewski, T., Guziewicz, E., Godlewski, M., Wachnicki, L., Kowalik, I.A., Wojcik-Glodowska, A., Lukasiewicz, M., Kopalko, K., Osinniy, V., et al. (2009) , The influence of growth temperature and precursors' doses on electrical parameters of ZnO thin films grown by atomic layer deposition technique. Microelectronics J. 40(2), 293–295

[37] Chang, Y.C., Huang, M.L., Chang, Y.H., Lee, Y.J., Chiu, H.C., Kwo, J., Hong, M. (2011) , Atomic-layer-deposited Al2O3 and HfO2 on GaN: A comparative study on interfaces and electrical characteristics. Microelectron. Eng. 88(7), 1207–1210

[38] Heo, S.C., Choi, C. (2012) , Plasma atomic layer deposited TiN metal gate for three dimensional device applications: Deposition temperature, capping metal and post annealing. Microelectron.

Eng. 94, 11–13

[39] Fang, Z., Aspinall, H.C., Odedra, R., Potter, R.J. (2011) , Atomic layer deposition of TaN and Ta3N5 using pentakis(dimethylamino)tantalum and either ammonia or monomethylhydrazine. J. Cryst. Growth 331(1), 33–39

[40] Alén, P., Ritala, M., Arstila, K., Keinonen, J., Leskelä, M. (2005) , The growth and diffusion barrier properties of atomic layer deposited NbNx thin films. Thin Solid Films 491(1–2), 235–241

[41] McDaniel, M.D., Ngo, T.Q., Hu, S., Posadas, A., Demkov, A.A., Ekerdt, J.G. (2015) , Atomic layer deposition of perovskite oxides and their epitaxial integration with Si, Ge, and other semiconductors. Appl. Phys. Rev. 2(4)

[42] Hong, T.E., Mun, K.-Y., Choi, S.-K., Park, J.-Y., Kim, S.-H., Cheon, T., Kim, W.K., Lim, B.-Y., Kim, S. (2012) , Atomic layer deposition of Ru thin film using N2/H2 plasma as a reactant. Thin Solid Films 520(19), 6100–6105

[43] Kim, M.R., Lee, J.H., Choi, B.H. Effect of hydrogen plasma on growth of Ir thin film by plasma-enhanced hybrid atomic layer deposition, in: Microelectron. Eng., Elsevier B.V., 2012: pp. 400–404

[44] Kuech, T., ed. Handbook of Crystal Growth: Thin Films and Epitaxy, Elsevier, 2014

[45] Özgit-Akgün, Ç. 2014, Plasma-Assisted Atomic Layer Deposition of Iii-Nitride Thin Films, Bilkent University

[46] Sippola, P. 2018, Study of Thermal and Plasma Enhanced Atomic Layer Deposition of AlN and Al2O3/TiO2 Films for Diverse Applications, Aalto University

[47] Kim, H. (2003) , Atomic layer deposition of metal and nitride thin films: Current research efforts and applications for semiconductor device processing. J. Vac. Sci. Technol. B Microelectron. Nanom. Struct. 21(6), 2231–2261

[48] Puurunen, R.L. (2005) , Surface chemistry of atomic layer deposition: A case study for the trimethylaluminum/water process. J. Appl. Phys. 97(12), 121301

[49] Profijt, H.B., Potts, S.E., van de Sanden, M.C.M., Kessels, W.M.M. (2011) , Plasma-Assisted Atomic Layer Deposition: Basics, Opportunities, and Challenges. J. Vac. Sci. Technol. A Vacuum, Surfaces, Film. 29(5), 050801

[50] Heil, S.B.S., van Hemmen, J.L., Hodson, C.J., Singh, N., Klootwijk, J.H., Roozeboom, F., van de Sanden, M.C.M., Kessels, W.M.M. (2007) , Deposition of TiN and HfO2 in a commercial 200 mm remote plasma atomic layer deposition reactor. J. Vac. Sci. Technol. A Vacuum, Surfaces, Film. 25(5), 1357

[51] Oviroh, P.O., Akbarzadeh, R., Pan, D., Coetzee, R.A.M., Jen, T.-C. (2019) , New development of atomic layer deposition: processes, methods and applications. Sci. Technol. Adv. Mater. 20(1),

465–496

[52] Shan, F.K., Liu, G.X., Lee, W.J., Lee, G.H., Kim, I.S., Shin, B.C. (2006) , Ga2O3 thin film deposited by atomic layer deposition with high plasma power. Integr. Ferroelectr. 80(1), 197–206

[53] Lee, E.J., Ko, M.G., Kim, B.Y., Park, S.K., Kim, H. Do, Park, J.W. (2006) , Lanthanum-oxide thin films deposited by plasma-enhanced atomic layer deposition. J. Korean Phys. Soc. 49(3), 1243–1246

[54] Rossnagel, S.M., Sherman, A., Turner, F. (2000) , Plasma-enhanced atomic layer deposition of Ta and Ti for interconnect diffusion barriers. J. Vac. Sci. Technol. B Microelectron. Nanom. Struct. 18(4), 2016–2020

[55] Alevli, M., Gungor, N. (2017) , Influence of N 2 /H 2 and N 2 plasma on binary III-nitride films prepared by hollow-cathode plasma-assisted atomic layer deposition. J. Vac. Sci. Technol. A Vacuum, Surfaces, Film. 36(1), 01A110

[56] Gungor, N., Alevli, M. (2019) , Visible/infrared refractive index and phonon properties of GaN films grown on sapphire by hollow-cathode plasma-assisted atomic layer deposition. J. Vac. Sci. Technol. A 37(5), 050901

[57] Gungor, N., Alevli, M. (2018) , Role of film thickness on the structural and optical properties of GaN on Si (100) grown by hollow-cathode plasma-assisted atomic layer deposition. J. Vac. Sci. Technol. A Vacuum, Surfaces, Film. 36(2), 021514

[58] Kizir, S., Haider, A., Biyikli, N. (2016) , Substrate impact on the low-temperature growth of GaN thin films by plasma-assisted atomic layer deposition. J. Vac. Sci. Technol. A Vacuum, Surfaces, Film. 34(4), 041511

[59] Ritala, M., Leskelä, M. Handbook of Thin Films, London, Academic Press, 2002

[60] Lim, S.J., Kwon, S.J., Kim, H., Park, J.S. (2007) , High performance thin film transistor with low temperature atomic layer deposition nitrogen-doped ZnO. Appl. Phys. Lett. 91(18), 2012–2015

[61] Banerjee, P., Lee, W.J., Bae, K.R., Lee, S.B., Rubloff, G.W. Structural, electrical, and optical properties of atomic layer deposition Al-doped ZnO films, in: J. Appl. Phys., 2010

[62] Elam, J.W., George, S.M. (2003) , Growth of Zno/Al2O3 alloy films using atomic layer deposition techniques. Chem. Mater. 15(4), 1020–1028

[63] Bakke, J.R., Bent, S.F. Formation of CdxZn1-xS films for photovoltaic buffer layers by atomic layer deposition, in: ECS Trans., 2009: pp. 9–14

[64] Lee, W., Dasgupta, N.P., Jung, H.J., Lee, J.R., Sinclair, R., Prinz, F.B. (2010) , Scanning tunneling spectroscopy of lead sulfide quantum wells fabricated by atomic layer deposition. Nanotechnology 21(48)

[65] Riedel, S., Neidhardt, J., Jansen, S., Wilde, L., Sundqvist, J., Erben, E., Teichert, S., Michaelis, A.

(2011) , Synthesis of SrTiO3 by crystallization of SrO/TiO2 superlattices prepared by atomic layer deposition. J. Appl. Phys. 109(9)

[66] Groner, M.D., George, S.M., McLean, R.S., Carcia, P.F. (2006) , Gas diffusion barriers on polymers using Al 2 O 3 atomic layer deposition. Appl. Phys. Lett. 88(5), 51903–51907

[67] Kayaci, F., Ozgit-Akgun, C., Donmez, I., Biyikli, N., Uyar, T. (2012) , Polymer-inorganic core-shell nanofibers by electrospinning and atomic layer deposition: Flexible nylon-ZnO core-shell nanofiber mats and their photocatalytic activity. ACS Appl. Mater. Interfaces 4(11), 6185–6194

[68] Ceylan, H., Ozgit-Akgun, C., Erkal, T.S., Donmez, I., Garifullin, R., Tekinay, A.B., Usta, H., Biyikli, N., Guler, M.O. (2013) , Size-controlled conformal nanofabrication of biotemplated three-dimensional TiO2 and ZnO nanonetworks. Sci. Rep. 3, 17–19

[69] Bass, M., Stryland, E. Van, Williams, D., Wolfe, W. Handbook of Optics - Volume IV, McGraw-Hill, Inc., 1996

[70] Yang, C.S.-C., Ben-David, A., Samuels, A.C. Infrared ellipsometric measurement of biological films at air/ZnS interfaces, in: Linear Nonlinear Opt. Org. Mater. VI, 2006: p. 63310R

[71] Brodie, G., Jacob, M. V., Farrell, P. (2015) , Techniques for Measuring Dielectric Properties. Microw. Radio-Frequency Technol. Agric.

[72] Sellmeier, W. (1871) , Zur Erkarung der abnormen Farbenfolge im Spectrum einiger. Substanzen. Ann. Der Phys. Und Chemie 219(Series 2, 143), 272–282

[73] Sellmeier, W. (1872) , II. Ueber die durch Aetherschwingungen erregten Mitschwingungen der Körpertheilchen und deren Rückwirkung auf die ersteren, besonders zur Erklärung der Dispersion und ihrer Anomalien. Ann. Phys. 221(4), 520–549

[74] Tompkins, H.G., Irene, E.A. Handbook of Ellipsometry, Springer, 2005

[75] Adachi, S. (1987) , Model dielectric constants of GaP, GaAs, GaSb, InP, InAs, and InSb. Phys. Rev. B 35(14), 7454–7463

[76] Adachi, S. (1988) , Model dielectric constants of Si and Ge. Phys. Rev. B 38(18), 12966–12976

[77] Kawashima, T., Yoshikawa, H., Adachi, S., Fuke, S., Ohtsuka, K. (1997) , Optical properties of hexagonal GaN. J. Appl. Phys. 82(7), 3528

[78] Rakić, A.D., Majewski, M.L. (1996) , Modeling the optical dielectric function of GaAs and AlAs: Extension of Adachi’s model. J. Appl. Phys. 80(10), 5909–5914

[79] Brendel, R., Bormann, D. (1992) , An infrared dielectric function model for amorphous solids. J. Appl. Phys. 71(1), 1–6

[80] Franke, A., Stendal, A., Stenzel, O., Von Borczyskowski, C. (1996) , Gaussian quadrature approach to the calculation of the optical constants in the vicinity of inhomogeneously broadened absorption lines. Pure Appl. Opt. (Print Ed. (United Kingdom) 5(6), 845–853

[81] Kim, C.C., Sivananthan, S. (1995) , Modeling the optical dielectric function of II-VI compound CdTe. J. Appl. Phys. 78(6), 4003–4010

[82] Kim, C.C., Garland, J.W., Abad, H., Raccah, P.M. (1992) , Modeling the optical dielectric function of semiconductors: Extension of the critical-point parabolic-band approximation. Phys. Rev. B 45(20), 11749–11767

[83] Djurišić, A.B., Li, E.H. (1999) , Modeling the optical constants of hexagonal GaN, InN, and AlN. J. Appl. Phys. 85(5), 2848

[84] Craig M. Herzinger, B.D.J. 1995, Dielectric function parametric model, and method of use

[85] Woollam J. A. Co. (2012) , Guide to using WVASE Spectroscopic Ellipsometry Data Acquisition and Analysis Software. J. A. Woollam Co., Inc.

[86] Herzinger, C.M., Johs, B., McGahan, W.A., Woollam, J.A., Paulson, W. (1998) , Ellipsometric determination of optical constants for silicon and thermally grown silicon dioxide via a multi-sample, multi-wavelength, multi-angle investigation. J. Appl. Phys. 83(6), 3323–3336

[87] Ihn, Y.S., Kim, T.J., Ghong, T.H., Kim, Y.D., Aspnes, D.E., Kossut, J. (2004) , Parametric modeling of the dielectric functions of Cd1-xMg xTe alloy films. Thin Solid Films 455–456, 222–227

[88] Zhao, S., Connie, a T., Dastjerdi, M.H.T., Kong, X.H., Wang, Q., Djavid, M., Sadaf, S., Liu, X.D., Shih, I., et al. (2015) , Aluminum nitride nanowire light emitting diodes: Breaking the fundamental bottleneck of deep ultraviolet light sources. Sci. Rep. 5, 8332

[89] Schubert, M. Infrared ellipsometry on semiconductor layer structures: phonons, plasmons, and polaritons., 2004

[90] Harima, H. (2002) , Properties of GaN and related compounds studied by means of Raman scattering. J. Phys. Condens. Matter 14(38), R967–R993

[91] Barker Jr, A.S., Ilegems, M. (1973) , Infrared lattice vibrations and free-electron dispersion in GaN. Phys. Rev. B 7(2), 743–750

[92] Gervais, F., Piriou, B. (1974) , Anharmonicity in several-polar-mode crystals: Adjusting phonon self-energy of LO and to modes in Al2O3 and TiO2 to fit infrared reflectivity. J. Phys. C Solid State Phys. 7(13), 2374–2386

[93] Berreman, D.W., Unterwald, F.C. (1968) , Adjusting Poles and Zeros of Dielectric Dispersion to Fit Reststrahlen of Pr Cl 3 and La Cl 3. Phys. Rev. 174(3), 791

[94] Schubert, M., Tiwald, T., Herzinger, C. (2000) , Infrared dielectric anisotropy and phonon modes of sapphire. Phys. Rev. B 61(12), 8187–8201

[95] Lowndes, R.P. (1970) , Influence of Lattice Anharmonic on the longitudinal optic modes of Cubic ionic solids. Phys. Rev. B 1(6), 2754

[96] Paul, W., Keller, S.P. Handbook on Semiconductors, Amsterdam, North-Holland, 1980

[97] Kittel, C. Introduction to Solid State Physics, New York, Wiley, 1976

[98] Kukharskii, A.A. (1973) , Plasmon-phonon coupling in GaAs. Solid State Commun. 13(11), 1761–1765

[99] Kasic, A., Schubert, M., Einfeldt, S., Hommel, D., Tiwald, T.E. (2000) , Free-carrier and phonon properties of n- and p-type hexagonal GaN films measured by infrared ellipsometry. Phys. Rev. B 62(11), 7365–7377

[100] Kankanamge, I.M. 2016, Optoelectronic and Structural Properties of Group III-Nitride Semiconductors Grown by High Pressure MOCVD and Migration Enhanced Plasma Assisted MOCVD, Georgia State University

[101] Alevli, M. 2008, Growth and Characterezation of Indium Nitride Layers Grown by High-Pressure Chemical Vapor Deposition, Georgia State University

[102] Feng, Z., Wang, W., Chua, S., Zhang, P., Williams, K., Pitt, G. (2001) , Raman scattering properties of GaN thin films grown on sapphire under visible and ultraviolet excitation. J. Raman Spectrosc. 32, 840–846

[103] Kuball, M. (2001) , Raman spectroscopy of GaN, AlGaN and AlN for process and growth monitoring/control. Surf. Interface Anal. 31(10), 987–999

[104] Dietz, N. (n.d.) , Reflection and Refraction in Multi-layered Heterostructures : Interference Reflection and Refraction in Multi-layered Heterostructures : Interference. , 49–53

[105] Bennett, J.M. Polarization, in: Handb. Opt., McGraw-Hill, Inc., 2009

[106] Zhang, T., Yin, J., Ding, L.H., Zhang, W.F. (2013) , Optical study of Ba(MnxTi(1-x)O3) thin films by spectroscopic ellipsometry. Chinese Phys. B 22(11)

[107] Fujiwara, H. Spectroscopic Ellipsometry Principles and Applications, 2007

[108] Butt, H.-J., Graf, K., Kappl, M. Measurement of Adsorption Isotherms, in: Phys. Chem. Interfaces, Weinheim, Wiley-VCH, 2006: p. 2006

[109] J.A. Woollam Co., I. (n.d.) , Mark II Features. J. A. Woollam Co., Inc.

[110] Boer, D., Gerardus, J.H.W. 1995, Spectroscopic infrared ellipsometry : components, calibration, and application, Eindhoven: Technische Universiteit Eindhoven

[111] Tiwald, T. (2008) , Determining the effects of backsurface reflections for IR-VASE data. J. A. Woollam Co., Inc. (402), 1–8

[112] Tompkins, H.G., Tiwald, T. (2009) , Training Manual for IR-VASE. J. A. Woollam Co., Inc.

[113] Bragg, W.H., Bragg, W.L. (1913) , The reflection of X-rays by crystals. Proc. R. Soc. London. Ser. A, Contain. Pap. a Math. Phys. Character 88(605), 428–438

[114] Hüfner, S. Photoelectron spectroscopy: principles and applications., Springer Science & Business Media, 2013

[115] Dönmez, İ. 2002, Atomic Layer Deposition of Metal Oxide Thin Films and nanostructures, Bilkent University

[116] Binnig, G., Quate, C.F., Gerber, C. (1986) , Atomic Force Microscope. Phys. Rev. Lett. 56(9), 930

[117] Nakamura, S. (1998) , The Roles of Structural Imperfections in InGaN-Based Blue Light-Emitting Diodes and Laser Diodes. Science (80-.). 281(5379), 956–961

[118] Sugiura, M., Kushimoto, M., Mitsunari, T., Yamashita, K., Honda, Y., Amano, H., Inoue, Y., Mimura, H., Aoki, T., et al. Study of radiation detection properties of GaN pn diode, in: Jpn. J. Appl. Phys., 2016: p. 05FJ02

[119] Johnstone, D., Biyikli, S., Dogan, S., Moon, Y.T., Yun, F., Morkoc, H. Comparison of deep levels in GaN grown by MBE, MOCVD, and HVPE, in: Light. Diodes Res. Manuf. Appl. IX, 2005: p. 7

[120] Detchprohm, T., Hiramatsu, K., Itoh, K., Akasaki, I. (1992) , Relaxation Process of the Thermal Strain in the Gan/Alpha-Al2O3 Heterostructure and Determination of the Intrinsic Lattice-Constants of Gan Free From the Strain. Japanese J. Appl. Phys. Part 2-Letters 31, L1454–L1456

[121] Li, G., Wang, W., Yang, W., Lin, Y., Wang, H., Lin, Z., Zhou, S. (2016) , GaN-based light-emitting diodes on various substrates: A critical review. Reports Prog. Phys. 79(5), 56501

[122] Rabiee Golgir, H., Gao, Y., Zhou, Y.S., Fan, L., Thirugnanam, P., Keramatnejad, K., Jiang, L., Silvain, J.F., Lu, Y.F. (2014) , Low-temperature growth of crystalline gallium nitride films using vibrational excitation of ammonia molecules in laser-assisted metalorganic chemical vapor deposition. Cryst. Growth Des. 14(12), 6248–6253

[123] Ozgit-Akgun, C., Goldenberg, E., Okyay, A.K., Biyikli, N. (2014) , Hollow cathode plasma-assisted atomic layer deposition of crystalline AlN, GaN and AlxGa1−xN thin films at low temperatures. J. Mater. Chem. C 2(12), 2123

[124] Hiramatsu, K., Detchprohm, T., Akasaki, I. (1993) , Relaxation Mechanism of Thermal Stresses in the Heterostructure of GaN Grown on Sapphire by Vapor Phase Epitaxy. Jpn. J. Appl. Phys. 32(Part 1, No. 4), 1528–1533

[125] Aseev, P., Rodriguez, P.E.D.S., Gómez, V.J., Alvi, N.U.H., Mánuel, J.M., Morales, F.M., Jiménez, J.J., García, R., Senichev, A., et al. (2015) , Near-infrared emitting In-rich InGaN layers grown directly on Si: Towards the whole composition range. Appl. Phys. Lett. 106(7), 072102

[126] Motamedi, P., Dalili, N., Cadien, K.C. (2015) , A Route to Low Temperature Growth of Single Crystal GaN on Sapphire. J. Mater. Chem. C 3, 7428–7436

[127] Saron, K.M.A., Hashim, M.R., Farrukh, M.A. (2013) , Growth of GaN films on silicon (1 1 1) by thermal vapor deposition method: Optical functions and MSM UV photodetector applications.

Superlattices Microstruct. 64, 88–97

[128] Zhou, S.Q., Vantomme, A., Zhang, B.S., Yang, H., Wu, M.F. (2005) , Comparison of the properties of GaN grown on complex Si-based structures. Appl. Phys. Lett. 86(8), 1–3

[129] Guzmán, G., Herrera, M., Silva, R., Vásquez, G.C., Maestre, D. (2016) , Influence of oxygen incorporation on the defect structure of GaN microrods and nanowires. An XPS and CL study. Semicond. Sci. Technol. 31(5), 055006

[130] Li, D., Sumiya, M., Fuke, S., Yang, D., Que, D., Suzuki, Y., Fukuda, Y. (2001) , Selective etching of GaN polar surface in potassium hydroxide solution studied by x-ray photoelectron spectroscopy. J. Appl. Phys. 90(8), 4219–4223

[131] Shang, L., Lu, T., Zhai, G., Jia, Z., Zhang, H., Ma, S., Li, T., Liang, J., Liu, X., et al. (2015) , The evolution of a GaN/sapphire interface with different nucleation layer thickness during two-step growth and its influence on the bulk GaN crystal quality. RSC Adv. 5(63), 51201–51207

[132] Djurišić, A.B., Li, E.H. (2001) , Dielectric function models for describing the optical properties of hexagonal GaN. J. Appl. Phys. 89(1), 273–282

[133] Ahn, H., Shen, C.H., Wu, C.L., Gwo, S. (2005) , Spectroscopic ellipsometry study of wurtzite InN epitaxial films on Si(111) with varied carrier concentrations. Appl. Phys. Lett. 86(20), 1–3

[134] Djurišić, A.B., Tsang, K.-O., Li, E.H. (1999) , Modeling the optical constants of wide bandgap materials. Proc. SPIE - Int. Soc. Opt. Eng. 3625, 49–56

[135] Pal, D., Mathur, A., Singh, A., Singhal, J., Sengupta, A., Dutta, S., Zollner, S., Chattopadhyay, S. (2017) , Tunable optical properties in atomic layer deposition grown ZnO thin films. J. Vac. Sci. Technol. A Vacuum, Surfaces, Film. 35(1), 01B108

[136] Motamedi, P., Cadien, K. (2015) , Structural and optical characterization of low-temperature ALD crystalline AlN. J. Cryst. Growth 421, 45–52

[137] Van Bui, H., Wiggers, F.B., Gupta, A., Nguyen, M.D., Aarnink, A.A.I., de Jong, M.P., Kovalgin, A.Y. (2015) , Initial growth, refractive index, and crystallinity of thermal and plasma-enhanced atomic layer deposition AlN films. J. Vac. Sci. Technol. A Vacuum, Surfaces, Film. 33(1), 01A111

[138] Kumar, S., Kumar, S., Sharma, P., Sharma, V., Katyal, S.C. (2012) , CdS nanofilms: Effect of film thickness on morphology and optical band gap. J. Appl. Phys. 112(12)

[139] Alevli, M., Gungor, N., Haider, A., Kizir, S., Leghari, S.A., Biyikli, N. (2016) , Substrate temperature influence on the properties of GaN thin films grown by hollow-cathode plasma-assisted atomic layer deposition. J. Vac. Sci. Technol. A Vacuum, Surfaces, Film. 34(1), 01A125

[140] Mridha, S., Basak, D. (2007) , Effect of thickness on the structural, electrical and optical properties of ZnO films. Mater. Res. Bull. 42(5), 875–882

[141] Biswas, A., Bhattacharyya, D., Sahoo, N.K., Yadav, B.S., Major, S.S., Srinivasa, R.S. (2008) ,

Spectroscopic ellipsometry studies of GaN films deposited by reactive rf sputtering of GaAs target. J. Appl. Phys. 103(8)

[142] Preschilla A., N., Major, S., Kumar, N., Samajdar, I., Srinivasa, R.S. (2000) , Nanocrystalline gallium nitride thin films. Appl. Phys. Lett. 77(12), 1861

[143] Maity, A.B., Chaudhuri, S., Pal, A.K. (1994) , Modification of the absorption edge due to grain boundaries and mechanical stresses in polycrystalline semiconductor films. Phys. Status Solidi 183(1), 185–191

[144] Nakamura, S. (2015) , Background Story of the Invention of Efficient Blue InGaN Light Emitting Diodes. Int. J. Mod. Phys. B 29(32), 1530016

[145] Alevli, M., Atalay, R., Durkaya, G., Weesekara, A., Perera, A.G.U., Dietz, N., Kirste, R., Hoffmann, A. (2008) , Optical characterization of InN layers grown by high-pressure chemical vapor deposition. J. Vac. Sci. Technol. A Vacuum, Surfaces, Film. 26(4), 1023–1026

[146] Nepal, N., Anderson, V.R., Hite, J.K., Eddy, C.R. (2015) , Growth and Characterization of III-N Ternary Thin Films by Plasma Assisted Atomic Layer Epitaxy at Low Temperatures. Thin Solid Films 589, 47–51

[147] Cavanagh, A.S., Roshko, A., Wahl, K.J., Sprenger, J.K., George, S.M., Sun, H. (2016) , Electron Enhanced Growth of Crystalline Gallium Nitride Thin Films at Room Temperature and 100 °C Using Sequential Surface Reactions. Chem. Mater. 28(15), 5282–5294

[148] Motamedi, P., Cadien, K. (2015) , Structure-property relationship and interfacial phenomena in GaN grown on C-plane sapphire via plasma-enhanced atomic layer deposition. RSC Adv. 5(71), 57865–57874

[149] Liu, L., Edgar, J.H. (2002) , Substrates for gallium nitride epitaxy. Mater. Sci. Eng. R Reports 37, 61–127

[150] Jeffries, A.M., Ding, L., Williams, J.J., Williamson, T.L., Hoffbauer, M.A., Honsberg, C.B., Bertoni, M.I. (2017) , Gallium nitride grown by molecular beam epitaxy at low temperatures. Thin Solid Films 642, 25–30

[151] Hushur, A., Manghnani, M.H., Narayan, J. (2009) , Raman studies of GaN/sapphire thin film heterostructures. J. Appl. Phys. 106(5)

[152] Ahmad, I., Holtz, M., Faleev, N.N., Temkin, H. (2004) , Dependence of the stress-temperature coefficient on dislocation density in epitaxial GaN grown on α-Al2O3and 6H-SiC substrates. J. Appl. Phys. 95(4), 1692–1697

[153] Wang, H., Lin, Z., Lin, Y., Wang, W., Li, G. (2017) , High-Performance GaN-Based LEDs on Si Substrates: The Utility of Ex Situ Low-Temperature AlN Template with Optimal Thickness. IEEE Trans. Electron Devices 64(11), 4540–4546

[154] Cowern, N.E.B., Bennett, N.S., Gwilliam, R.M., Bailey, P., Lankinen, A., Horan, K., O'Reilly, L., Sealy, B.J., Noakes, T.C.Q., et al. (2008) , Constraints on micro-Raman strain metrology for highly doped strained Si materials. Appl. Phys. Lett. 92(23), 233506

[155] Darakchieva, V., Valcheva, E., Paskov, P.P., Schubert, M., Paskova, T., Monemar, B., Amano, H., Akasaki, I. (2005) , Phonon mode behavior in strained wurtzite AlN/GaN superlattices. Phys. Rev. B - Condens. Matter Mater. Phys. 71(11), 1–9

[156] Hu, Z.G., Strassburg, M., Weerasekara, A., Dietz, N., Perera, A.G.U., Kane, M.H., Asghar, A., Ferguson, I.T. (2006) , Lattice vibrations in hexagonal Ga 1-xMn xN epitaxial films on c-plane sapphire substrates by infrared reflectance spectra. Appl. Phys. Lett. 88(6), 6–8

[157] Eddy, C.R., Nepal, N., Hite, J.K., Mastro, M. a. (2013) , Perspectives on future directions in III-N semiconductor research. J. Vac. Sci. Technol. A Vacuum, Surfaces, Film. 31(5), 058501

[158] Haider, A., Kizir, S., Biyikli, N. (2016) , Low-temperature self-limiting atomic layer deposition of wurtzite InN on Si(100). AIP Adv. 6(4)

[159] Ozgit-Akgun, C., Goldenberg, E., Bolat, S., Tekcan, B., Kayaci, F., Uyar, T., Okyay, A.K., Biyikli, N. (2015) , Low-temperature hollow cathode plasma-assisted atomic layer deposition of crystalline III-nitride thin films and nanostructures. Phys. Status Solidi Curr. Top. Solid State Phys. 12(4–5), 394–398

[160] J. A. Woollam Co. Guide to using WVASE32: Spectroscopic ellipsome- try data acquisition and analysis software, Lincoln, NE, 2008

[161] Herzinger, C.M., Snyder, P.G., Johs, B., Woollam, J.A. (1995) , InP optical constants between 0.75 and 5.0 eV determined by variable-angle spectroscopic ellipsometry. J. Appl. Phys. 77(4), 1715–1724

[162] Nagata, T., Koblmüller, G., Bierwagen, O., Gallinat, C.S., Speck, J.S. (2009) , Surface structure and chemical states of a-plane and c-plane InN films. Appl. Phys. Lett. 95(13), 20–23

[163] Piper, L.F.J., Veal, T.D., Jefferson, P.H., McConville, C.F., Fuchs, F., Furthmüller, J., Bechstedt, F., Lu, H., Schaff, W.J. (2005) , Valence-band structure of InN from x-ray photoemission spectroscopy. Phys. Rev. B - Condens. Matter Mater. Phys. 72(24), 1–5

[164] Wu, J., Walukiewicz, W., Li, S.X., Armitage, R., Ho, J.C., Weber, E.R., Haller, E.E., Lu, H., Schaff, W.J., et al. (2004) , Effects of electron concentration on the optical absorption edge of InN. Appl. Phys. Lett. 84(15), 2805–2807

[165] Davydov, V.Y., Kitaev, Y.E., Goncharuk, I.N., Smirnov, A.N., Graul, J., Semchinova, O., Uffmann, D., Smirnov, M.B., Mirgorodsky, A.P., et al. (1998) , Phonon dispersion and Raman scattering in hexagonal GaN and AlN. Phys. Rev. B 58(19), 12899–12907

[166] Darakchieva, V., Paskov, P.P., Paskova, T., Birch, J., Tungasmita, S., Monemar, B. (2002) , Deformation potentials of the E1(TO) mode in AlN. Appl. Phys. Lett. 80(13), 2302–2304

[167] Darakchieva, V. (2008) , Infrared generalized ellipsometry on non-polar and superlattice group-III nitride films: strain and phonon anisotropy. Phys. Status Solidi a-Applications Mater. Sci. 205(4), 905–913

[168] Darakchieva, V., Paskov, P., Valcheva, E., Paskova, T., Monemar, B., Schubert, M., Lu, H., Schaff, W.J. (2004) , Deformation potentials of the E[sub 1](TO) and E[sub 2] modes of InN. Appl. Phys. Lett. 84(18), 3636–3638

[169] Arora, A.K., Rajalakshmi, M., Ravindran, T.R., Sivasubramanian, V.R. (2007) , Raman spectroscopy of optical phonon confinement in nanostructured materials. J. Raman Spectrosc. 38(April), 604–617

ÖZGEÇMİŞ

ÖDÜLLER

2010- 2012 **TÜBİTAK**- Son Sınıf Lisans Öğrencileri için Yurt İçi Lisansüstü Bursu

2013- 2017 **TÜBİTAK**- Yurtiçi Doktora Bursu

ESERLER

A. Uluslararası hakemli dergilerde yayımlanan makaleler:

A1. *"Visible/Infrared refractive index and phonon properties of GaN films grown on sapphire by hollow-cathode plasma-assisted atomic layer deposition."* Neşe Güngör, Mustafa Alevli. **Journal of Vacuum Science & Technology A: Vacuum, Surfaces, and Films, 37(5) (2019)**

A2. **"***Influence of N_2/H_2 and N_2 plasma on binary III-nitride films prepared by hollow-cathode plasma-assisted atomic layer deposition."* Mustafa Alevli, Neşe Güngör. **Journal of Vacuum Science & Technology A: Vacuum, Surfaces, and Films, 36(1), 01A110 (2018).**

A3. *"The role of film thickness on the structural and optical properties of GaN on Si (100) grown by hollow-cathode plasma-assisted atomic layer deposition."* Neşe Güngör, Mustafa Alevli. **Journal of Vacuum Science & Technology A: Vacuum, Surfaces, and Films, 36(2) (2018)**

A4. *"Substrate temperature influence on the properties of GaN thin films grown by hollow-cathode plasma-assisted atomic layer deposition. "* Mustafa Alevli, Neşe Güngör, Ali Haider, Seda Kizir, Shahid A Leghari, Necmi Biyikli. **Journal of Vacuum Science & Technology A34 /1/01A125 (2016)**

A5. *"Effect of reactor pressure on optical and electrical properties of InN films grown by high-pressure chemical vapor deposition. "* Mustafa Alevli, Neşe Güngör, Sabri Alkis, Cagla Ozgit-Akgun, Inci Donmez, Ali Kemal Okyay, Sampath Gamage, Indika

Senevirathna, Nikolaus Dietz, Necmi Biyikli. **physica status solidi (c) 12/4-5/423-429 (2015)**

B. <u>Uluslararası bilimsel toplantılarda sunulan ve bildiri kitaplarında (p*roceedings*) basılan bildiriler:</u>

B1. *"Optical anisotropy studies of GaN on Si (100) grown by hollow-cathode plasma-assisted atomic layer deposition. "* Neşe Gungor, Mustafa Alevli. 2018 the European Materials Research Society Spring Meeting and Exhibit, 18 -22 June 2018, Strasbourg, FRANCE

B2. *"Critical layer thickness determination of GaN thin films on sapphire grown by hollow-cathode plasma-assisted atomic layer deposition."* Mustafa Alevli, Neşe Güngör. 2018 the European Materials Research Society Spring Meeting and Exhibit, 18 -22 June 2018, Strasbourg, FRANCE

B3. *"Optical properties of GaN and InN on quartz grown by hollow-cathode plasma-assisted atomic layer deposition"* Neşe Gungor, Mustafa Alevli. 2017 ICG Annual Meeting & 32. ŞİŞECAM Glass Symposium, 22-25 Ekim 2017.İstanbul, TÜRKİYE

B4. *"The role of thickness on infrared optical properties of GaN films grown by hollow-cathode plasma-assisted atomic layer deposition"* Neşe Gungor, Mustafa Alevli, Seda Kizir, Ali Haider, Necmi Bıyıklı. Turkish Physical Society, 32nd International Physics Congress, 6-9 September 2016 Bodrum, TURKEY.

B5. *"Influence of N_2/H_2 and N_2 plasma on binary III-Nitride films prepared by hollow-cathode plasma-assisted atomic layer deposition"* Mustafa Alevli, Neşe Gungor, Cagla Ozgit-Akgun, Ali Haider, Seda Kizir, Necmi Bıyıklı. 16th International Conference on Atomic Layer Deposition, 24th-27th July, 2016 Dublin, IRELAND

B6. *"Infrared dielectric functions, phonon modes, and band-gap properties of plasma-assisted ALD-grown $In_xGa_{1-x}N$ films"* Mustafa Alevli, Neşe Gungor, Ali Haider, Seda Kizir, Necmi Bıyıklı. 16th International Conference on Atomic Layer Deposition, 24th-27th July, 2016 Dublin, IRELAND

B7. *"The role of film thickness on the visible/UV and infrared optical properties of GaN films grown by hollow-cathode plasma-assisted atomic layer deposition"* Mustafa Alevli, Neşe Gungor, Ali Haider, Seda Kizir, Necmi Bıyıklı. 16th International Conference on Atomic Layer Deposition, 24th-27th July, 2016 Dublin, IRELAND

B8. *"Effect of substrate temperature and Ga source precursor on growth and material properties of GaN grown by hollow cathode plasma assisted atomic layer deposition."* Ali Haider, Seda Kizir, Piter Deminskyi, Oleksandr Tsymbalenko, Shahid Ali Leghari, Mustafa Alevli, Neşe Güngör, Necmi Bıyıklı. In:2016 IEEE 36th International Conference on Electronics and Nanotechnology, ELNANO 2016-Conference Proceedings. Institute of Electrical and Electronics Engineers Inc., 2016. p. 132-134.

B9. *"Comparison studies of GaN grown with Trimethylgallium and Triethylgallium for optoelectronic applications."* Mustafa Alevli, Ali Haider, Neşe Gungor, Seda Kizir, Sabri Alkis, Ali Kemal Okyay, Necmi Bıyıklı. AVS 62 International Symposium and Exhibition. October 18-23, 2015 San Jose, California.

B10. "*Comparison of Trimethylgallium and Triethylgallium as "Ga" source materials for the growth of ultra-thin GaN films via hollow-cathode plasma-assisted ALD"* Mustafa Alevli, Neşe Gungor, Cagla Ozgit-Akgun, Ali Haider, Seda Kizir, Shahid A Leghari, Sabri Alkis, Ali Kemal Okyay , Necmi Bıyıklı. 15th International Conference on Atomic Layer Deposition, June 28-July 1, 2015 Portland, Oregon USA

B11. "*Substrate temperature influence on the properties of GaN thin films grown by hollow-cathode plasma-assisted atomic layer deposition"* Mustafa Alevli, Neşe Gungor, Cagla Ozgit-Akgun, Seda Kizir, Ali Haider, Shahid A Leghari, Sabri Alkis, Ali Kemal Okyay, Necmi Bıyıklı. 15th International Conference on Atomic Layer Deposition, June 28-July 1, 2015 Portland, Oregon USA

C. <u>Ulusal bilimsel toplantılarda sunulan ve bildiri kitaplarında basılan bildiriler:</u>

C1. *"Substrate Effect on Optical Properties of InN Thin Films Grown by Hollow Cathode Assisted Atomic Layer Deposition "* Neşe Gungor, Mustafa Alevli. Fotonik 2016, 19. Ulusal Optik, Elektro-Optik ve Fotonik Çalıştayı, 22 Eylül 2017, Koç Üniversitesi, TÜRKİYE

C2. "*Critical Thickness on Optical Properties at UV-VIS and Infrared Region of GaN Thin Films Grown by Hollow Cathode Assisted Atomic Layer Deposition. "* Neşe Gungor, Mustafa Alevli. Fotonik 2016, 18. Ulusal Optik, Elektro-Optik ve Fotonik Çalıştayı, 23 Eylül 2016, Bilkent Üniversitesi, TÜRKİYE

C3. *"Effect of growth temperature and film thickness on structural and optical properties of AlN films grown by plasma enhanced atomic layer deposition",* Neşe Güngör, Çağla Özgit Akgün, Necmi Bıyıklı, Mustafa Alevli, NanoTr, 8th Nanoscience and Nanotecnology Conference, 25-29 Haziran 2012, Hacettepe Üniversitesi, Ankara